TECHNISCHE UNIVERSITÄT WIEN
Vienna | Austria

INSTITUT FÜR PHOTONIK
Photonics Institute

DISSERTATION

Applications of Intense Laser Pulses to the Control of Attosecond Processes in Gas-Phase Atoms and Dimers

ausgeführt zum Zwecke der Erlangung des akademischen Grades

Doktor der technischen Wissenschaften

unter der Anleitung von

Privatdoz. Dipl.-Ing. Dr.techn. Markus Kitzler

und

Univ. Prof. Andrius Baltuška, Ph.D.

am Institut für Photonik der Technischen Universität Wien.

Eingereicht an der Technischen Universität Wien

Fakultät für Elektrotechnik und Informationstechnik

von

Dipl. Ing. Martin Dorner-Kirchner

Matrikelnummer: 00925748

Wien, 8. Juli 2022 _____

Acknowledgments

A doctoral thesis is typically attributed to a single person, but in truth it is an achievement only possible with the support of many. Here I would like to express my deep gratitude to the people that accompanied me on this journey. A heartfelt **THANK YOU** to all of you!.

I'd like to start with Markus Kitzler, who sparked my curiosity about physics at almost inconceivable short time scales, invited me to pursue a Ph.D. in this field and his guidance, support and care throughout.

Andrius Baltuška, for giving me the opportunity to work in his Ultrafast Laser Group, and cultivating this positive environment and its infrastructure.

Ondřej Hort and Sonia Erattupuzha, who soon after my arrival at the Photonics Institute already moved on, but were responsible for my initial introduction to the laboratory work with lasers and taught me to keep my eyes safe (successfully so far).

Paolo A. Carpeggiani, for further refinement of essential scientific skills and, more importantly, core concepts of the Italian language and old tricks of John Wayne.

Xiaojun Liu and his group from the Innovation Academy for Precision Measurement Science and Technology (APM) in Wuhan, China, for our fruitful collaboration, and especially Yanlan Wang, for her dedicated work on simulations even during the difficult times of the corona pandemic.

Václav Hanus and Sarayoo Kangaparambil, for sharing their experience, tools, enthusiasm and countless hours of feeding good 'potatoes' to the COLTRIMS setup with me.

Valentina Shumakova and Edgar Kaksis, for their help with the ytterbium laser system, valuable insights and scientific, as well as non-scientific discussion.

To all current and former members of the Photonics Institute, for such a wonderful work environment, where any call for help or advice was quickly

answered and only rarely tools borrowed without returning them. A special thanks goes to Melanie Molnar for being the administrative glue that keeps everything together.

Lucia, für deine Unterstützung, die Möglichkeit mich zu entfalten und meinen Platz zu finden. Danke!

Iris, for your support and fighting through places I don't dare. I love you.

Raphael, for filling everything with light and music. Don't stop Meow!

Abstract

When a laser pulse interacts with a physical system, the laser electric field directly couples to the system's electronic structure and allows to observe and, given sufficient field strength, steer processes therein. In this thesis intense ultrashort laser pulses are applied to the investigation and control of three specific processes in the electronic structure of gas-phase atoms and dimers on their natural attosecond time scale. As properties of matter are ultimately determined by its electronic structure these fundamental processes have implications for many important natural and technical mechanisms.

The first process is the laser induced transfer and transient capture (LITE) of an electron from one atom across its system boundary to the other atom within an argon dimer. By reaction microscopy it is found that this electron transfer process triggers attosecond electron-electron interaction dynamics in the neighboring argon atom and that this is influenced by the carrier envelope phase (CEP) of the inducing laser pulse. Then, these findings are further investigated in the same sample system of argon dimers, where it is observed that also for the process of recapture of an electron into excited high lying Rydberg states, so-called frustrated field ionization (FFI), control can be exerted via CEP of ultrashort laser pulses. These findings disclose a strong-field route to controlling the dynamics in molecular compounds through the excitation of electronic dynamics on a distant molecule by driving inter-molecular electron-transfer processes.

Distinct from these fundamental investigations on electronic processes, furthermore in this thesis a practical approach for driving the process of high harmonic generation (HHG) is presented. It combines the high power scalability of a ytterbium based laser system with efficient spectral broadening and simultaneous red-shift by stimulated Raman scattering (SRS) in a long stretched hollow core fiber (HCF) to significantly extend the achievable cut-off energy beyond previous limitations.

6

Journal publications

Publications that directly contribute to this thesis are highlighted in blue.

[1] V. Hanus, S. Kangaparambil, S. Larimian, **M. Dorner-Kirchner**, X. Xie, M. S. Schöffler, G. G. Paulus, A. Baltuška, A. Staudte, and M. Kitzler-Zeiler, "Subfemtosecond tracing of molecular dynamics during strong-field interaction," Phys. Rev. Lett. **123**, 263201 (2019).

[2] V. Hanus, S. Kangaparambil, S. Larimian, **M. Dorner-Kirchner**, X. Xie, M. S. Schöffler, G. G. Paulus, A. Baltuška, A. Staudte, and M. Kitzler-Zeiler, "Experimental separation of subcycle ionization bursts in strong-field double ionization of H_2," Phys. Rev. Lett. **124**, 103201 (2020).

[3] S. Kangaparambil, V. Hanus, **M. Dorner-Kirchner**, P. He, S. Larimian, G. Paulus, A. Baltuška, X. Xie, K. Yamanouchi, F. He, E. Lötstedt, and M. Kitzler-Zeiler, "Generalized phase sensitivity of directional bond breaking in the laser-molecule interaction," Phys. Rev. Lett. **125**, 023202 (2020).

[4] Y. Wang, X. Lai, S. Yu, R. Sun, X. Liu, **M. Dorner-Kirchner**, S. Erattupuzha, S. Larimian, M. Koch, V. Hanus, S. Kangaparambil, G. Paulus, A. Baltuška, X. Xie, and M. Kitzler-Zeiler, "Laser-induced electron transfer in the dissociative multiple ionization of argon dimers," Phys. Rev. Lett. **125**, 063202 (2020).

[5] V. Hanus, S. Kangaparambil, S. Larimian, **M. Dorner-Kirchner**, X. Xie, A. Baltuška, and M. Kitzler-Zeiler, "Exploring photoelectron angular distributions emitted from molecular dimers by two delayed intense laser pulses," Phys. Rev. A **102**, 053115 (2020).

[6] H. Hu, S. Kangaparambi, **M. Dorner-Kirchner**, V. Hanus, A. Baltuška, M. Kitzler-Zeiler, and X. Xie, "Quantitative retrieval of the angular dependence of laser-induced electron rescattering in molecules," Phys. Rev. A **103**, 013114 (2021).

Journal publications

[7] **M. Dorner-Kirchner**, S. Erattupuzha, S. Larimian, M. Koch, V. Hanus, S. Kangaparambil, G. Paulus, A. Baltuška, X. Xie, M. Kitzler-Zeiler, Y. Wang, X. Lai, S. Yu, R. Sun, and X. Liu, "Laser-subcycle control of electronic excitation across system boundaries," Journal of Physics B: Atomic, Molecular and Optical Physics **54**, 164004 (2021).

[8] **M. Dorner-Kirchner**, V. Shumakova, G. Coccia, E. Kaksis, B. Schmidt, V. Pervak, A. Pugzlys, A. Baltuška, M. Kitzler-Zeiler, and P.-A. Carpeggiani, "HHG at the carbon K-edge directly driven by SRS red-shifted pulses from an ytterbium amplifier," **In Preparation** (2022).

Contents

Contents

"Certainty of death. Small chance of success. What are we waiting for?"
— *Gimli, son of Glóin, The Return of the King*

Chapter 1

Motivation and outline of thesis

Imagine another life scaled by a factor of 10^{-18} to the atto-world. On attometer scale, with a heartbeat as fast as oscillating light fields and a lifetime of about two nanoseconds, all of human history would fit into less than a microsecond. The movement of gas molecules being like planets in a sea of nothingness. Half a second would be equivalent to birth and death of an entire universe in this other life. One could directly observe changes in the electronic structure that are fundamental to the properties of matter and processes therein.

Outside such a life, this achievement is only possible by the utilization of a special tool: intense ultrashort laser pulses [9]. These laser pulses not only allow for the probing, but by their strong electric fields, they can also be applied to control electronic processes on their natural time scales [10]. Such control in the atto-world has practical real life consequences, as dynamic electronic processes are at the basis of charge and energy transfer mechanisms, chemical reactions and light-matter interaction. Nowadays it is possible to produce laser pulses with durations down to single oscillation cycles of the electric field and one can use them as time reference on the femtosecond scale [11]. To act on the attosecond time scale, one can consider

that electrons directly couple to the laser electric field, which can be further shaped on sub-laser-cycle times by various techniques, such as control of the polarization [12], stabilization of the carrier-envelope phase (CEP) [13] or multi-color waveform synthesis [14]. Another route to reach the atto-world is via the application of sub-fs laser pulses in the extreme ultra-violet (XUV) or soft X-Ray spectral region produced by high-order harmonic generation (HHG) [15].

The goal of this thesis is to further investigate possible applications of intense ultrashort laser pulses to the control of fundamental electronic processes on their natural attosecond time scale. Some of these processes can be studied in the most basic system of isolated gas-phase atoms. However, in many fields, especially the interaction between distinct systems is of great interest. Therefore, to investigate fundamental processes across such system boundaries, the sample under investigation in this thesis is extended to gas-phase dimers.

First, it will begin with the core concepts of strong field-matter interaction to establish the connection between laser electric field oscillation and the electronic dynamics on attosecond time-scales. In the following chapter the methods to produce and characterize intense few-cycle laser pulses are discussed. Furthermore, this chapter presents some details on the applied techniques of target preparation, cold target recoil ion momentum spectroscopy (COLTRIMS) and classical ensemble model simulations. These fundamentals and methods were utilized to achieve the results described in the three main chapters of this thesis. In chapter 4, the process of laser-induced transfer of electron (LITE) in the dissociative multiple ionization of gas-phase argon dimers is discovered to be controllable via the CEP of ultrashort laser pulses [4]. For the same target system, the possibility of atto-second control of electronic excitation by frustrated field ionization (FFI) across system boundaries [7] is investigated in chapter 5. Finally in chapter 6, the technique of stimulated Raman scattering (SRS) is used for efficient spectral broadening and red-shift of ultrashort pulses and exploited to apply control over the HHG process in order to extend the achieved cut-off energy significantly [8].

"Wizards had always known that the act of observation changed the thing that was observed, and sometimes forgot that it also changed the observer too."

— Sir Terry Pratchett, *Interesting times*

Chapter 2

Fundamentals of strong field - matter interaction

In this chapter, the fundamental concepts of strong field - matter interaction that constitute the basis of research results presented in this thesis will be introduced. Broadly speaking, the presented topics can be summarized as modifications of matter by strong laser fields and vice versa, their feedback to the laser field. To simplify the description of these complex, nonlinear processes it was often found useful to split the interaction into three steps and treat them separately [16–19], often referred to as the three-step model of strong-field physics. This will also be the basis of this introduction. In this semi-classical model, electrons are usually treated quantum mechanically as electron wave packet (EWP) and the electric fields are treated classically.

Figure 2 gives an overview of the key processes for this thesis' research topics that will be discussed in more detail in the following sections. In this simplified picture, a molecule interacts with a strong laser field and the above mentioned three steps of (1) ionization, (2) electron propagation in the laser field and (3) recollision are shown in green. A possible outcome after recollision is the generation of XUV radiation, referred to as HHG, which is well described by this three-step model [17]. However, other processes, such as light scattering are not directly tied to this model and are better described by

15
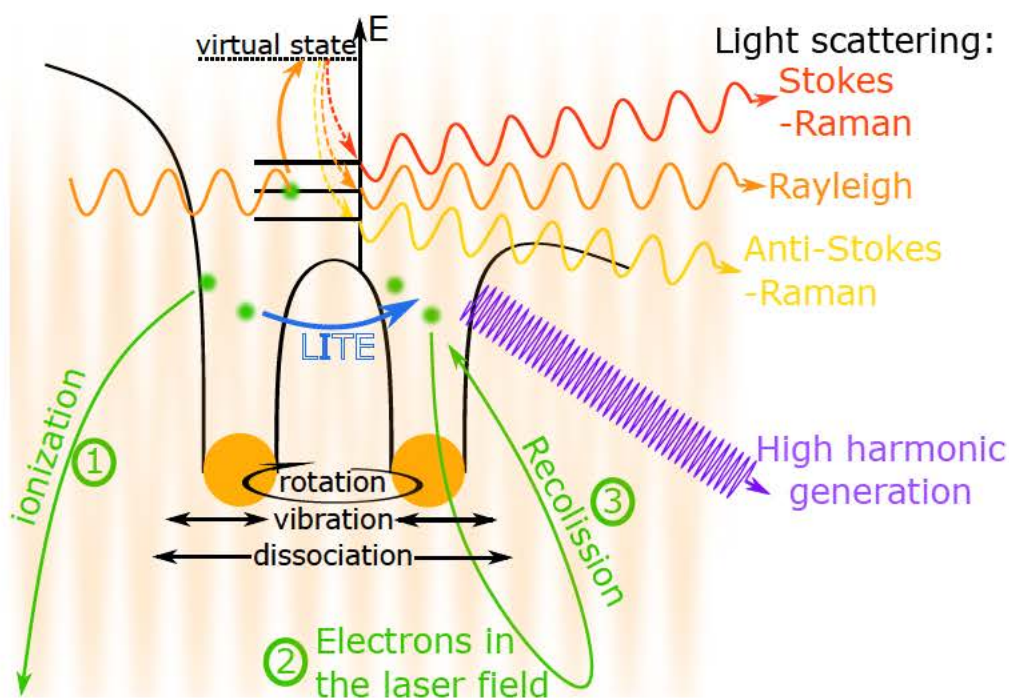
Figure 2: Overview of fundamental processes of strong field - matter interaction that will be discussed in this chapter, as an example shown for a simplified molecular potential in one dimension. Electrons, shown in green, can be completely removed from the system (Ionization). Or, after being driven by the laser field, recollide with their parent ion and trigger a plethora of processes, e.g. HHG. Afterwards, the matter can be left in an excited state or start to dissociate. Also the laser field is modified by the interaction through elastic- (Rayleigh-) and inelastic- ((Anti-)Stokes-Raman-) scattering processes.

their own concepts. Additionally, processes that cannot be present in single atoms, but only be induced by the interaction in clusters or molecules, such as rotational/vibrational excitation or dissociation are indicated in black. Another such example is the process of LITE shown in blue, That was discovered in this thesis and will be a core topic of chapters 4 and 5.

The discussion will at first be limited to single gas-phase atoms and then extended to larger clusters, specifically gas-phase dimers. In these systems all necessary topics for this thesis are covered and therefore further extension of these concepts to larger systems or other phases of matter will be omitted. The Atomic System of Units is used throughout this thesis.
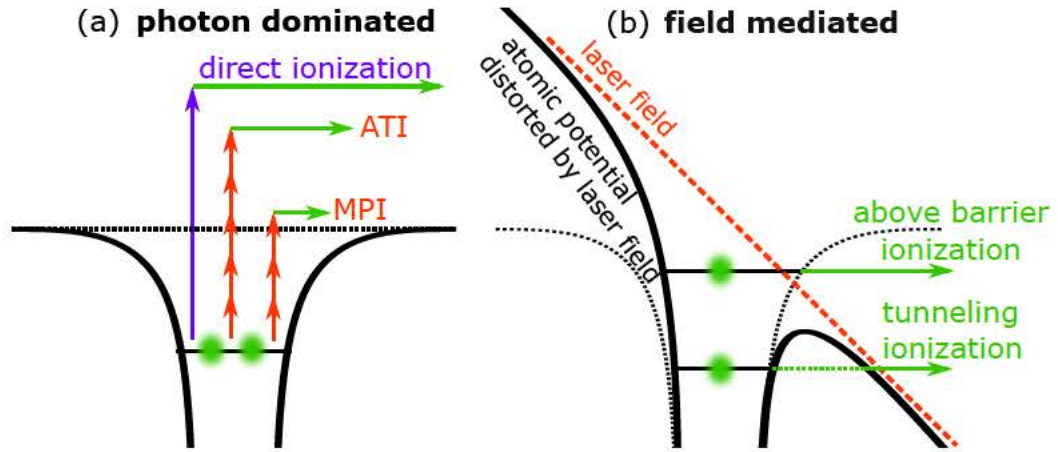
2.1 Ionization

The first step of strong field - matter interaction is ionization, the removal of electrons from the system under investigation. For now we will limit ourselves to a single electron bound by its ionization potential (I_p) in an atom, called single active electron approximation (SAE). This first process is already very complex, however, in many areas (e.g. this thesis) certain further approximations are justified. The first one will be to exclude relativistic effects, which effectively means to neglect the magnetic field component of the laser field. And the second will be the dipole approximation, which means to neglect spatial variations of the impinging electric field and only consider its temporal evolution $\boldsymbol{E} \approx \boldsymbol{E}(t)$. This approximation is appropriate as long as the extension of the EWP is small compared to variations of the laser electric field. With these, the EWP evolves in the combined electric fields of the laser and atomic binding potential $V_0(\boldsymbol{r})$, which can be written as

$$V(\boldsymbol{r}, t) = V_0(\boldsymbol{r}) - \boldsymbol{E}(t) \cdot \boldsymbol{r} \tag{2.1.1}$$

Clearly, this evolution is influenced strongly by the atomic (I_p, electronic structure) and laser electric field parameters (intensity, frequency). And depending on the specific parameters under consideration, two main regimes of ionization that behave differently can be distinguished: photon dominated and field mediated regimes.

These two regimes and certain types of ionization that are associated with them are visualized in Fig. 2.1.1. In the photon dominated regime, encountered for laser fields with relatively high frequency (short wavelength), electrons are ionized by absorption of photons. For the simplest case, direct ionization, photons with an energy $h\nu$ above the atom's I_p are required. For cases where $h\nu < I_p$, multiple photons $n \cdot h\nu > I_p$ have to be absorbed by the electron to liberate it from the atomic potential, so-called multi photon ionization (MPI) [20]. And if even more photons are absorbed than would be required to overcome the I_p, the process at hand is above threshold ionization

Figure 2.1.1: Possible ionization types that can be encountered in strong field - matter interaction shown in their respective regimes. (a) Direct ionization, above threshold ionization (ATI), multi photon ionization (MPI) as photon dominated processes and (b) tunneling-, above barrier- ionization as field mediated processes.

(ATI) [21]. The photoelectron energy spectrum of electrons produced by ATI exhibits peaks that are spaced by the photon energy of the laser field. This process of ATI can also be described as interference of a rescattering EWP delayed by one laser cycle [22, 23] and is also at home in the field mediated regime.

Considering, compared to the photon dominated regime, slower varying laser electric fields of high intensity we enter the field mediated regime. Here the atomic binding potential is periodically distorted by the laser electric field and a potential barrier is formed, through which an electron can tunnel with a certain probability Γ (tunneling ionization). This probability depends exponentially on the ratio between I_p and electric field strength E_0, $\Gamma \propto exp(\frac{-2(2I_p)^{3/2}}{3|E_0|})$ [24]. If the laser electric field changes slowly compared to the time it takes for the electron to tunnel through the barrier, that means the laser field can be considered quasi static, E_0 can be replaced by $E(t)$ and therefore Γ will be strictly tied to the temporal evolution of the laser electric field. Due to this exponential dependence of Γ on $E(t)$, ionization takes places in bursts of attosecond duration synchronized to each laser sub-cycle. ATI can also be observed under such conditions, which can be exploited for

18

the characterization of carrier-envelope phase (CEP) of laser pulses [25, 26] and will be further discussed in section 3.3.2. If the laser electric field is so strong that the atom's potential barrier is distorted to lie below the electron's I_p, the electron can escape the atomic potential which is referred to as above barrier ionization [27].

To distinguish these two regimes of ionization it is insufficient to consider only the frequency of the laser field, at least the interplay between oscillation frequency ω_0, field strength E_0 and ionization potential I_p has to be taken into account. This leads to introduction of the Keldysh parameter [24]:

$$\gamma = \frac{\omega_0 \sqrt{2I_p}}{E_0} \qquad (2.1.2)$$

It compares the oscillation period of the laser field with the hypothetical tunneling time of the electron. For $\gamma << 1$, the field oscillation period is long compared to this tunneling time and the field can be considered quasi static throughout the tunneling step, i.e. field mediated tunneling regime. In the opposite limit of $\gamma >> 1$, the ionization process can be considered as dominated by (multi) photon absorption. However in practice, many experiments are performed with $\gamma \approx 1$ and an unambiguous assignment of ionization regime may not be possible.

2.2 Electrons in the laser field

The second phase of strong field - matter interaction in the three-step model deals with the evolution of the EWP after liberation from its bound state. The incorporation of the ions Coulomb potential is quite difficult and at the same time, for sufficiently strong laser field outside the ionic core, it is plausible to be considered only a small distortion. This leads to the introduction of the strong field approximation (SFA), where the Coulomb potential is completely neglected [24, 28, 29]. With this approximation, often at least qualitative description of and agreement with experiments can be achieved.

To obtain some of the key insights, we will assume an electron being emitted at the position of its ion with zero velocity at time $t = 0$ and can choose the initial conditions after ionization as $(\boldsymbol{r_i}, t_i, \dot{\boldsymbol{r}}(t_i)) = (0, 0, 0)$. Within SFA the electron will be purely driven by the strong laser electric field and its trajectory can be calculated by integration starting from Newton's equations of motions $\ddot{\boldsymbol{r}} = \boldsymbol{F} = -\boldsymbol{E}(t)$. Together with the laser vector potential $\boldsymbol{E}(t) = -\dot{\boldsymbol{A}}(t)$, for the electron's momentum $p(t)$ we can derive

$$\boldsymbol{p}(t, t_i) = \dot{\boldsymbol{r}} = -\int_{t_i}^{t} \boldsymbol{E}(t') dt' = \int_{t_i}^{t} \frac{\boldsymbol{A}(t')}{dt'} dt' = \boldsymbol{A}(t) - \boldsymbol{A}(t_i). \qquad (2.2.1)$$

And considering laser pulses with a limited duration, i.e. vanishing laser field $\boldsymbol{A}(t) \to 0$ for $t \to \pm\infty$, we arrive at

$$\boldsymbol{p}(t_i) = -\boldsymbol{A}(t_i). \qquad (2.2.2)$$

That means the momentum of the EWP after the laser pulse passed is determined by $-\boldsymbol{A}(t_i)$, the negative vector potential at the specific moment of ionization. Which, in the field mediated tunneling regime will be strictly tied to the temporal evolution of the laser electric field on attosecond time scales, as discussed in the previous section.

For a simple linearly polarized laser field and neglecting the laser pulse envelope, the vector potential can be written as $\boldsymbol{A}(t) = -E_0/\omega_0 sin(\omega t)\hat{z}$. With this, the electron's trajectory consists of a term that follows the laser field, oscillating around the ion and a drift term depending on the moment of ionization t_i. The oscillating term will fade together with the laser pulse and only the drift term remains. Not considering possible scattering events, which will be discussed later in section 2.3, the average final kinetic energy of the EWP after the laser pulse interaction can be found as the ponderomotive energy (U_p):

$$U_p = \frac{E_0^2}{4\omega_0^2} = \frac{E_0^2 \lambda_0^2}{16\pi^2}. \qquad (2.2.3)$$

Obviously, due to the dependence of the drift term on t_i, the drift energy specific to a certain trajectory is also connected to the electron's moment of ionization within the laser field and the maximum possible energy acquired of an emitted electron will be $2U_p$. Also U_p will scale linearly with the laser field intensity $I = E_0^2$ and quadratically with its wavelength λ_0.

The more complicated cases of circular and elliptically polarized laser fields will not be derived here, because recollision processes will be suppressed in these cases as the EWP does not return to its parent nucleus [30] and furthermore in this thesis only linearly polarized laser fields will be encountered. After the ionization step the EWP will exhibit a distribution of initial velocities centered around 0 and the EWP will further spread out the longer it propagates in the laser field. This can be partially taken into account as a reduction of probability for recollision processes at long excursion times of the electron.

2.3 Recollision

As discussed above, in a linearly polarized laser field the electron's trajectory will be determined by its ionization time t_i and there exists a strict mapping on attosecond time scales to possible recollision times $t_r = t_r(t_i)$. Because the electron trajectory is a combination of an oscillating and a drift term, a specific trajectory passes by its parent nucleus either never, once or multiple times. However, as the EWP spreads out due to dispersion, the first time the EWP passes close by its parent ion has the highest chance to induce recollision processes. These processes, if triggered, will depend on the properties of the recolliding EWP, e.g. its recollision energy and momentum, that can again be mapped by the corresponding ionization time t_i. Neglecting inelastic scattering events along the way, the highest possible recollision energy will be achieved by a single trajectory with about $3.17U_p$ and ionization time $\omega_0 t_i \approx 17\,\mathrm{deg}$ [31, 32]. This maximum recollision energy within a laser field oscillation is not to be confused with the maximum energy that can be acquired without recollision in total after the laser field has subsided of $2U_p$
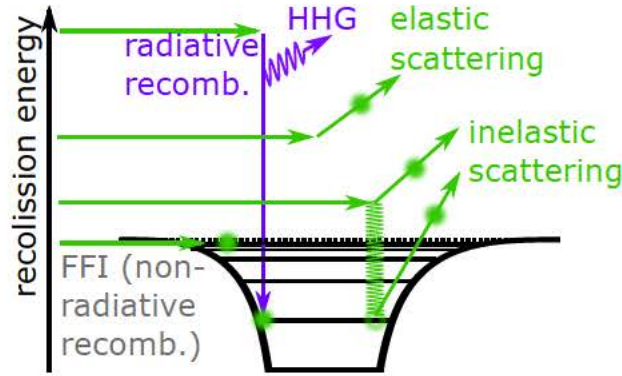
Figure 2.3.1: Common recollision scenarios. Whenever an EWP is driven back to its parent by the laser field, depending on its parameters, there is a chance for recombination with (radiative, HHG) and without emission of a photon (non-radiative, FFI). Also elastic and inelastic scattering with energy deposition in the parent ion (shown as green wavy line) or further ionization are possible outcomes.

mentioned in the previous section. Lower recollision energies than the maximum of $3.17U_p$ can be attained by two possible pathways each, the so-called long- and short- trajectories, of which the short ones will be in many cases of higher importance, again due to the dispersion of the EWP. The change of recollision energy from 0 to $3.17U_p$ within the laser cycle, called atto-chirp, is a useful feature for probing dynamics because it establishes a connection between recollision time and energy on a laser sub-cycle, attosecond time scale [33, 34].

In principle, four processes of the recolliding EWP can be identified, visualized in Fig. 2.3.1 and will be discussed in the following paragraphs and sections: elastic or inelastic electron scattering; and radiative (HHG) or non-radiative recombination (FFI) with its parent ion.

An electron passing by its parent ion can scatter elastically, retaining most of its properties and change only its direction. By this process, the electron can further accelerate and acquire energy in the laser electric field beyond the limit of $2U_p$ established in the previous section, up to an energy of about $10U_p$. This can be observed as a high energy plateau in the ATI spectrum between $2U_p$ and $10U_p$ [35–37]. Due to its sensitivity on $t_r(t_i)$ and the laser

field $E(t)$, it can be exploited for measurement of the CEP of few cycle laser pulses (see section 3.3.2).

On the other hand, an electron can also scatter inelastically and deposit energy in its parent ion. Such an event can excite bound electrons, or even ionize the atom, so-called non-sequential double/multiple ionization (NS-DI/NSMI). Also, excited electrons are more loosely bound by their parent ion and will be more readily ionized during subsequent laser field cycles, so-called recollision-induced excitation and subsequent field ionization (RESI) [38, 39]. Like their elastic counterpart, these inelastic processes are sensitive to the laser field shape and therefore attosecond control of energy deposition into the parent ion by shaping the laser field shape is possible [40–42].

In another type of recollision processes the electron can be recaptured by its parent ion. Depending on the recollision energy, two scenarios can be distinguished. Either the electron's recollision energy is negligibly low, such that the electron can be recaptured by the long range Coulomb potential of its parent ion, then this can happen non-radiative, without the emission of a photon, which is called frustrated field ionization (FFI) [43]. For the other scenario, the electron's recollision energy is higher than the binding energy of its recaptured state and the excess energy is converted into a photon, a radiative recombination process or so-called high-order harmonic generation (HHG) [17, 44]. Because these two recombination scenarios are of key interest in chapters 5 and 6, they will be discussed more detailed in the following two sections.

2.4 Frustrated field ionization

As mentioned above, if an EWP after ionization and propagation in the laser field returns with a low kinetic energy, it can be recaptured in an unoccupied state by the long range Coulomb potential without emission of a photon. Due to the increasing density of unoccupied states towards the continuum, i.e. for increasing principal quantum number n, an electron is more likely to be recaptured non-radiative in such a high lying state, a so-called Rydberg

state [43, 45–49].

These states are named after Johannes Rydberg and his formula to describe the wavelengths λ_{12} of spectral lines of hydrogen-like elements,

$$\frac{1}{\lambda_{12}} = RZ^2(\frac{1}{n_1^2} - \frac{1}{n_2^2}), \tag{2.4.1}$$

with R the element specific Rydberg constant, Z the atomic number and $n_1(n_2)$ the lower (higher) principal quantum number of the atomic electron transition that emits with λ_{12}. These Rydberg states have interesting properties that can be described by their principal quantum number n [50, 51]: They extend much farther away from the ionic core than the ground state as their size increases with n^2. Also they can be quite long lived as their natural lifetime scales with n^3. And even though their binding energy decreases with $1/n^2$, Rydberg states that were populated by FFI can still survive until the strong laser field has subsided [43]. Although Rydberg states were historically introduced for hydrogen-like atoms, for sufficiently large principal quantum number n they exist also in more complex systems such as molecules or clusters [52].

Due to their features, Rydberg states are of interest to many different scientific fields. For instance, as a result of their relatively high energy and size they can initiate complex dynamics in molecules [53–61] and additionally their long lifetime makes them interesting for quantum information applications [51, 62] to name only a few works related to Rydberg atoms.

As established in the previous sections, the electron's recollision energy and by that also the Rydberg state that can be populated by FFI are tied to the ionization and recollision timing dictated by the laser waveform. Therefore there is a possibility to control the formation of high lying Rydberg states and subsequent processes on attosecond time scales by careful shaping of laser pulses [47].
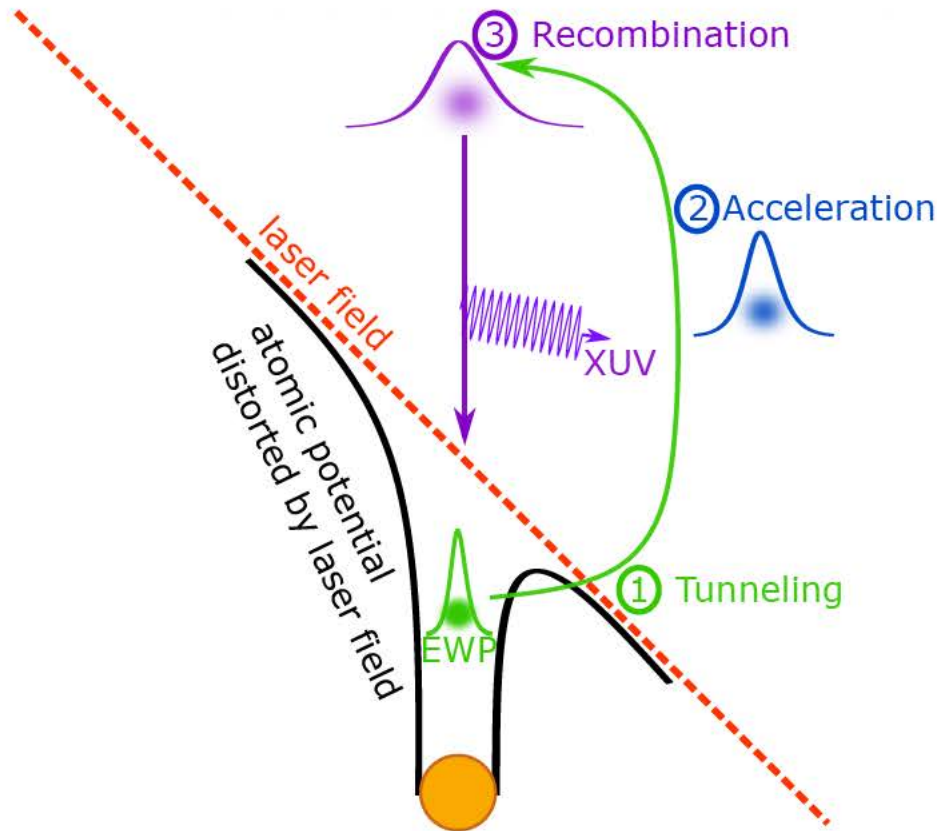
Figure 2.5.1: Three-step model of strong field physics for the case of HHG. The atomic potential is distorted by the laser field and an EWP can tunnel through the suppressed Couloumb barrier (1). The EWP gains energy by acceleration in the laser field (2) and upon return there is a chance of radiative recombination under emission of an XUV photon (3).

2.5   High harmonic generation

The complementary process to FFI is the recapture of an electron under emission of a photon. Historically this was observed as high energy harmonic radiation spaced by twice the fundamental photon energy of the inciting laser pulse beyond what could be achieved by perturbative nonlinear processes and therefore called high-order harmonic generation (HHG) [17, 44]. Because the energy of generated photons depend on the electron's recollision energy which can reach hundreds of eV and even keV, HHG is exploited to produce XUV and soft X-ray laser pulses.

On the microscopic level, the HHG process is well described by the three step model already discussed in sections 2.1 to 2.3 and will be briefly repeated here and in Fig. 2.5.1 in the context of HHG. A strong laser field can distort an atomic potential so that a Couloumb barrier is formed, through which electrons can tunnel (1). Then the liberated EWP is accelerated and returned to its parent ion by the laser field (2). And, finally, there is a chance that the recolliding EWP is captured in its former bound state (3), upon which the electron's surplus energy is converted into a high energy photon. The maximum achievable photon energy, the HHG cut-off energy $E_{cut-off}$, will be determined by the maximum recollision energy plus the electron's binding potential: $E_{cut-off} \approx 3.17U_p + I_p$ [17, 32].

Because this cut-off energy scales with the ponderomotive energy U_p, for a given atomic species with a fixed I_p, we can write $E_{cut-off} \propto I\lambda_0^2$. However, there are limitations to this cut-off scaling in both variables. For increasing intensities, the atom's ground state could become depleted before the peak of the laser field intensity. Which means that there would be no electrons available at ionization times t_i corresponding to the maximum recollision energies. And for longer wavelengths, the EWP propagates longer in the laser field, therefore it spreads stronger, which reduces the probability of the recombination step. By this, the achievable photon flux Φ is reduced drastically for increasing wavelength as $\Phi \propto \lambda^{-5} - \lambda^{-6}$ [63, 64]. This combination of scaling relations also establishes, that for targeting a specific spectral region by HHG, there is an optimal wavelength of the driving laser, which will be the shortest one which still allows to cover the desired cut-off energy.

For multicycle laser pulses, during every laser half-cycle a burst of high energy photons with a continuous spectrum up to $E_{cut-off}$ is generated. These attosecond pulses are interfering in time and the resulting spectrum of such an attosecond pulse train consists of a comb of odd multiples of the driving laser field's photon energy $h\nu_0$ up to $E_{cut-off}$. As described in the previous sections, also for HHG the laser electric field shape dictates the relationship $t_r(t_i)$ and possible recollision energies. Therefore also the process of HHG can be controlled on attosecond time scales by carefully tailored strong laser
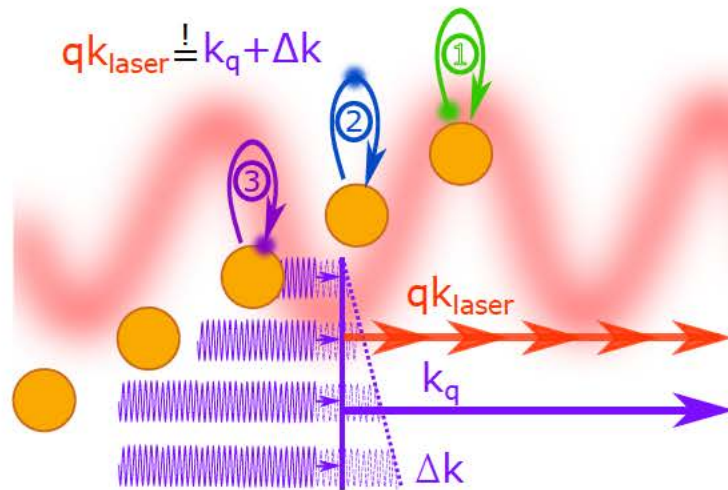
Figure 2.5.2: For HHG in a dilute gas to be efficient, the harmonic emission from different locations in the gas is required to add up in phase. Integer multiples of the wave vector of the driving laser (qk_{laser}) have to be balanced with the wave vector of generated harmonics (k_q) by the sum of all additional phase-mismatch contributions (Δk).

fields. In many spectroscopic applications broad, continuous spectra (single isolated attosecond pulses) are preferred over a harmonic spectrum (pulse train). This can be achieved by a variety of techniques that usually boil down to shaping the laser field such that the harmonic emission is restricted to a single pulse, for instance amplitude gating [65] or polarization gating [66].

On the macroscopic level, for HHG to be effective, the emission from many atomic sources within the gas medium has to add up coherently [67]. A simplified picture of this requirement is shown in Fig. 2.5.2. For HHG, and any other nonlinear optical frequency conversion process, the phase velocities, or precisely wave vectors, of fundamental driving laser k_{laser} and upconverted radiation k_q ideally should match. This phase matching ensures that throughout the propagation of the laser field the generated harmonic radiation builds up, independent of the position of atomic emitters within the medium.

However, naturally, the phase velocities of fundamental and generated laser fields in any medium will be different and additional sources of phase mis-

match Δk, such as plasma dispersion, play a critical role. In total to achieve phase matching in HHG, integer multiples of the wave vectors of driving laser qk_{laser} and generated harmonics k_q have to be balanced by the sum of all sources of phase mismatch Δk: $qk_{laser} = k_q + \Delta k$. For a perfect balance with the remaining mismatch $\Delta k \to 0$, the coherence length for HHG $L_{coh} = \pi/\Delta k$ could grow arbitrarily large. But in reality, this is difficult to achieve for a broad range of harmonics. Furthermore, because generated XUV and soft X-ray radiation is absorbed in the gas, the effectively useful medium length for HHG is limited to about 5-10 absorption lengths [68].

There exist various techniques to enhance phase matching that involve solutions in spatial and/or temporal domain [67], that all have in common a strong gas pressure dependence of the phase mismatch Δk. Therefore optimization usually involves a scan of the employed gas pressure. For the experiments described in chapter 6, a tight focusing geometry and a gas filled cell with variable cell length and position is used for HHG.

Here, it shall only be briefly mentioned that HHG is also performed in other types of media than mono-atomic gas, such as molecules [69], plasmas [70], liquids [71] or solids [72], that each have their own applications.

2.6 Strong field driven processes in gas-phase dimers

So far this chapter dealt with the interaction of a strong laser field with single isolated gas-phase atoms to describe the fundamentals in the most basic systems possible. However, due to the highly practical importance for chemical, environmental, biological and computer sciences (and probably many more) the extension of these fundamentals to more complex systems, such as molecules, clusters, nanoparticles and also solids, is generally desired.

One way to achieve this is by building upon insights acquired in the simplest possible systems. As chapters 4 and 5 investigate fundamental processes across system boundaries, we are here specifically interested in the most

simple system where such a system boundary can be studied: atoms bound by van der Waals (vdW) force forming dimers [73]. The bonding in such a vdW dimer is induced by fluctuating polarizations with dissociation energies of few meV and no covalent or ionic bonds present between the monomers. For molecular dimers, the vdW force depends on the relative orientation of the monomers to each other, but for noble gas dimers it can be considered isotropic. In this weakest form of chemical bonding no orbitals are shared between the monomers and thus they can be seen as closely spaced but individual quantum systems [74]. Therefore, we will discuss now here briefly, and more detailed in chapters 4 and 5, additional considerations that have to be taken into account and processes that become possible when we increase the system size to such gas-phase vdW dimers.

Clearly, due to their spatial extension, the distance between the monomers R_{12} has to be taken into account. Also the orientation angle θ of the dimer relative to the polarization direction of the laser field will be important for the ionization and recollision dynamics induced by a laser field. To stick with the nomenclature introduced in previous sections, for dimers the relation between ionization and recollision timing needs to be extended to $t_r(t_i, R_{12}, \theta)$. These additional spatial degrees of freedom are not necessarily static, thus may change during the interaction with a laser field depending on the vibrational and rotational state of the dimer. This ionic motion is typically slow compared to that of the electrons, but cannot be easily neglected. At this point it was not even considered what happens when an electron of one monomer recollides with the other monomer. To summarize, already for this still quite simple system, it can be considered more fruitful to gain insights via simulations rather than strive for analytical solutions. For this, see sections 3.6 and chapters 4 and 5.

Furthermore, additional processes are present in a dimer that cannot be observed in mono atomic systems. The most obvious is dissociation, which can be induced by ionization or excitation of aforementioned vibrational or rotational states. However, such ionized or excited states can also cause the dimer to be more tightly bound due to increased polarizability. For instance,

for the argon dimer Ar_2 a dissociation energy of about $12\,meV$ is required [75], whereas the singly ionized argon dimer Ar_2^+ requires $1.3\,eV$ [76].

Another process that would be impossible in a mono atomic system is that an freed electron can recollide upon another entity than its own parent ion. There it can, at least transiently, be captured, a process which we will call laser-induced transfer of electron (LITE) and is described in detail in chapter 4. In principle upon recollision with its neighbor, all processes discussed in section 2.3 are also possible at the distant entity. And FFI, of which the result is equivalent to electronic excitation, across a system boundary is explored in chapter 5.

All processes discussed so far in this chapter can in principle be extended to larger systems, however, complexity increases quickly with system size, as geometry, additional degrees of freedom, collective effects and the interplay between constituents of the systems become important. For such large systems, more specialized models and techniques are required for their satisfactory description, which are beyond the scope of this work.

2.7 Light scattering on gas-phase molecules: Raman scattering

In chapter 6 the method of SRS in a hollow core fiber (HCF) plays a key role for the achieved results. Here the basic concepts of SRS are introduced and later in section 3.2.2 it will be discussed how these fundamentals can be exploited for efficient spectral broadening and simultaneous red-shift in a HCF. In contrast to mechanisms covered so far by the three step model in sections 2.1 to 2.6, ionization of the medium is a competing process to SRS and ideally should be avoided. This is done by choosing the laser beam diameter so that the laser peak intensity stays below the critical limit for ionization and scattering becomes the dominant interaction between light and matter.

Light scattering can be categorized into three domains based on a relative size

Figure 2.7.1: Schematic overview of light scattering on particles that are small compared to the wavelength of incident light. A photon can be absorbed, by which the system is excited to a virtual state. Subsequent re-emission of a photon can leave the system in the same state as before (Ralyeigh scattering). Alternatively, vibrational or rotational states can be excited and the emitted photon is of higher (Anti-Stokes-Raman) or lower (Stokes-Raman) energy.

parameter between scattering object D and incident wavelength $a = \pi D/\lambda$ and have to be handled distinctly. These domains are geometric scattering for large obstacles $a >> 1$, Mie-scattering when scatterer and wavelength are on the same order $a \approx 1$ [77] and Rayleigh-Raman scattering for small objects $a << 1$ [78, 79]. Here we are interested in the scattering of light with wavelengths in the near infra-red (NIR) range on small gas-phase molecules, especially the output of an ytterbium laser systems at $1030\,\mathrm{nm}$ scattering on nitrogen molecules with a size of about $0.3\,\mathrm{nm}$. Thus with $a \approx 10^{-3}$, we are well in the Rayleigh-Raman scattering regime. Scattering in this regime is pictured in Fig. 2.7.1.

For not too strong laser fields, MPI or tunneling ionization processes will not be present and photon energies in the NIR regime ($h\nu_0 < 1.5\,\mathrm{eV}$) are insufficient for direct ionization. Instead, electrons can be excited by photon absorption to short lived virtual states and subsequently recaptured in their former electronic state under emission of a photon. In atoms this happens elastically, i.e. absorbed and emitted photon are of the same energy and only the directions is changed (Rayleigh scattering) [78]. In molecules, there is

an additional chance for inelastic scattering where the molecule is left in the same electronic, but a different vibrational or rotational excited state than initially [79, 80]. Due to energy conservation, the emitted photon is bound to be of lower (Stokes-Raman) or higher (Anti-Stokes-Raman) energy, which will be called a Raman shifted photon. Naturally, for a gas in thermodynamic equilibrium, the lower states will be initially stronger populated and therefore Stokes-Raman scattering to lower photon energies (longer wavelengths) will be dominant, leading to a net red-shift of Raman photons. Typically, compared to the incident light, relative scattered intensity will be in the range of $10^{-3} - 10^{-4}$ for Rayleigh and 10^{-7} for Raman scattering [81].

Generally, Raman scattering happens spontaneously, in random time intervals, but it can also take place as stimulated Raman scattering (SRS) when photons of suitable wavelength are present. These can either be produced beforehand by spontaneous Raman scattering or simultaneously injected, e.g. by laser pulses with a sufficient bandwidth to cover the molecule's vibrational and/or rotational excited states. The probability for such SRS increases with the number of Raman shifted photons, therefore it is self-enhancing and the Raman shifted light is amplified at the expense of the incident fundamental light. Later, in section 3.2.2 a method for spectral broadening and simultaneous continuous red-shifting of laser pulses will be discussed where, SRS is cascaded due to an increased interaction length in a stretched HCF.

"You're not supposed to eat like that,' said Gurder severely. 'You're not supposed to shove it all in your mouth and then cut off what won't fit."

— Sir Terry Pratchett, *Wings*

Chapter 3

Methods

Unlike in a dinner context, methods in the scientific world do not necessarily have to be clean, however, a kind of elegance is preferred in both cases. Setting the introduction joke aside, we elegantly turn to the topics at hand. In this chapter, the techniques employed to achieve the results presented in this thesis are discussed. It will start with ultrafast lasers and an overview of the two laser system that were used, a titanium doped sapphire (Ti:Sa) and an ytterbium based system. Both of these laser systems are capable of producing laser pulses with durations in the fs regime, however, further pulse preparation in the form of post-compression by either self phase modulation (SPM) or stimulated Raman scattering (SRS) in a hollow core fiber (HCF) and chirped mirrors is required for the experiments presented in this thesis. Additionally, pulse characterization techniques of second harmonic generation frequency resolved optical gating (SHG FROG) and carrier-envelope phase (CEP) tagging will be introduced. For chapters 4 and 5 further methods are prerequisite. The process of target preparation and method of cold target recoil ion momentum spectroscopy (COLTRIMS) will be shown. Finally, details on the used classical ensemble model simulation are given.

3.1   Ultrafast lasers

To control processes on an attosecond time scale we need a way to act and observe at this time scale. The method for this has been provided by the advent of ultrafast laser technology, nowadays routinely capable of producing intense laser pulses with durations below few hundred femtoseconds. Further temporal compression down to a regime where a laser pulse consists of only few laser cycles gives a tool for attosecond control over fundamental electronic processes based on their critical dependence on the laser electric field, as has been established in chapter 2. Another technique to achieve attosecond control would be via attosecond pulses as can be produced by HHG. However, within this thesis, HHG will be investigated as a process we want to control rather than a method for exploration.

Typically, the generation of intense ultra short laser pulses is based on two key technologies, which are mode-locked lasers [82, 83] and chirped pulse amplifier (CPA) [84].

Any laser systems produces light in a certain spectral bandwidth as limited by the bandwidth of the gain medium where laser light is amplified. Within this bandwidth, the optical cavity restricts the produced output to certain longitudinal modes that will interfere constructively with themselves after each roundtrip in the cavity. In a mode-locked laser, the phase relation between many of these longitudinal modes is locked instead of fluctuating randomly. Periodically, all the locked modes interfere constructively with each other and produce intense ultra-short laser pulses spaced in time by the cavity roundtrip time. There exist several active and passive techniques for mode-locking, of which the shortest pulse durations (sub 5 fs possible) are achieved by passive Kerr-lens mode-locking [85, 86]. Here, the optical Kerr-effect is utilized to induce an light intensity dependent lens into the cavity such that laser pulses with highest intensity (shortest duration) experience the largest gain from the cavity.

Until the introduction of CPA, further amplification of such intense ultra short laser pulses was limited by the damage threshold of gain media and

onset of detrimental nonlinear effects, such as undesired self focusing or self phase modulation (SPM). In a CPA, prior to amplification, the frequency components of an ultrashort laser pulse are separated, usually such that low frequency components (red) travel a shorter distance than the high frequency (blue) ones. In other words, a so-called positive chirp is introduced to the laser pulse, stretching its pulse duration by a large factor. By this the peak intensity of the laser pulse is drastically reduced and stays below the threshold of unwanted nonlinear effects throughout amplification. Afterwards, the chirped and amplified laser pulses are re-compressed, for instance by a grating or prism compressor. There exist numerous realizations of CPA with different combinations of stretching, amplification and compression techniques.

For the performed experiments, two different ultrafast laser systems were used. Both are based on the CPA design and their key distinction can be found in the employed gain medium for amplification, which is either titanium doped sapphire (Ti:Sa) or ytterbium-doped calcium fluoride (Yb:CaF$_2$).

3.1.1 Ti:Sa laser system

A schematic overview of the Ti:Sa laser system and its post compression, used for the experiments described in chapters 4 and 5, is shown in Fig. 3.1.1.

Laser pulse generation starts with the *Femtolaser* 'Rainbow' oscillator, a passively Kerr-lens mode-locked Ti:Sa laser pumped by a *Coherent* 'Verdi V5' laser at 532 nm (green). Its output of about 7 fs pulses with a center wavelength of 790 nm and a repetition rate of 80 MHz are temporally stretched and chirped in a piece of SF57 glass to pico-second duration. These pulses are then amplified in a home-built, cryogenically cooled Ti:Sa multi-pass amplifier, which is pumped by a dedicated pump laser, a Q-switched Nd:YLF laser (1054 nm) frequency doubled to 527 nm. The chirped laser pulses from the oscillator pass a total of ten times through the amplifiers Ti:Sa crystal. After the first four passes, to match the repetition rate of the pump, 5 kHz of pulses are picked for further amplification up to pulse energies of 0.8 mJ. With the addition of manipulation of third order dispersion (TOD)
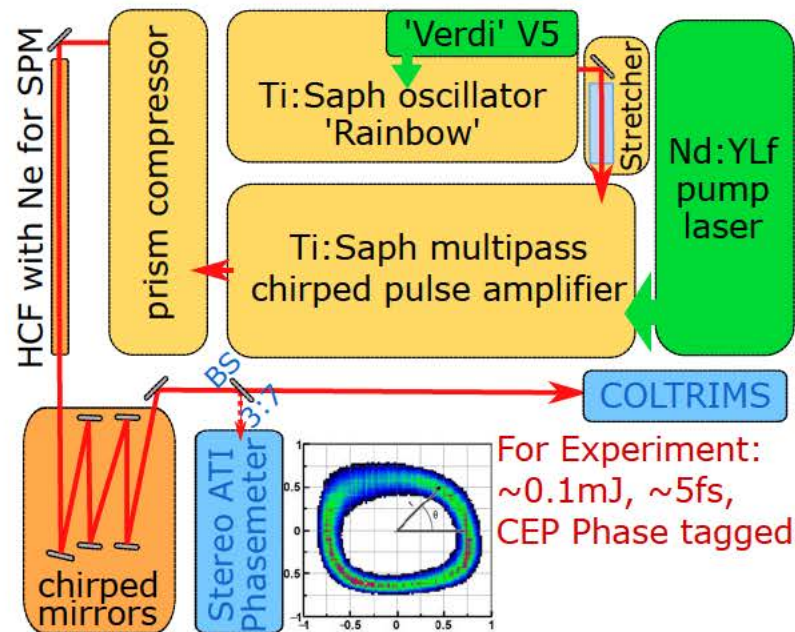
Figure 3.1.1: Schematic of the Ti:Sa based laser system used for the experiments described in chapters 4 and 5. Shown in green are the two pump lasers for the Ti:Sa oscillator and amplifier systems. Laser pulses from the oscillator are temporally stretched in a piece of SF57 glass, amplified in a 10-pass Ti:Sa amplifier and then compressed in a prism compressor. After further pulse preparation by SPM in a neon filled HCF and chirped mirrors a beamsplitter (BS) sends about 30 % of the laser beam to CEP characterization. About 0.1 mJ, 5 fs pulses with a repetition rate of 5 kHz are available for the experiments.

by an acousto-optic programmable dispersive filter (AOPDF, or so-called DAZZLER)[87] and after temporal compression by a double prism compressor, transform limited pulses of about 25 fs duration can be achieved. The transform limited pulse duration increases during amplification process due to gain narrowing that limits the bandwidth of laser pulses. Further pulse preparation is done by spectral broadening by SPM in a neon filled 1 m HCF and subsequent temporal compression by chirped mirrors (see section 3.2). In the end, laser pulses of about 0.1 mJ and 5 fs with center wavelength of 790 nm and a repetition rate of 5 kHz are available for the experiments.

In general, Ti:Sa laser systems operate most efficiently around 800 nm, but their tuning range extends from 650 nm to 1100 nm. This very large gain bandwidth is their biggest advantage, as it allows for the generation of ultrashort intense laser pulses. They also enjoy a wide range of possible pumping wavelengths, however these are situated in the green spectral region which is not easily accessible. Even though there exist the possibility for Ti:Sa laser systems to be directly pumped by diodes in the blue (450 nm)[88] or green (520 nm)[89], typically the pumping of Ti:Sa systems involve multiple conversion steps that add to complexity and cost. For instance, for the system above: pump-diodes at 808 nm $\rightarrow$ Nd:YLF laser 1054 nm $\rightarrow$ frequency doubled to 527 nm to pump Ti:Sa amplifying around 790 nm. Independent of the used pumping scheme, efficiency and power scalability of Ti:Sa lasers suffer fundamentally from their large quantum defect ($1 - \frac{\lambda_{pump}}{\lambda_{laser}} \approx 32\%$ for Ti:Sa), the energy that is lost as heat during conversion from pump to laser [90].

3.1.2 Ytterbium laser system

A schematic overview of the ytterbium laser system and its post compression, used for experiment of chapter 6, is shown in Fig. 3.1.1.

The ytterbium laser systems also follows a typical CPA scheme [91]. It uses commercial 'Pharos' from *Light Conversion*, a combination of master-oscillator and preamplifier, diode pumped, ytterbium laser as a seeder of
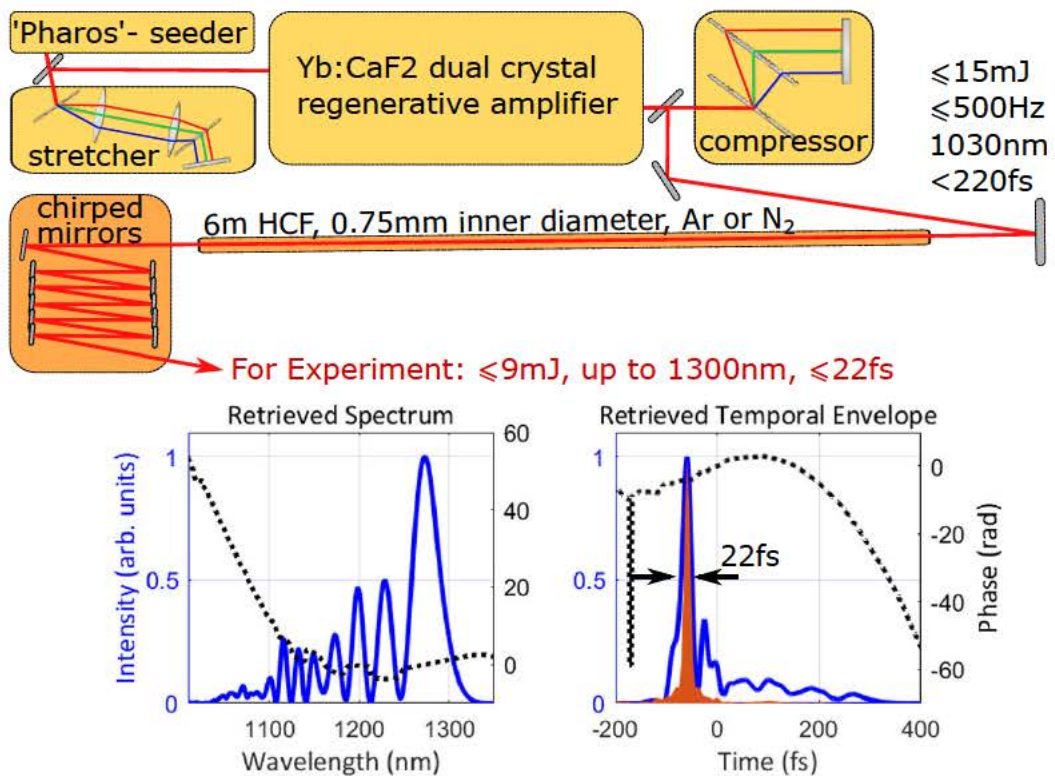
Figure 3.1.2: Schematic of the ytterbium based laser system used for the experiment described in chapter 6. Shown in yellow are the main buildings blocks of the all-diode pumped ytterbium CPA system. Laser pulses from a *Light Conversion* 'Pharos' laser are stretched and seed a dual crystal regenerative amplifier before being re-compressed. Further pulse preparation is achieved by either SPM or SRS in a HCF and chirped mirrors. For the experiment up to 9 mJ, sub-22 fs pulses with a repetition rate of 500 Hz were available.

sub-mJ, femtosecond laser pulses with a center wavelength at 1030 nm. They are stretched to 500 ps in a Martinez-type stretcher [92], containing two antiparallel diffraction gratings with a telescope in between. Then the stretched pulses are amplified up to 15 mJ in a cryogenically-cooled, diode pumped, regenerative amplifier with two Yb:CaF$_2$ crystals as gain medium. In a regenerative amplifier, in contrast to the multi-pass design of the above discussed Ti:Sa system with a fixed number of amplification steps (10), a light pulse is injected into a resonator, where it is amplified in an adjustable number of roundtrips before being ejected by a fast electro-optic switch. The amplified pulses are then compressed in a Treacy-type compressor [93] to sub 220 fs duration. The combination of Martinez-type stretcher and Treacy-type compressor, matched to each other, allows to stretch a pulse in time to almost arbitrarily and then compress it to its original duration without distortion [94]. This system can operate at repetition rates between 500 Hz and 10 kHz. For further pulse preparation SPM (or SRS) is applied for spectral broadening (and red-shift) in a argon (nitrogen) filled 6 m long stretched HCF with inner diameter 0.75 mm (*Few-cycle Inc.*) and subsequent temporal compression by chirped mirrors (see section 3.2). In the end, laser pulses of up to 9 mJ, <22 fs with center wavelength of 1030 nm (1230 nm for SRS) and a repetition rate of 500 Hz are used for the HHG experiments.

For the experiments, the key differences of the ytterbium system compared to the Ti:Sa system are the longer wavelength and higher pulse energy, which are both beneficial for the HHG experiment of chapter 6 (see also section 2.5). In general, ytterbium based laser gain media feature a narrower gain bandwidth and therefore do not directly support as short laser pulses as compared to Ti:Sa, but post compression techniques are still applicable and comparable pulse durations can be achieved [95]. The large advantage of ytterbium based system is that they can be pumped at 970 nm to produce laser light at 1030 nm giving it a very small quantum defect of about only 5%. this in combination with the possibility to be directly pumped by diodes, gives ytterbium the capacity for efficient scalability to high laser powers.

3.2 Pulse preparation

As a property of Fourier transformation we know that for a given pulse shape, the product of temporal duration and spectral bandwidth will have a minimum value, e.g. ~ 0.44 for gaussian pulses. Therefore for any spectral bandwidth there is a shortest supported pulse duration, a so-called transform limited pulse. The performed experiments required laser pulses with shorter pulse durations than would be supported by the spectral bandwidth provided by the used laser systems directly and therefore additional pulse preparation was applied. For this, at first the laser pulses will be spectrally broadened by either SPM or SRS in a gas filled HCF to support shorter pulse duration and then temporally compressed by chirped mirrors.

3.2.1 Self phase modulation

Due to the Kerr-effect the refractive index n of a material is changed proportional to the square of an applied electric field $n_{Kerr} \propto E^2 \propto I$. For this no external electric field is necessary, the laser electric field of a propagating light pulse will modify the materials refractive index also for itself as

$$n(I) = n_0 + n_{Kerr} = n_0 + n_2 \cdot E^2 = n_0 + n_2 \cdot I, \qquad (3.2.1)$$

with n_2 the second order nonlinear refractive index. This Kerr-effect is the reason for nonlinear optical effects of self-focusing and SPM [96, 97]. The case of SPM is illustrated in Fig. 3.2.1 and will be discussed now.

Clearly, for any laser pulse the intensity $I(t)$ and by the Kerr-effect also the refractive index change over time $n(I) \to n(t)$. This in turn causes a change of instantaneous phase $\phi(t)$ of the laser pulse after a distance L traveled in the medium:

$$\phi(t) = \omega_0 t - kz = \omega_0 t - \omega_0 L n(t), \qquad (3.2.2)$$

with ω_0 the fundamental laser frequency. This phase shift in turn causes a
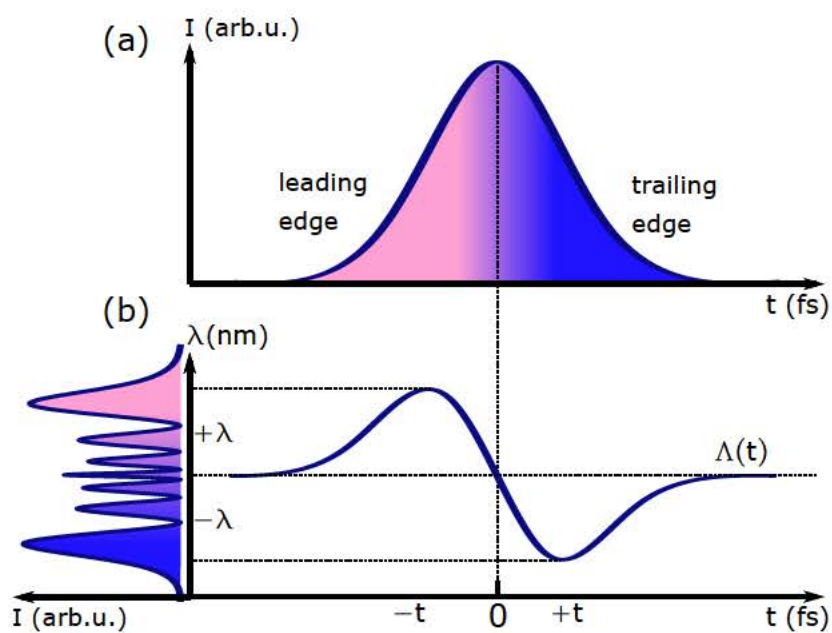
Figure 3.2.1: Demonstration of SPM: (a) Envelope of the field intensity I over time t and (b) corresponding change of instantaneous wavelength $\Lambda(t)$ caused by SPM for a gaussian laser pulse. For an initially un- or up-chirped laser pulse, due to the nearly instantaneous response of SPM this leads to a symmetric spectral broadening displayed on the left. The leading (trailing) edge of the laser pulse will be red- (blue-) shifted, indicated by the red (blue) shading in (a).

change of instantaneous frequency/wavelength $\omega(t) = \frac{2\pi}{\Lambda(t)}$:

$$\omega(t) = \frac{d\phi(t)}{dt} = \omega_0 - \omega_0 L \frac{dn(t)}{dt} = \omega_0 - \omega_0 L n_2 \frac{dI(t)}{dt} = \frac{2\pi}{\Lambda(t)} \qquad (3.2.3)$$

For any symmetric laser pulse intensity, e.g. a Gaussian shape $I(t) \propto exp(-t^2)$, this instantaneous response causes a symmetric spectral broadening. In an initially un- or up-chirped laser pulse the leading edge of the laser pulse will be shifted to longer (red), while the trailing edge is shifted towards shorter (blue) wavelengths. This SPM does not by itself change the temporal pulse envelope of the laser pulse, however dispersion acts simultaneously on the laser pulse and for normal dispersion this will lead to a temporal broadening. Even though this temporal broadening seems to be in conflict with the stated goal of shortening the pulse duration, the spectral broadening achieved by SPM gives the laser pulse the potential to be subsequently temporally compressed below its initial pulse duration, e.g. by chirped mirrors (see section 3.2.3). A typical SPM spectrum shows strong oscillations due to interference of the same wavelength being produced at two different times within the laser pulse, exemplified in Fig. 3.2.1(b).

To increase the effect of SPM, the pulse intensity has to be kept high over long distances L, this is typically achieved by propagating the laser pulses in a gas filled HCF [98]. Pulse energy for SPM in a HCF is limited by ionization of the gas or self focusing and can be increased with the core diameter of the HCF. Due to their high ionization potential, typically noble gases are used.

3.2.2 Stimulated Raman scattering

For a detailed description of SRS in HCFs see [99] and corresponding supplemental material, which will be summarized here. In principle, SRS in a HCF can be understood in the same way as SPM, but with an additional term to the material's refractive index due to SRS n_{Raman} in a molecular gas, which can be described by

$$n_{Raman} = \int_{-\infty}^{\infty} R(t-t')I(t)dt', \qquad (3.2.4)$$

with R the Raman response function. This Raman response function can be approximated by a damped sine function with two time constants τ_1, τ_2, characteristic to the material

$$R(t) = \frac{\tau_1^2 + \tau_2^2}{\tau_1 \tau_2^2} sin(t/\tau_1)e^{(-t/\tau_2)}. \qquad (3.2.5)$$

For nitrogen, as is used in the experiment in chapter 6, these time constant are $\tau_1 \approx 62\,\mathrm{fs}$ and $\tau_2 \approx 120\,\mathrm{fs}$, well on the order of employed pulse duration of about $220\,\mathrm{fs}$. Therefore, the change of phase $\delta\phi(t)$ cannot be considered to be following the intensity profile of the laser pulse $I(t)$ instantaneously as in the case of SPM. Instead it will reach its maximum in the trailing edge of the laser pulse, leading to a asymmetric spectral red-shift.

However, to explain the experimentally observed spectra, in addition to the temporal intensity profile of the laser pulse also the spatial intensity profile $I(t, r, z)$ has to be taken into account in a full three dimensional modeling. By this, it can be found that SRS also manifests as a nonlinear lens which induces a steepening of the trailing edge of the laser pulse. In addition, this non-linear lens excites higher order waveguide modes. These modes have mismatched group velocities, thus walk off away from each other and intensity decreases. This is strongest at the maximum of $\delta\phi(t, r, z)$ and therefore further steepens the trailing edge of the laser pulse.

Based on this, the effect of SRS in a nitrogen filled HCF can be modeled as shown in Fig. 3.2.2, which is adapted from [99]. A laser pulse modified in such a way will have a long, flat leading and steep trailing edge. As the maximum of $\delta\phi(t, r, z)$ lags behind the maximum of laser pulse intensity, it will increase throughout almost the entire pulse. By that, the majority of the laser pulse will be shifted towards longer wavelengths and only the trailing end of the laser pulse will instead experience a shift to shorter wavelengths.
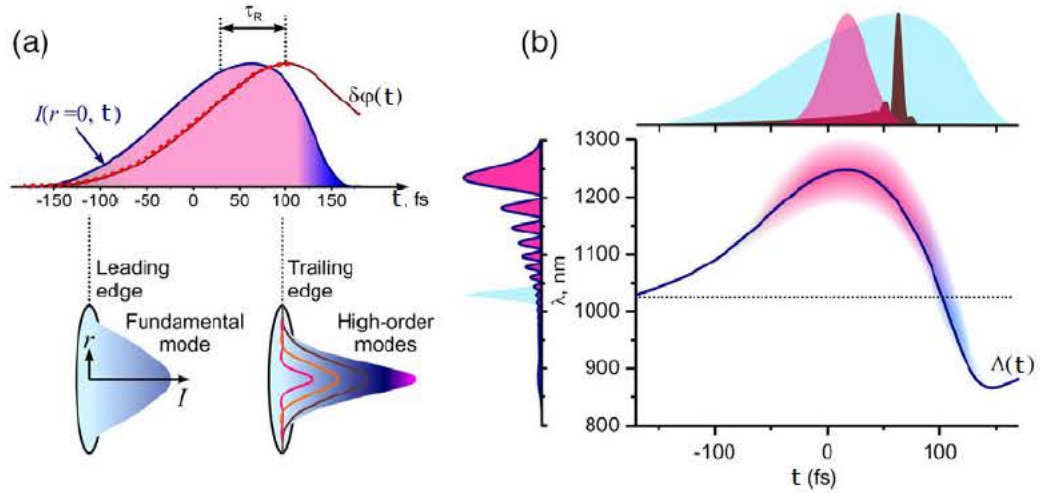
Figure 3.2.2: Demonstration of SRS: (a) Envelope of the field intensity I over time t and temporal phase $\delta\phi(t)$ induced by the delayed response of rotational excitation. Portions of the pulse that are red- or blue- shifted are indicated by a respective shading. Beam profiles in the leading and trailing edges of the pulse are shown below. Due to the delayed response and interplay between higher order modes, the laser pulse will be asymmetrically red-shifted. (b) Change of instantaneous wavelength $\Lambda(t)$ caused by SRS is shown in the main panel. In the upper panel field intensity envelopes of the fiber output (blue), the compressed pulse (brown), and the fiber output transmitted through a 1450-1650 nm bandpass filter (red) are shown. The left panel displays the input spectrum (blue) and the red-shifted spectrum after the HCF (red). Figure adapted from [99].
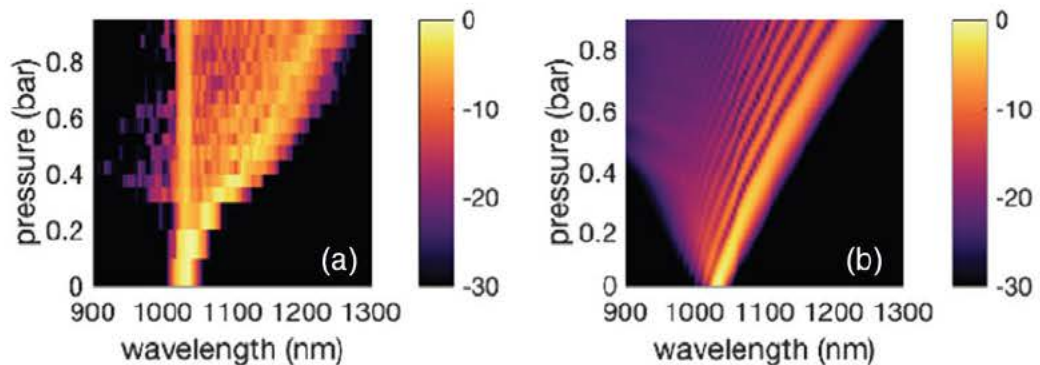
Figure 3.2.3: (a) Measured and (b) calculated spectra, broadened and red-shifted by SRS in a nitrogen filled HCF as a function of nitrogen pressure. The key parameters for SRS (fiber diameter and length, laser pulse intensity and duration) and output spectra are comparable to the ones used in the experiment described in chapter 6. Figure adapted from [99].
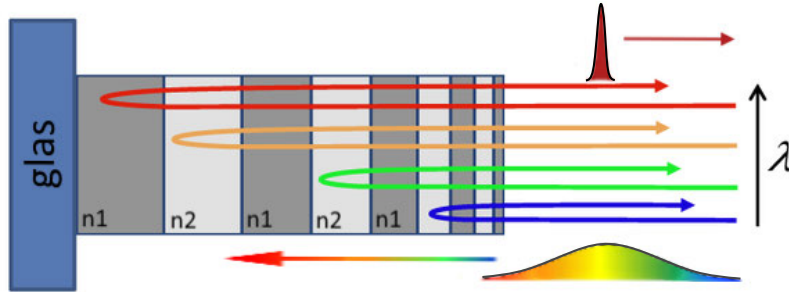
Figure 3.2.4: Simplified schematic of a chirped mirrors for negative dispersion: In the stacked layers of dielectric coatings with increasing thickness longer wavelengths components of the laser beam penetrate deeper into the mirror before being reflected, thus, experiencing higher group delay than the shorter wavelength components. Such a configuration can be employed to counteract the temporal chirp of a laser pulse and compress it in time to its transform limited duration.

The amount of spectral broadening and red-shift is proportional to gas pressure and laser power [99, 100] and can be continuously tuned by adjusting the gas pressure until it is limited by the critical power of self focusing. An example of achievable spectra produced by SRS in a HCF with similar parameters as for chapter 6 is given in Fig. 3.2.3

3.2.3   Pulse compression with chirped mirrors

After spectral broadening by either SPM or SRS, due to dispersion in the gas, laser pulses are stretched in time and positively chirped, meaning that the leading edge of the laser pulse will contain the long wavelength (red) components, while the trailing edge contains the short wavelengths (blue) components of its spectrum. To again achieve transform limited pulses, the different spectral components have to be stacked onto each other in the temporal domain, which can be achieved by so-called chirped mirrors [101].

See Fig. 3.2.4 for a schematic representation of such a chirped mirror. It can be understood as a special case of a dielectric Bragg mirror, stacked layers with thickness d of two materials with different refractive indices n_1 and n_2. At each material interface incident light is partially reflected and for a certain wavelength λ with $n_{1,2} \cdot d = \lambda/4$ and normal incidence these

reflections interfere constructively. Very high reflectivities of such a mirror can be achieved by a high number of layers and high contrast in refractive indices. By this principle, such layer stacks can also be designed for different incidence angles or as anti reflection coatings.

Now for chirped mirrors, this principle is extended such that the thickness of the layers are not constant anymore, but is varied throughout the structure to compensate the chirp of laser pulses. For the case of positive chirp, the thickness d increases continuously from the top layer farther into the material and so longer wavelengths will penetrate deeper into the mirror before being reflected. In other words, the leading long wavelength edge of a positively chirped laser pulses will have a longer path length and each reflection of such a mirror will result in temporal pulse compression. Typically, to fully compensate the dispersion acquired from SPM or SRS multiple reflections (4-10) from chirped mirrors are required.

In practice, such a simplified mirror design would show oscillations of its group delay dispersion, which can be circumvented by a so-called double chirped mirror design, where in addition to the layer thickness d also the thickness-ratio of the two materials is chirped. Another complication are reflections at the first interface to air, which can be counteracted by a carefully tuned anti reflection structure on top of the actually chirped mirror.

3.3 Pulse characterization

For all the performed experiments at least an assessment and confirmation of the quality of laser pulses is necessary. For ultrashort laser pulses in the femtosecond regime there exist several techniques for pulse characterization and for the experiments presented here this was done by second harmonic generation frequency resolved optical gating (SHG FROG)[102], which will be described in section 3.3.1. A crucial part of the electron transfer experiments of chapters 4 and 5 is the measurement of the carrier-envelope phase (CEP), which is inaccessible to SHG FROG and instead measured by a stereo ATI phasemeter, described in section 3.3.2.
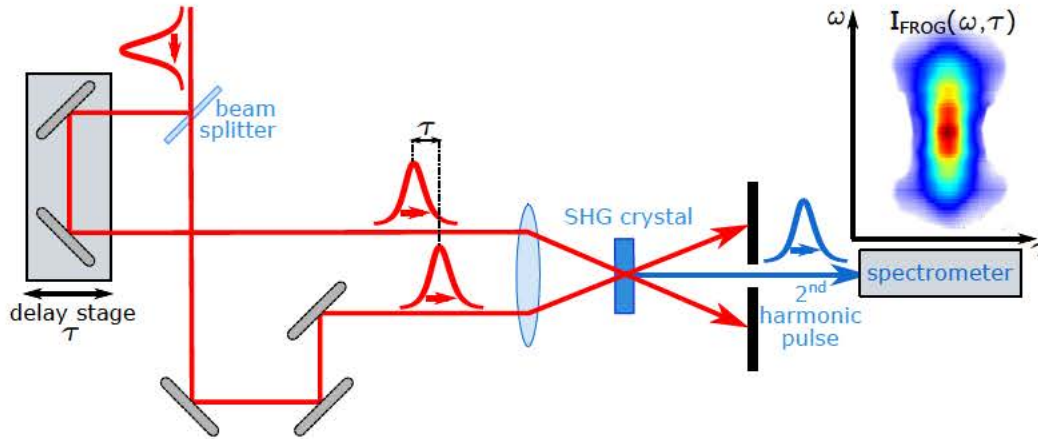
Figure 3.3.1: Schematic of a setup for pulse characterization by SHG FROG. The incoming laser pulse is split in two, with one pulse being delayed by τ with respect to the other. The two pulses are focused into a crystal with a $\chi^{(2)}$-nonlinearity (SHG crystal) and the spectrum of the resulting second harmonic pulse is recorded by a spectrometer. The dataset of spectra for varying delay times τ is the so-called FROG-trace that can be used to reconstruct the shape of the incoming pulse.

3.3.1 Frequency resolved optical gating

Pulse parameters such as pulse energy, repetition rate and spectral shape can be quite easily measured with power meter, photo diode and a spectrometer. However, for characterization of ultrashort laser pulses, in addition to the aforementioned, at least the spectral phase is required. A method to measure the phase, is frequency resolved optical gating [102], existing in several variants, of which SHG FROG based on second harmonic generation in a crystal with strong second order susceptibility $\chi^{(2)}$ (SHG crystal) was used during this work. With knowledge of the pulse in the spectral domain $E(\omega) = \tilde{E}(\omega)e^{i\varphi(\omega)}$, the electric field shape in the temporal domain can be calculated via Fourier re-transformation:

$$E(t) = \hat{E}(t)e^{i\phi(t)} = \frac{1}{2\pi}\int_{-\infty}^{\infty} E(\omega)e^{i\omega t} \tag{3.3.1}$$

A schematic of a SHG FROG setup is shown in Fig. 3.3.1. Similar to intensity auto-correlation, the laser pulse itself is used as a temporal gate. For SHG

FROG, this is done by dividing the laser beam into two different pathways by a beam splitter, controlling the time delay τ between the two arms and then focusing them into a SHG crystal. The resulting second harmonic laser pulse and its spectrum depend on the temporal overlap of the two pulse replicas and multiple spectra are recorded while scanning the gate pulse over its twin by varying the time delay τ. The collection of these spectra gives a two dimensional dataset, a so-called FROG-trace $I_{FROG}(\omega, \tau)$. From this FROG-trace the spectral phase of the initial laser pulse can be reconstructed by an iterative phase retrieval algorithm, that also includes a consistency check due to the involved redundancy.

There are some practical limitations to SHG FROG [103]. The response of the spectrometer needs to be calibrated and for extremely broadband laser pulses there may not be a single spectrometer that can cover the whole bandwidth. Sub-cycle pulses with an over octave spanning spectrum cannot be easily characterized by a technique based on second harmonic generation as the blue wing of the fundamental pulse and red wing of its second harmonic will overlap. Also for few-cycle laser pulses ($<10\,\text{fs}$) the dispersion of the beam splitter can be a significant factor influencing the measurement. For non-collinear configurations, the accuracy is limited by a geometric smearing effect, but still an upper limit for the pulse duration can be acquired [104]. Fundamentally, direction of time and CEP cannot be measured by SHG FROG.

3.3.2 Carrier envelope phase tagging (Stereo ATI phasemeter)

A missing parameter for a complete characterization of the electric field of a laser pulse is the CEP, a time independent offset to the phase: $E(t) = \hat{E}(t)exp(i\phi(t) + \phi_{CEP})$. It can be understood as the phase difference between the fast oscillations of the electric field at optical frequencies, the carrier, and envelope of the laser pulse. Especially for few- and sub-cycle laser pulses the actual electric field shape will depend strongly on this CEP (see Fig. 3.3.2). Typically the CEP fluctuates randomly between laser shots and additional
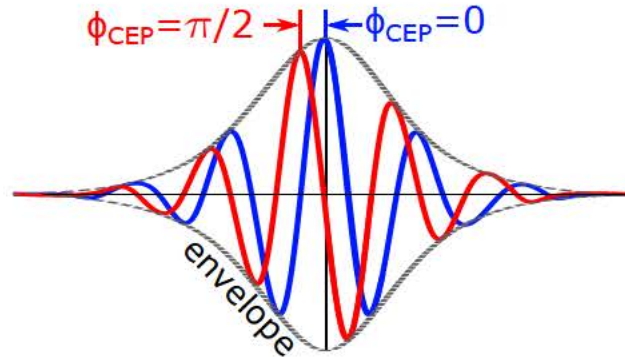
Figure 3.3.2: Laser electric field for a laser pulse with a $\phi_{CEP} = 0$ in blue (cosine-like) and $\phi_{CEP} = \pi/2$ in red (sine-like) for a given pulse envelope. As was discussed in chapter 2, the electron ionization rate depends exponentially on the electric field strength and therefore the CEP of an ultrashort laser pulse is decisive for the timing of electron ionization and recollision that is initiated by it.

measures need to be taken to control or stabilize it.

For the electron transfer process explored in chapters 4 and 5 the shape of the laser electric field, therefore the CEP, plays a crucial role. As we are interested in a scan over all possible CEP values, the CEP is here not stabilized, but instead measured for every laser shot and the result added to the acquired dataset (CEP-tagging).

The CEP measurement is done by a stereo ATI phasemeter [25, 26]. A schematic of its operation principle is shown in Fig. 3.3.3 and will be explained here. A part of the laser beam is sent to the stereo ATI phasemeter and focused onto a xenon gas-target in a vacuum chamber. For a reliable single shot characterization of each incoming laser pulse, a peak intensity on the order of $1 \times 10^{14} W/cm^2$ is required [105]. The polarization vector of the laser pulse is orthogonal onto the detection planes of two micro channel plates (MCP) detectors, that are positioned equidistant from the laser focus, for measuring the kinetic energies of produced electrons.

The laser pulses ionize the xenon gas and rescattering ATI electrons can reach kinetic energies of up to 50 eV with an energy spectrum that depends strongly on the laser electric field shape (see sections 2.1 and 2.3). The
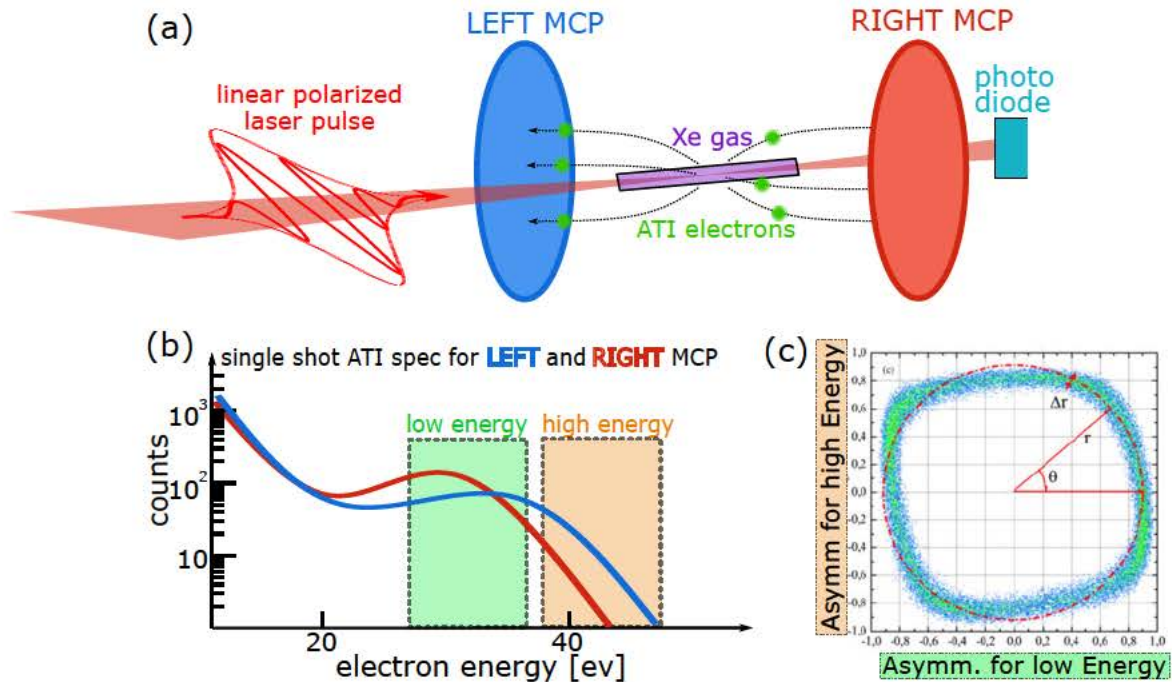
Figure 3.3.3: (a) Schematic of Stereo ATI-phasemeter: The laser pulse is focused into xenon gas and causes ATI. A photodiode is used to trigger the time of flight measurement. The left and right sided photoelectron energy spectra of produced rescattering ATI electrons are measured by the time of flight to the left and right MCP. (b) Example of a single shot ATI spectra for left (blue) and right (red) MCP. The differences in these ATI spectra, in the region between $2U_p$ and $10U_p$, are characteristic for a given CEP and can be quantified by asymmetry parameters for the indicated low (green) and high energy (orange) integration regions. In a plot of asymmetry parameter for low versus high energy region the polar angle θ corresponds to the CEP and the radial distance r is inversely proportional to the pulse duration. (c) Asymmetry plot for about 150000 single shot measurements of sub 4 fs pulses adapted from [105].

spectra that are recorded for a given field shape, a specific CEP, by the individual detectors show pronounced differences and by integration in a low and high energy region two asymmetry parameters can be defined:

$$A_{low} = \frac{N_{low}^{LEFT} - N_{low}^{RIGHT}}{N_{low}^{LEFT} + N_{low}^{RIGHT}}$$
$$A_{high} = \frac{N_{high}^{LEFT} - N_{high}^{RIGHT}}{N_{high}^{LEFT} + N_{high}^{RIGHT}} \tag{3.3.2}$$

In a two dimensional plot of these two parameters for adequately chosen low/high energy regions the measured laser shots are represented by dots that form a ring structure, a so-called 'phase potato' (e.g. Fig. 3.3.3(c)). The polar angle $\theta = arctan(A_{high}/A_{low})$ in such a representation is equivalent to the relative CEPs between measured laser pulses and it is possible to obtain absolute CEP values, that means a specific field shape, by calibration [106]. Shorter pulses result in larger asymmetry values and therefore the radial distance $r = \sqrt{A_{low}^2 + A_{high}^2}$ is inversely proportional to the pulse duration [107]. This also means it is only possible to reliably measure the CEP of sufficiently short (<10 fs) laser pulses, as for longer pulses the asymmetry will be too small and no phase potato will be detected, because its radius becomes negligible.

3.4 Target preparation

To facilitate the experiments of chapters 4 and 5, the target, a gas jet of argon atoms, containing a fraction of argon dimers, has to be carefully prepared as part of the COLTRIMS measurements. Ideally, the gas jet is well localized, internally cold (i.e. it has a low lateral momentum) and contains a large fraction of argon dimers.

To achieve this, the pressurized gas (few bar) is expanded through a small nozzle ($10 \, \mu m$) into a vacuum chamber, so-called supersonic-expansion [108, 109]. During this expansion, thermal energy of the gas is converted into directed kinetic energy of the gas jet. In the center of such a supersonic gas
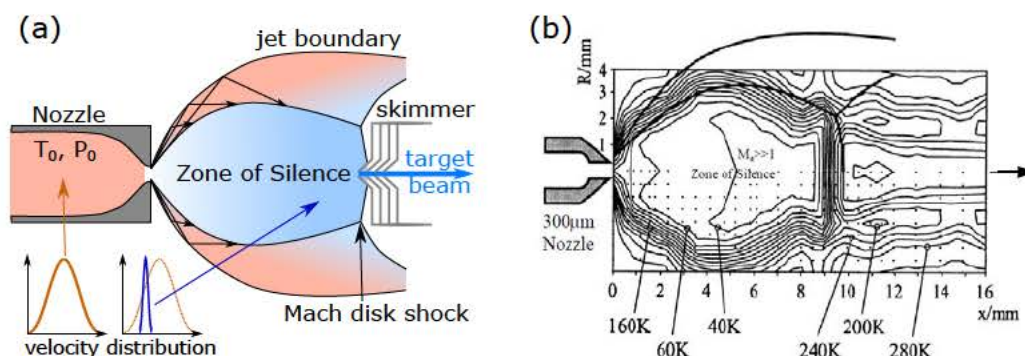
Figure 3.4.1: (a) Schematic of a supersonic jet from gas expansion through a thin nozzle between a high pressure reservoir and a low pressure volume. The so-called zone of silence where temperatures can be as low as a few Kelvin is surrounded by a system of shock waves. By placing a skimmer in the zone of silence, a well localized, internally cold target beam can be extracted. (b) Measurement of temperature in a supersonic jet of CO_2 adapted from [108].

jet is a region with a directed flow of low density gas and temperatures that can be as low as a few Kelvin, the so-called zone of silence, which is confined by a system of shock waves (see Fig. 3.4.1). The properties of the gas jet depend mostly on the gas pressure and temperature before expansion. Because information of boundary conditions cannot propagate faster than the speed of sound in the medium, a supersonic flow is not affected by any downstream objects. Therefore, a skimmer ($300\,\mu m$) can be placed into the zone of silence without influencing its properties. By this, a well localized, internally cold, supersonic gas jet with almost negligible momentum perpendicular to its propagation direction is produced.

Due to the low temperatures achieved in the supersonic gas jet, weakly bound vdW dimers can be formed by collision and reach the laser interaction region without dissociating again. However, typically the fraction of dimers in the gas jet is on the order of $0.1\,\%$ to $1\,\%$ and any increase is desired as it directly increases the rate of data acquisition. The dimer fraction depends on several factors: gas species; nozzle size and shape; gas temperature and pressure; nozzle-skimmer distance. See for instance [110, 111] for details. For the performed experiments, some factors were fixed, but gas temperature,

backing pressure and nozzle-skimmer distance could be scanned to optimize the dimer fraction to a few percent.

3.5 Coincidence momentum imaging

Insight into electron dynamics for the investigation of electron transfer processes upon strong field interaction (chapters 4 and 5) can be gained via measurement of electron momenta. Due to momentum conservation, this should be equivalent to measuring the ion's recoil momentum acquired by the ionization process. This fact is exploited in the so-called recoil ion momentum spectroscopy (RIMS)[112]. However, in practice the resolution of this was limited by the width of the momentum distribution of the investigated target, or in other words its temperature. Therefore the accuracy was drastically improved by the utilization of a cold target beam produced by supersonic expansion (see section 3.4), thus enhancement of RIMS to cold target recoil ion momentum spectroscopy (COLTRIMS)[113, 114]. Several more improvements were applied to this basic COLTRIMS concept and nowadays it is possible to acquire the 3-dimensional momentum vectors of almost all charged particles produced by an atomic or molecular reaction in coincidence, often referred to as reaction microscopy (REMI).

A schematic overview of the COLTRIMS apparatus used is given in Fig. 3.5.1 and more details about this specific setup can be found in [109]. To reduce the number of background events as much as possible, the measurements are performed in an ultrahigh vacuum chamber that can reach background pressure of 10^{-10} mbar. In the interaction region of this spectrometer chamber, the incoming CEP-tagged ultrashort laser pulses, propagating along the y-direction, intersect with the cold target beam in x-direction. As discussed in chapter 2, the light-matter interaction can induce a plethora of reactions that also involve ionization. Afterwards produced electrons and ions are guided in opposite z-direction (TOF-direction) by carefully tuned, homogeneous electric and magnetic fields to two position sensitive detectors that each consist of a combination of MCP and delay line anode. As long as the separation
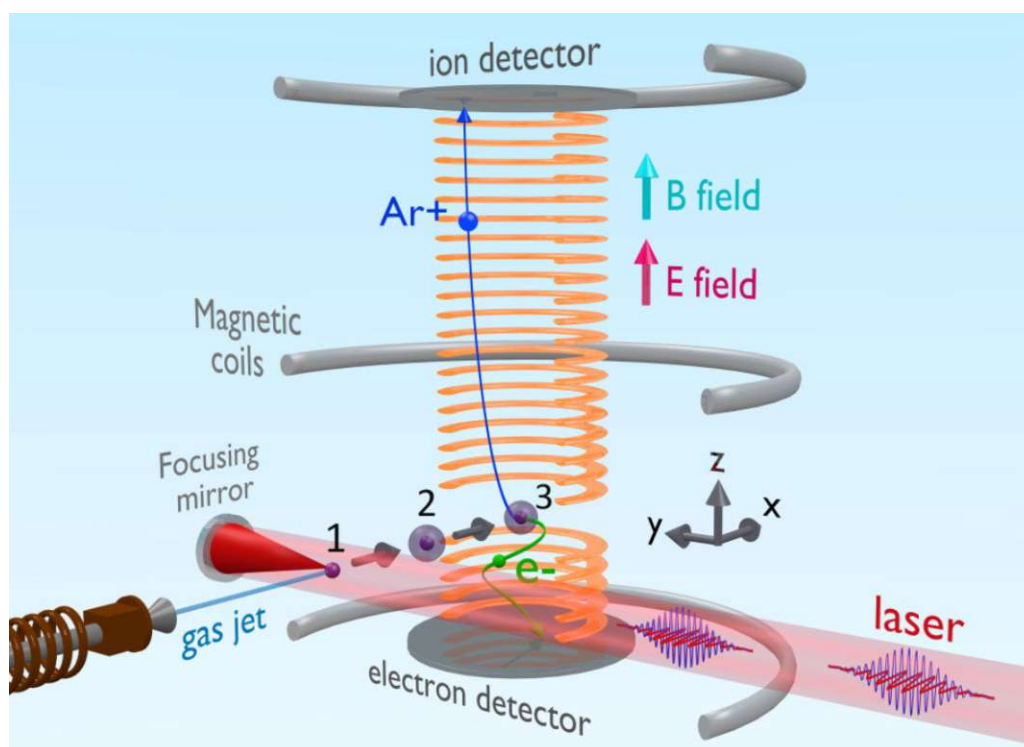
Figure 3.5.1: Schematic of the COLTRIMS apparatus. The supersonic target gas jet and laser beam intersect in the center of a ultrahigh vacuum chamber ($\approx 10^{-10}$ mbar). Ions and electrons produced by the light-matter interaction are guided by electric and magnetic fields to MCP detectors on opposite sites of the vacuum chamber. By recording the position on the detectors (x, y) and time-of-flight (TOF), the 3-dimensional momentum vector (p_x, p_y, p_z) of each detected fragment can be reconstructed. Figure adapted from [47].

in time of incoming particles is longer than a few tens of ns, this detection scheme is able to measure the impact position (x,y) and TOF of multiple particles for each laser shot. To ensure that the detected particles originate from the same interaction event, the coincidence condition of less than one reaction event per laser pulse has to be fulfilled. This is done by reduction of background events and choosing the density of the gas target, interaction volume and laser intensity appropriately.

With the knowledge of the detector geometry and applied fields, it is possible to calculate from the acquired dataset of two dimensional impact position (x,y) and TOF the initial 3-dimensional momentum vector (p_x, p_y, p_z) of detected particles. Under coincidence conditions, all the produced particles by each laser shot can be traced to the same event and in combination with knowledge of the laser pulse shape (CEP-tagging) the interaction event can be completely reconstructed in the offline data analysis. Even if not all particles are detected, it is possible to reconstruct missing information by the application of momentum conservation.

Typically, datasets of a large number of events are acquired over multiple measurement days (up to 10^8 events per day), then further calibrated and filtered during the offline analysis to identify different types of events or reaction pathways. For instance in a photo-ion-photo-ion-coincidence map (PIPICO), where the TOFs of coincident particles are plotted, dissociation events show up as curved lines depending on the mass to charge ratios of involved fragments. These can be picked from the dataset for further analysis by application of filter conditions.

3.6 Simulations: Classical ensemble model

To explain the observations in argon dimers presented in chapters 4 and 5, the collaborating group of Xiaojun Liu, from the Innovation Academy for Precision Measurement Science and Technology (APM) in Wuhan, China, provided simulations. Details of the used simulation model are given here and my interpretations of the produced data are discussed in detail in chapters 4 and 5. In these simulations the motion of the correlated electrons and the nuclei in the combined laser and Coulomb fields were traced by performing a 3D classical ensemble model calculation [115, 116]. Due to the very complex many-body dynamics involved in the ionization-dissociation of a dimer, time-dependent Schrödinger equation (TDSE) simulations are not feasible as they are beyond the present computational capability. Even though classical trajectory models neglect all quantum effects such as pathway interferences, it is known that they are reliable in reproducing experimental observables on a qualitative level. For example, classical trajectory models were used to successfully explain photoelectron distributions from two-color fields [117, 118], the sub-cycle ionization dynamics in circularly polarized fields [119, 120], and even the complicated process of electron-electron correlation involved in recollision-induced double ionization in linearly polarized fields [121] and two-dimensional two-color waveforms [122, 123]. In problems directly related to the present work classical trajectory models could well reproduce the angular distributions of fragment ions emitted during strong-field ionization-fragmentation of the argon dimer [116], and they could explain the sensitivity of electron recapture processes via the FFI mechanism to the laser field's waveform [47]. However, due to the neglect of quantum effects, certain quantities calculated with classical models, such as ionization or scattering cross sections, may differ from those obtained with quantum models. Nevertheless, classical trajectory models are valuable tools to unveil the underlying mechanisms leading to experimental observables in complex multi-electron, multi-dimensional problems such as the present one.

As in the presented experiments, the laser intensity is well above the over-the-barrier threshold [27, 124], the outermost electron is rapidly stripped from

each atom of the argon dimer at the rising edge of the laser field and leaves the interaction region quickly. It is therefore reasonable to assume that the motion of the remaining electrons and ions is not affected by the first two emitted electrons [115]. Thus, the model ignores the influence of the first electron in each argon atom and the starting configuration of the dimer for the simulation is $Ar_2^{2+} = (Ar^{2+} + e^-) + (Ar^{2+} + e^-)$, i.e., two doubly charged argon ion potentials separated by R_{eq} with an active electron bound to each of them. This approach has previously been used successfully to model the strong field fragmentation dynamics of argon dimers and trimers [115, 116]. The error in the CEP-dependence of the electron emission asymmetry that might result from the neglect of the first two ionization steps is expected to be small, since the two electrons are emitted early in the pulse when the laser vector potential is still small.

To mimic the situation of the experiment, the orientation of the dimer with respect to the laser polarization was randomized, and the initial condition of each active electron is sampled from a microcanonical distribution around its corresponding parent nucleus with a binding energy equal to the double ionization potential of the argon dimer. The influence of the dimer orientation on the $\mathcal{A}_z^{(n,m)}$ curves is discussed in more detail Section 4.5.3.

The initial momentum of each of these two nuclei was assumed to be zero and the distance between them was set to 7.12 a.u, equilibrium internuclear distance (R_{eq}) of the argon dimer [125]. The subsequent evolution of the two electrons and nuclei driven by the intense laser field is governed by the following coupled many-body Newton's equations of motion,

$$
\begin{aligned}
\frac{d^2\boldsymbol{r_i}}{dt^2} &= -\vec{E}(t) - \nabla_{r_i}\left(-\sum_{k=1}^{2}\frac{2}{|\boldsymbol{R_k}-\boldsymbol{r_i}|} + \sum_{j=1,j\neq i}^{2}\frac{1}{|\boldsymbol{r_i}-\boldsymbol{r_j}|}\right), \\
\frac{d^2\boldsymbol{R_k}}{dt^2} &= \frac{2}{M}\vec{E}(t) - \frac{1}{M}\nabla_{R_k}\left(-\sum_{i=1}^{2}\frac{2}{|\boldsymbol{R_k}-\boldsymbol{r_i}|} + \sum_{l=1,l\neq k}^{2}\frac{4}{|\boldsymbol{R_k}-\boldsymbol{R_l}|}\right),
\end{aligned}
\tag{3.6.1}
$$

where $i,j = 1,2$ and $k,l = 1,2$ denote the two electrons and two nuclei, respectively. M represents the mass of the argon nucleus. $\boldsymbol{r}$ and $\boldsymbol{R}$ denote

the displacements of the electrons and nuclei.

The laser electric field in the simulation was represented as follows

$$\vec{E}(t) = -E_0 \exp\left(-4\ln(2)(t/(2T))^2\right)\cos(\omega t - \varphi_{\mathrm{CEP}})\hat{\vec{z}} \qquad (3.6.2)$$

where E_0 is the peak laser field, ω the laser angular frequency, φ_{CEP} the CEP, $T = 2\pi/\omega$ and $\hat{\vec{z}}$ is the unit vector along the laser polarization direction z.

This system is allowed to evolve freely for 500 laser-cycles after the laser field is turned off to ensure that the two nuclei are completely separated. Then the resulting fragmentation channel Ar(n,m), where Ar(n, m) denotes Ar$_2 \xrightarrow{\text{Laser}} \mathrm{Ar}_2^{(n+m)+} \to \mathrm{Ar}^{n+} + \mathrm{Ar}^{m+}$, are identified. For comparison with the experiments, the three fragmentation channels of interest are Ar(1,2), Ar(2,2) and Ar(1*,2). The Ar(1,2) and Ar(2,2) channels are ascertained by an energy criterion: The Ar(1,2) channel is reached when the final energy of only one electron is larger than zero, whereas the Ar(2,2) channel is reached when both electrons have final energies larger than zero. The criterion to qualify as Ar(1*,2) is as follows, one electron must have an energy larger than zero and additionally the kinetic energy released (KER) of the fragmentation has to be between 12 eV and 18 eV, which is the experimentally determined KER range of the Ar(1*,2) channel, see Fig. 5.2.1(a).

For a comparison of simulated and measured curves, all measured data in chapters 4 and 5 was shifted by the same constant CEP-value such that the simulated and measured curves for the Ar$^+$ monomer overlap. With that, the experimental and simulated curves agree well also for the Ar(1,2), Ar(2,2) and Ar(1*,2) channels. In particular the simulated CEP shifts between these channels are very close to the measured values and will be discussed in more detail in chapters 4 and 5.

3.6.1 Asymmetry parameter $\mathcal{A}$ vs. mean sum momentum

In chapters 4 and 5, in order to obtain insight into the laser-driven electron dynamics, the CEP-dependence of the asymmetry of the electron (or equivalently the ion) momentum distributions along the laser polarization direction is analyzed. To this end for each fragmentation channel, $\mathrm{Ar}(n,m)$, an asymmetry parameter along z is defined,

$$\mathcal{A}_z^{(n,m)} = \frac{n_{\mathrm{up}} - n_{\mathrm{down}}}{n_{\mathrm{up}} + n_{\mathrm{down}}}, \qquad (3.6.3)$$

where n_{up} and n_{down} denote the number of electrons with sum momentum in z-direction $\bar{p}_{e,z}^{(n,m)} > 0$ and $\bar{p}_{e,z}^{(n,m)} < 0$, respectively. The use of $\mathcal{A}_z^{(n,m)}$ has the practical advantage that it can be directly associated with the integral over the ionization time distributions in Figs. 4.3.1 and 5.4.1, and therefore is a convenient quantity for the visual, qualitative comparison of the time distributions with the CEP-dependence of the electron emission.

However, the quantities n_{up} and n_{down} do not contain information on the momenta of the emitted electrons, but only characterize their yields. Thus, $\mathcal{A}_z^{(n,m)}$ does not contain information on whether the electrons are emitted with high or low momentum, and also not on how many electrons are emitted with what momentum; $\mathcal{A}_z^{(n,m)}$ is blind to the shape of the electron momentum distributions. A quantity that does also contain information on the momenta of the electrons and therewith on the shape of the momentum distributions is the mean sum momentum, which for a given fragmentation channel of the argon dimer, $\mathrm{Ar}(n,m)$, along the laser polarization direction z is defined as

$$\bar{\bar{p}}_{e,z}^{(n,m)} = \frac{\int \bar{p}_{e,z}^{(n,m)} N(\bar{p}_{e,z}^{(n,m)}) d\bar{p}_{e,z}^{(n,m)}}{\int N(\bar{p}_{e,z}^{(n,m)}) d\bar{p}_{e,z}^{(n,m)}}, \qquad (3.6.4)$$

where $N(\bar{p}_{e,z}^{(n,m)})$ denotes the number density of electrons with momentum $\bar{p}_{e,z}^{(n,m)}$. Due to momentum conservation, from $\bar{\bar{p}}_{e,z}^{(n,m)}$ the center of mass recoil momentum of the ions, $\bar{\bar{p}}_{R,z}^{(n,m)}$, can be calculated as $\bar{\bar{p}}_{R,z}^{(n,m)} = -\bar{\bar{p}}_{e,z}^{(n,m)}$.
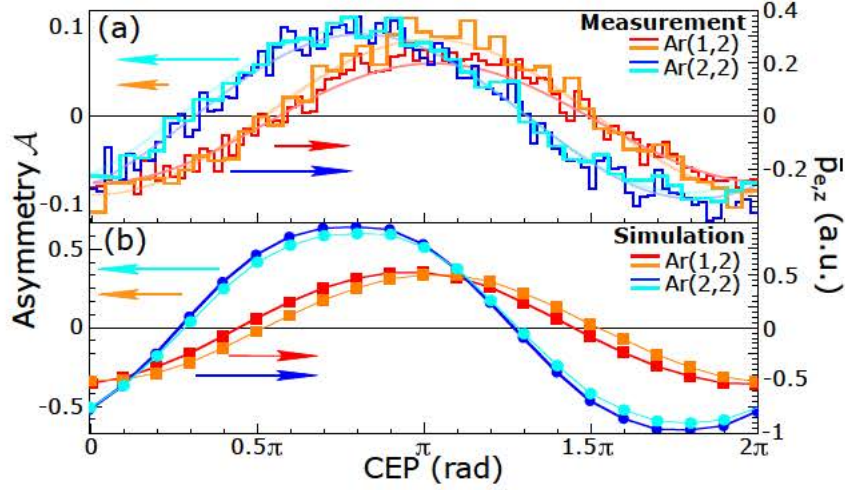
Figure 3.6.1: Comparison of the CEP-dependence of the measured (a) and simulated (b) asymmetry parameter $\mathcal{A}_z^{(n,m)}$ along z (left axis, light colors) with the mean electron sum momentum $\bar{\vec{p}}_{e,z}^{(n,m)}$ along z (right axis, dark colors) for the fragmentation channels for the Ar$(1,2)$ and Ar$(2,2)$ channels, i.e., for $(n,m) = \{(1,2),(2,2)\}$.

Fig. 3.6.1 compares the measured and simulated CEP-dependences of $\mathcal{A}_z^{(n,m)}$ with that of $\bar{\vec{p}}_{e,z}^{(n,m)}$ for the two fragmentation channels Ar$(1,2)$ and Ar$(2,2)$. It can be seen that the measured curves of both quantities show an almost identical CEP-dependence. Also the simulated curves feature a very similar CEP-dependence, albeit in this case the $\mathcal{A}_z^{(n,m)}$ curve shows a slightly larger left shift (by $< 0.1\pi$) than the $\bar{\vec{p}}_{e,z}^{(n,m)}$ curve. This slight deviation between the two quantities is still significantly smaller than the CEP-shift between the Ar$(1,2)$ and Ar$(2,2)$ channels that is further analyzed in chapters 4 and 5. Thus, both quantities, $\mathcal{A}_z^{(n,m)}$ and $\bar{\vec{p}}_{e,z}^{(n,m)}$, can be used to quantitatively analyze the left CEP-shift between these two channels. This left-shift is due to the LITE process, as will be explained in detail in chapter 4. Thus, it can be concluded that the results and analysis are to a good approximation independent of whether $\mathcal{A}_z^{(n,m)}$ or $\bar{\vec{p}}_{e,z}^{(n,m)}$ are considered. In the discussion in chapters 4 and 5 the asymmetry parameter $\mathcal{A}_z^{(n,m)}$ was chosen simply because of its direct connection to the time-distributions in Fig. 4.3.1 and 5.4.1.

The reason for the near-equivalence of $\mathcal{A}_z^{(n,m)}$ and $\bar{\vec{p}}_{e,z}^{(n,m)}$ is that the electron (or ion) sum momentum distributions along z of both the Ar$(1,2)$ and

Measurement
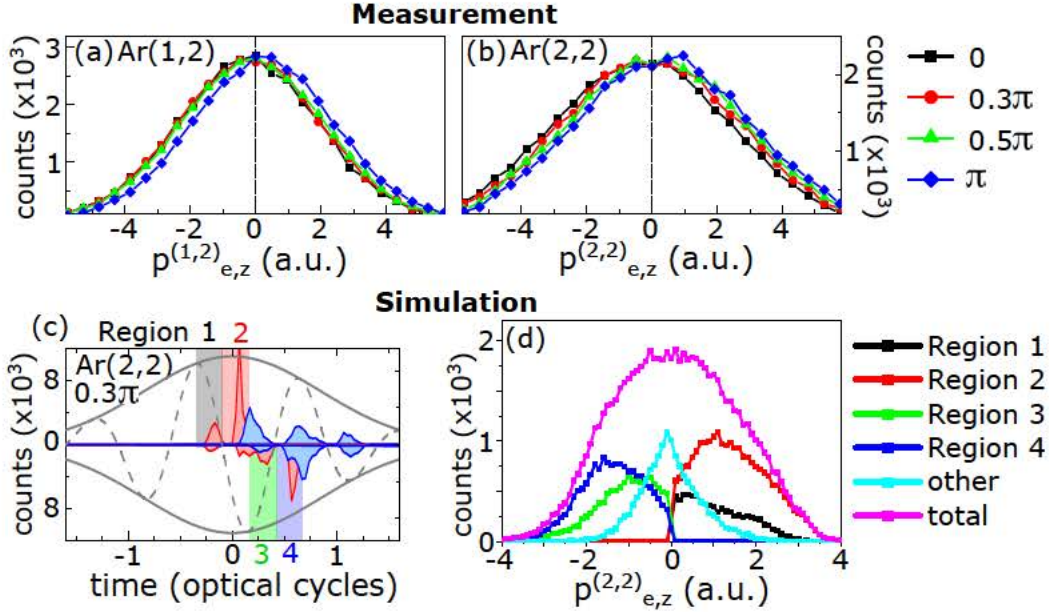
Simulation

Figure 3.6.2: (a,b) Measured sum electron momentum distributions for the Ar(1, 2) (a) and Ar(2, 2) (b) channels for four values of the CEP. (c) Ionization time-distributions simulated using the 3D classical ensemble model of the first (red distributions) and second emitted electrons (blue distributions) for the Ar(2, 2) channel and a CEP of 0.3π. (d) Simulated electron sum momentum distributions for the Ar(2, 2) channel corresponding to the ionization time-distributions of the first electron in (c). Shown are the total distribution (magenta) and the color-coded contributions to it resulting from the ionization time windows for the first electron denoted Region 1 to 4 in (c).

Ar(2, 2) channels exhibit a single-peaked gaussian-like shape and that mainly their peaks oscillate as a function of CEP. This is depicted in Figs. 3.6.2(a) and 3.6.2(b) for the sum electron momentum distributions, which move from negative to positive values as the CEP increases from 0 to π. This is consistent with the CEP-dependence of $\bar{p}_{e,z}^{(n,m)}$ and $\mathcal{A}_z^{(n,m)}$ shown in Fig. 3.6.1.

It might be somewhat surprising that the momentum distributions exhibit a single-peaked gaussian-like shape, given the complicated laser-sub-cycle emission dynamics that is revealed by the analysis in chapters 4 and 5. To understand this fact, in Fig. 3.6.2(c) the electron emission time-distributions predicted by the 3D classical ensemble model simulations for the Ar(2, 2)

channel and a CEP-value of 0.3π is shown. A statistics of the momentum distributions resulting from emissions of the first electron during four quarter cycles, marked as 1 to 4 in Fig. 3.6.2(c), is shown in Fig. 3.6.2(d). It can be seen that the momentum distributions corresponding to the electrons emitted during these four quarter cycles each exhibit a single-peak structure with either purely positive or negative momentum. However, their sum (together with the trajectories emitted during the rest of the pulse not covered by the regions 1-4) exhibits a smooth gaussian-like shape around zero momentum very much consistent with the measured momentum distributions in Figs. 3.6.2(a) and 3.6.2(b). As a result, the complicated laser-sub-cycle emission dynamics can be well characterized by either $\mathcal{A}_z^{(n,m)}$ or $\bar{\vec{p}}_{e,z}^{(n,m)}$.

*"My words may not be sweet and my looks may not
be fair, but I have love enough to give and a life
enough to share." And she replys: "Same"*
— *The vows of Walnut and Brahma, the 'C'-Team*

Chapter 4

Laser-induced electron-transfer in the dissociative multiple ionization of argon dimers

This chapter reports on an experimental and theoretical study of the ionization-fragmentation dynamics of argon dimers in intense few-cycle laser pulses with a tagged carrier-envelope phase (CEP). It is found that a field-driven electron transfer process from one argon atom across the system boundary to the other argon atom triggers sub-cycle electron-electron interaction dynamics in the neighboring atom. This attosecond electron-transfer process between distant entities and its implications manifest themselves as a distinct phase-shift between the measured asymmetry of electron emission curves of the $Ar^+ + Ar^{2+}$ and $Ar^{2+} + Ar^{2+}$ fragmentation channels. This work discloses a strong-field route to controlling the dynamics in molecular compounds through the excitation of electronic dynamics on a distant molecule by driving inter-molecular electron-transfer processes.

4.1   Motivation

Photoinduced molecular charge-transfer across system boundaries is a key step in many important natural or technical processes such as solar-driven energy production [126, 127], photocatalysis [128, 129], or photosynthetic activity [130, 131]. In these processes the relocation of charge, initiated by the absorption of a single photon by a molecule, is determined by the energetic and spatial structure of the system. A fundamentally different mechanism for determining charge-localization processes becomes available in strong laser fields. It was shown that the *intra-molecular* localization of electrons during the dissociation of isolated, small molecules can be determined by multi-photon processes driven by intense few-cycle laser pulses using their CEP as the control parameter [132–136].

An intriguing yet unexplored question is then, whether strong-field-driven multi-photon processes can influence the localization of charge not only within one molecule but also *across* system boundaries. Widely used model-systems for investigating inter-system transfer reactions are small vdW clusters and dimers. VdW dimers are used to study photoinduced biological processes [58, 137, 138], photocatalytic reactions [61, 139], and energy or charge transfer reactions induced by soft X-ray photons [140–143] and electron impact [144]. VdW systems are also studied with strong laser fields, but in the case of dimers with a focus on the field-driven ionization and fragmentation dynamics [49, 116, 145–156], or electronic energy conversion processes in the case of larger clusters [157–162]. To the best of my knowledge, strong-field driven electron transfer-reactions across the system boundary from one entity to another have thus far not been investigated.

In this chapter, it will be shown experimentally and by simulations, using the argon dimer, Ar_2, as an example, that electron transfer-reactions from one argon atom to the other can be driven by a strong laser field and, furthermore, that they are decisive for the ionization and fragmentation behavior of the dimer. Specifically, it will be demonstrated that an electron liberated at one of the two argon atoms can be captured by the neighboring atom. This

process, which will be referred to as the laser-induced transfer of electron (LITE) process, determines the emission timing of the electrons via electron-electron interaction and thus, depending on the CEP, influences the momenta of the emitted electrons. As a result, the effect of LITE can be observed in the presented experiments and simulations when comparing the asymmetry of electron emission as a function of CEP for the two ionization- fragmentation channels Ar(1,2) and Ar(2,2), where Ar(n,m) denotes Ar$_2 \xrightarrow{\text{Laser}}$ Ar$_2^{(n+m)+} \rightarrow$ Ar^{n+} + Ar^{m+}.

4.2 Experiment

In the experiments, argon dimers created by supersonic expansion of a few bars of argon gas were ionized by intense laser pulses, linearly polarized along z, with a full width at half maximum (FWHM) duration in intensity of 4.5 fs and a peak intensity, calibrated in *in situ* [163], of $5 \times 10^{14} W/cm^2$, inside the ultra-high vacuum chamber of a COLTRIMS reaction microscope [113]. Details on the COLTRIMS apparatus can be found in section 3.5 and Refs. [42, 118, 164]. The laser center wavelength was $\lambda = 750$ nm. The duration of the pulses and their CEP were measured with a stereo ATI phasemeter in phase-tagging mode, see section 3.3.2 and [105] for details. Upon laser ionization of the argon dimers, the two vdW-bound argon atoms, separated by their $R_{eq} \approx 7.1$ a.u., undergo fragmentation via Coulomb explosion. The two emerging argon ions, Ar^{n+} and Ar^{m+}, were detected in coincidence and from their time of flight and impact position on the detector their three-dimensional momenta $\mathbf{p}_{\text{Ar}}^n$ and $\mathbf{p}_{\text{Ar}}^m$ were calculated. By imposing momentum conservation conditions onto the ions detected in coincidence, the two-body fragmentation channels of interest, Ar(1,2) and Ar(2,2), as well as the channel Ar(1,1), were selected for further analysis. Due to momentum conservation, the sum momentum of the $(n + m)$ emitted electrons, $\mathbf{p}_e^{(n,m)} = \sum_{i=1}^{n+m} \mathbf{p}_{ei}$, with $\mathbf{p}_{ei}$ the momentum of the ith electron, can be determined from the center of mass recoil momentum of the ions, $\mathbf{p}_{\text{R}}^{(n,m)} = \mathbf{p}_{\text{Ar}}^n + \mathbf{p}_{\text{Ar}}^m$, using the relation $\mathbf{p}_e^{(n,m)} = -\mathbf{p}_{\text{R}}^{(n,m)}$.
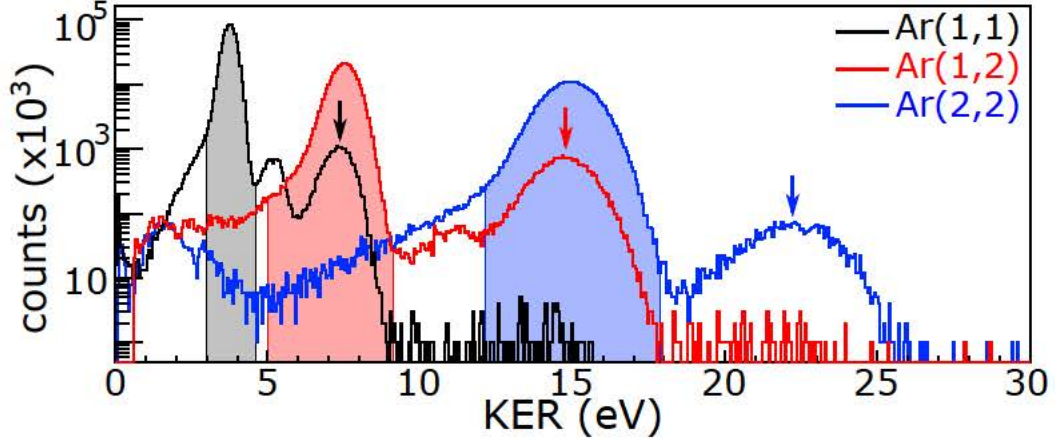
Figure 4.2.1: Kinetic energy released (KER) distributions of fragmentation channels Ar(n, m) with $(n, m) = \{(1, 1), (1, 2), (2, 2)\}$. Arrows mark peaks due to electron recapture, shaded areas highlight the peaks resulting from Coulomb explosion at R_{eq}.

Fig. 4.2.1 displays the measured distributions of the kinetic energy released (KER) during fragmentation, $\text{KER} = \left[(\mathbf{p}_{\text{Ar}}^m)^2 + (\mathbf{p}_{\text{Ar}}^n)^2 \right] / (2M)$ with M the atomic mass of argon, for the Ar(1,1), Ar(1,2) and Ar(2,2) channels. For each channel, at least two characteristic main peaks can be identified. The smaller peaks at higher KER-values (marked by arrows) were attributed to the process of frustrated field ionization [49, 145, 146], see chapter 5. The dominant peaks at lower KER-values, highlighted by colored areas in Fig. 4.2.1, originate from Coulomb explosions of the argon dimers at R_{eq} and are the focus of this chapter.

To obtain insight into the multiple ionization dynamics underlying the colored lower-KER peaks in Fig. 4.2.1, an asymmetry-parameter is introduced: $\mathcal{A}_z^{(n,m)} = (n_{\text{up}} - n_{\text{dn}})/(n_{\text{up}} + n_{\text{dn}})$, where n_{up} (n_{dn}) denote for the channel Ar(n,m) the number of events with a positive (negative) electron sum momentum along z. Alternatively to $\mathcal{A}_z^{(n,m)}$, one could also analyze the mean electron sum momentum $\bar{\mathbf{p}}_{e,z}^{(n,m)}$. But as was shown in section 3.6.1, the two quantities feature an almost identical dependence on the CEP. In the following $\mathcal{A}_z^{(n,m)}$ will be used, as it has the advantage that it can be visually connected to electron yields discussed below. The measured dependence of $\mathcal{A}_z$ on CEP for the Ar(1,2) and Ar(2,2) channels is depicted in Fig. 4.3.1(a).

The key feature in Fig. 4.3.1(a) is that the $\mathcal{A}_z$-curve for the Ar(2,2) channel exhibits a clear left phase shift of about 0.23π rad to that of the Ar(1,2) channel.

4.3 Simulation

As mentioned before, to understand this experimentally observed CEP-shift between the two channels, the collaborating group of Xiaojun Liu from APM in Wuhan was asked to carry out simulations. In these simulations, the motion of correlated electrons and nuclei in the combined laser and Coulomb fields was traced by performing a 3D classical ensemble model calculation [115, 116]. As the laser intensity is well above the over-the-barrier threshold [27, 124] the two outermost electrons are rapidly stripped from each argon atom [115]. Therefore these two initial ionization events were not modeled and instead the simulation is started from a dimer consisting of two singly charged argon ions (Ar^+- Ar^+), with one active electron situated around the position of each ion. For more details about the simulation methods see section 3.6. My interpretation of the produced simulation data is given in this and the following sections.

The CEP-dependence of $\mathcal{A}_z$ predicted by the simulations for the Ar(1,2) and Ar(2,2) channels is shown in Fig. 4.3.1(b). The simulated curves agree very well with the measured ones, in particular the CEP left-shift of the Ar(2,2) channel is very well reproduced. The origin of this phase-shift can be extracted from the simulations by analyzing the distributions of ionization times t_{1st} and $t_{2nd} > t_{1st}$ of the laser-driven electron trajectories that lead to the channels Ar(1,2) and Ar(2,2), respectively. The ionization time t_{1st} marks the instant at which the single-particle energy of the first emitted electron becomes positive for the first time. Likewise, t_{2nd} marks this instant for the second emitted electron in the Ar(2,2) channel. The distributions of t_{1st} and t_{2nd} are plotted in Figs. 4.3.1(c)-(h) for the Ar(1,2) and Ar(2,2) channels and three selected values of the CEP. For convenience of the following discussion, the ionization time-distributions were separated depending on whether the
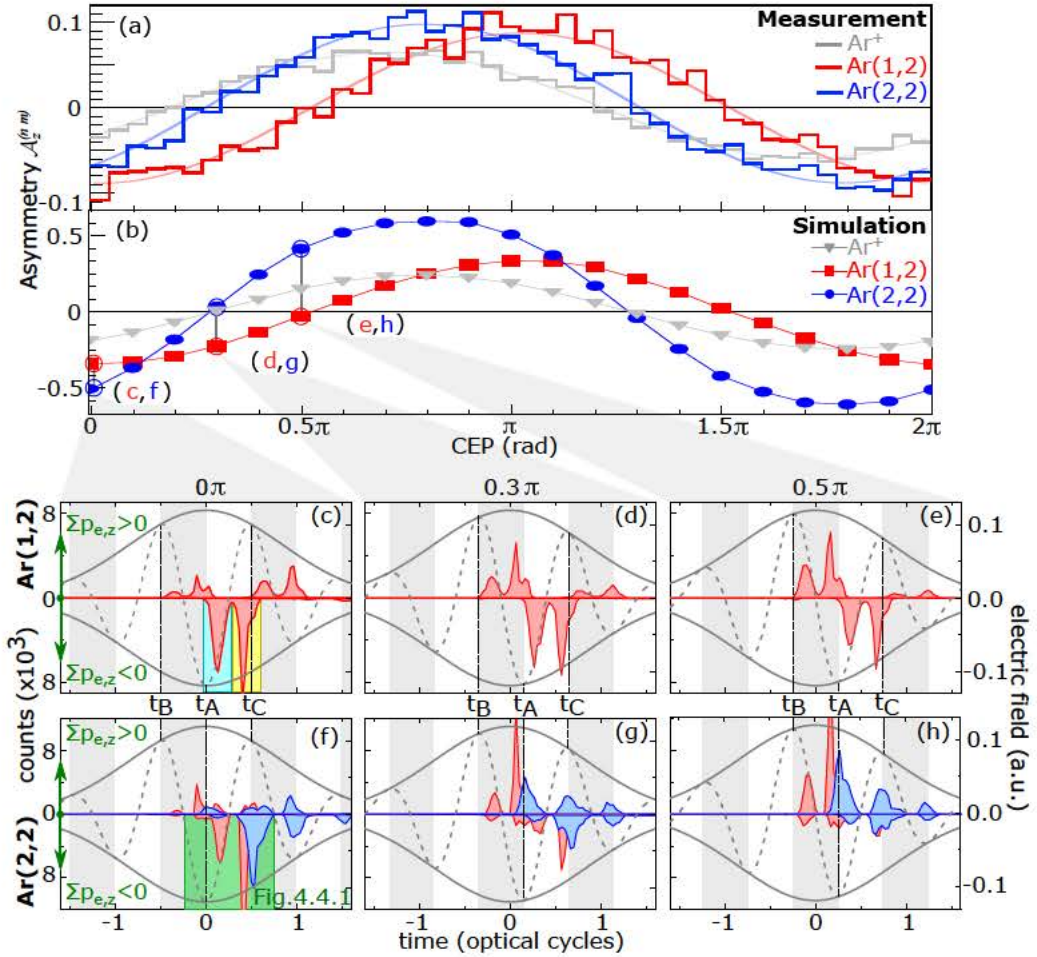
Figure 4.3.1: (a) Measured asymmetry $\mathcal{A}_z^{(n,m)}$ of electron emission along z for Ar(n,m), $(n,m) = \{(1,2),(2,2)\}$ over CEP. (b) Same as (a) but simulated. The curves of the Ar^+ monomer (gray) serve as a reference in (a) and (b). (c-e) Simulated distributions of ionization times of the first electron, t_{1st}, for trajectories leading to Ar(1,2) for three values of the CEP. (f-h) Same as (c-e) but for trajectory pairs leading to Ar(2,2) with the distributions of the ionization times of the second electron, t_{2nd}, shown in blue. The laser electric field $E_z(t)$ (gray dashed) is also shown for reference. The time-distributions are separated depending on whether the (sum) momentum of the electron (pair) reaches positive (upper halves) or negative momentum (lower halves).

(sum) momentum of the electron (pair) reaches positive (upper halves) or negative momentum (lower halves).

To explain the CEP left-shift between Ar(1,2) and Ar(2,2), we will start with the CEP-dependence of $\mathcal{A}_z^{(1,2)}$. As shown in Figs. 4.3.1(c)-(e), the distributions of the ionization times (t_{1st}) in this channel feature two maxima per peak of the laser field. The reason underlying these two maxima will be explained below. For $\varphi_{CEP} = 0$, the two maxima corresponding to the field peak at $\boldsymbol{t_A}$ are marked by cyan and yellow boxes [Fig. 4.3.1(c)]. The maxima corresponding to the field peaks at $\boldsymbol{t_B}$ and $\boldsymbol{t_C}$ are much smaller for $\varphi_{CEP} = 0$. The emission directions of electrons set free during these maxima (up or down, indicated by positive or negative time-distributions) are largely determined by the laser vector potential according to the relation $\mathbf{p}_{e1} = -\mathbf{A}(t_i) = \int_{-\infty}^{t_i} \mathbf{E}(t')dt'$ [28, 29] with t_i the ionization time. Positive values of $\mathbf{A}(t_i)$ are indicated by gray shading in Figs. 4.3.1(c)-(h). The small deviations from $\mathbf{p}_{e1} = -\mathbf{A}(t_i)$ are due to the Coulomb forces of the argon ions.

For $\varphi_{CEP} = 0$, most of the trajectories are emitted with $\mathbf{p}_{e1} < 0$. Therefore, $\mathcal{A}_z^{(1,2)}$ has a large negative value, confer Figs. 4.3.1(a,b). For increasing CEP, the laser field-maximum at $\boldsymbol{t_B}$ shifts closer to the pulse peak and becomes stronger. Accordingly, the positive valued double-peak structure corresponding to the field maximum at $\boldsymbol{t_B}$ becomes gradually larger; at $\varphi_{CEP} = 0.5\pi$ the negative and positive double-peak structures are roughly equal in area. As a consequence, $\mathcal{A}_z^{(1,2)}$ varies from a large negative value at $\varphi_{CEP} = 0$ to roughly 0 at $\varphi_{CEP} = 0.5\pi$. Thus, the CEP-dependence of $\mathcal{A}_z^{(1,2)}$ in Figs. 4.3.1(a,b) can to a good degree be explained straightforwardly using standard strong-field arguments based on the relation $\mathbf{p}_{e1} = -\mathbf{A}(t_i)$ and the sub-cycle dependence of the ionization rate on CEP.

To explain the CEP-dependence of $\mathcal{A}_z^{(2,2)}$ for Ar(2,2), also the distribution of t_{2nd}, blue-colored in Fig. 4.3.1, must be considered. The distributions of t_{1st} in the Ar(2,2) channel, although different in amplitude from those of channel Ar(1,2), are also dominated by two peaks per laser cycle. In contrast, the distribution of t_{2nd} for $\varphi_{CEP} = 0$ in Fig. 4.3.1(f) is dominated by only one

peak. It is delayed by a laser-half-cycle to the strongest field maximum at t_A and points into the negative direction. Again, the reasons for the delay and the single peak-structure will be discussed below. Together with the t_{1st} peaks that also point into the negative direction, this single t_{2nd} peak leads to $\mathcal{A}_z^{(2,2)} < 0$ for $\varphi_{\text{CEP}} = 0$, in agreement with Figs. 4.3.1(a,b). As the CEP increases, the half-cycle-delayed negative t_{2nd} peak due to the decreasing field-maximum at t_A becomes weaker, and the positive t_{2nd} peak due to the increasing field maximum at t_B becomes stronger. Together with the t_{1st} distributions that behave similarly as in the Ar(1,2) case, this causes that $\mathcal{A}_z^{(2,2)}$ moves towards positive values, reaches ≈ 0 for $\varphi_{\text{CEP}} = 0.3\pi$ and a large positive value for $\varphi_{\text{CEP}} = 0.5\pi$ [see Figs. 4.3.1(a,b)].

4.4 Discussion of CEP-dependance of $\mathcal{A}_z$

We now turn to discussing the origin of the t_{1st} double-peak and the half-cycle delayed single-peak structure of t_{2nd}. As we will see, this will also explain the CEP left-shift of $\mathcal{A}_z^{(2,2)}$ relative to $\mathcal{A}_z^{(1,2)}$. To this end, the classical trajectories leading to the Ar(2,2) channel were traced. For simplicity, but without loss of generality, for this in-depth analysis the electron pairs emitted within $[-0.25T, 0.75T]$ and with negative sum momentum for the case of $\varphi_{\text{CEP}} = 0$ is selected [indicated by a green box in Fig. 4.3.1(f)]. The resulting time-distributions, displayed in Fig. 4.4.1(a), show that the emissions can be classified into two types according to the relative emission time of the first and second electrons: One, where the two emissions happen *isolated* of each other ($t_{1st} \in [-0.25T, 0.25T]$), and a second one, where the two emission steps happen in a *concerted* manner within the same half-cycle ($t_{1st} \in [0.25T, 0.75T]$).

Typical trajectories for both the *isolated* and *concerted* case are displayed in Fig. 4.4.1. It will be shown below in section 4.5.2 that they are representative for all emitted trajectories. The trajectories for the isolated case of double ionization (DI) [Figs. 4.4.1(b,c)] show that the first electron is immediately flying away from its own parent nucleus (red curve). The second electron, in
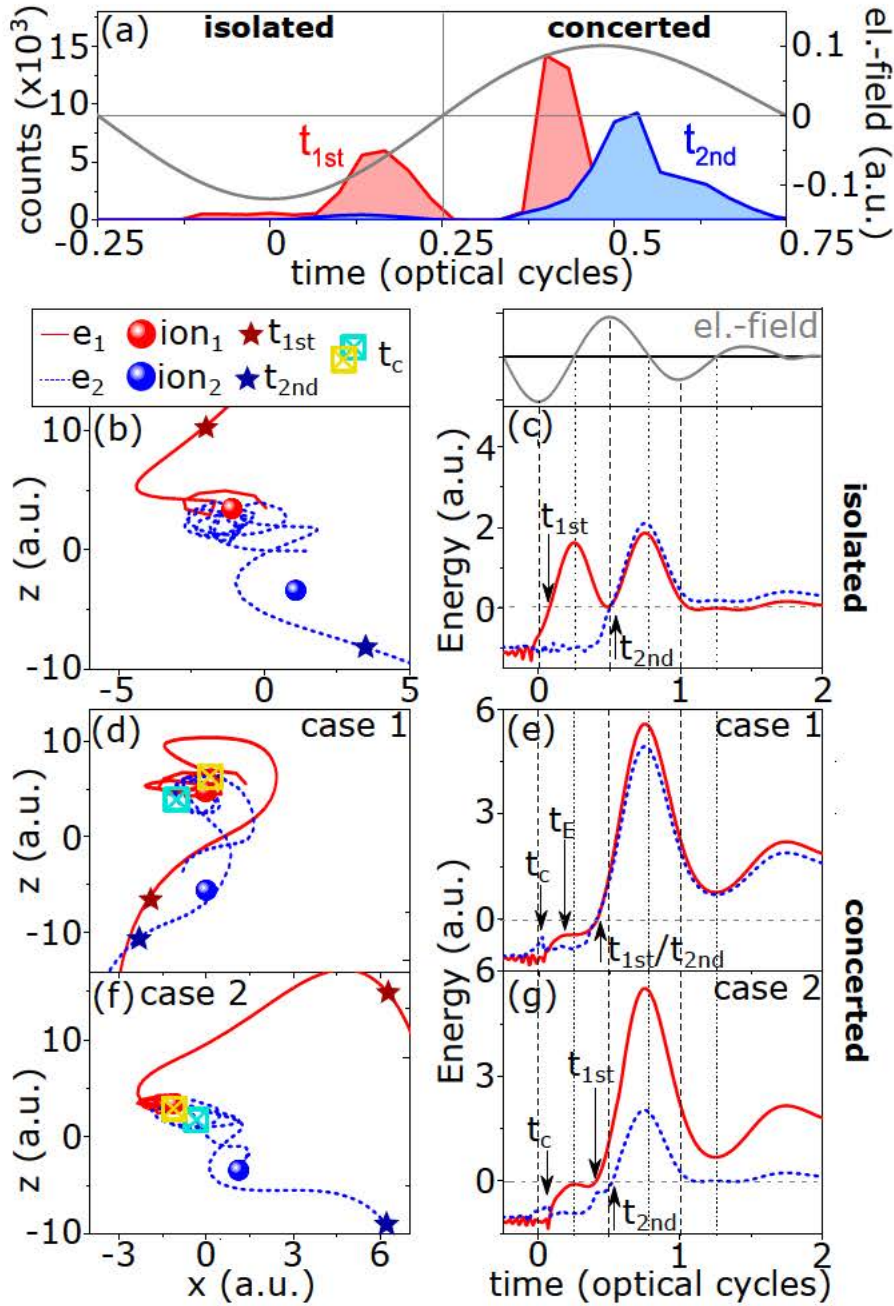
Figure 4.4.1: Classical trajectory analysis for channel Ar(2,2). (a) Ionization time distributions of first (red), t_{1st}, and second (blue), t_{2nd}, electrons for electron pairs emitted within [-0.25T, 0.75T] and with negative sum momentum for $\varphi_{\mathrm{CEP}} = 0$. The left (b,d,f) and right columns (c,e,g) show typical electron trajectories in space and over time, respectively. The trajectories are classified in isolated ($t_{1st} \in [-0.25T, 0.25T]$, (b,c)) and concerted ($t_{1st} \in [0.25T, 0.75T]$, (d-g)). t_C, t_E denote the times of collision and excitation. For better visibilty, the orbits in (b,d,f) are shown for $t > -0.1T$.

71

contrast, is transferred to the other nucleus, where it is subsequently temporally captured by the Coulomb potential of the neighboring Ar^{2+} ion. It becomes ionized only during the next laser-half-cycle around the peak of the field. This electron transfer across the system boundaries and the subsequent capture process that results in the ionization delay will be referred to as LITE.

LITE also plays a significant role in the concerted type of DI. Two cases can be distinguished: Representative electron trajectories [Figs. 4.4.1(d,e)] show that for *case 1* one of the electrons is emitted at one site and transferred to the other site by LITE. There it is captured by the Coulomb potential, collides with the second electron initially on this site, and produces a doubly excited neutral atom, i.e., an Ar^{2+}-Ar^{**} dimer. The highly excited Ar^{**} atom is then doubly ionized before the next peak of the laser field, resulting in an Ar(2,2) dimer. *Case 2* [Figs. 4.4.1(f,g)] starts similarly: An electron is emitted at one site and is transferred to the other by LITE. However, in this case the energy exchange by collisions with the second electron is larger, so that one of the electrons gains enough energy to ionize soon. The other electron loses some of its energy and is trapped by the Coulomb potential, forming a transient Ar^{2+}-Ar^{+*} complex. The captured electron finally ionizes at or after the next peak of the laser field and produces an Ar(2,2) dimer.

This second case is reminiscent of the recollision-induced excitation with subsequent field ionization (RESI) process well-known for monomers [38, 39, 165]. Here, however, the collision-excitation step takes place on a distant entity and is enabled only by a preceding LITE process. Further explanations and a visualization of the role of LITE in the three different DI scenarios, as well as additional data and discussion on the role of the alignment of the argon dimer with respect to the laser polarization direction, the correlation between the two emitted electrons due to the collisions induced by LITE, and a spatio-temporal analysis of the electron transfer will be discussed in section 4.5.

The finding that the DI dynamics to Ar(2,2) is dominated by an electron transfer process (LITE), explains why the second electron emission is delayed
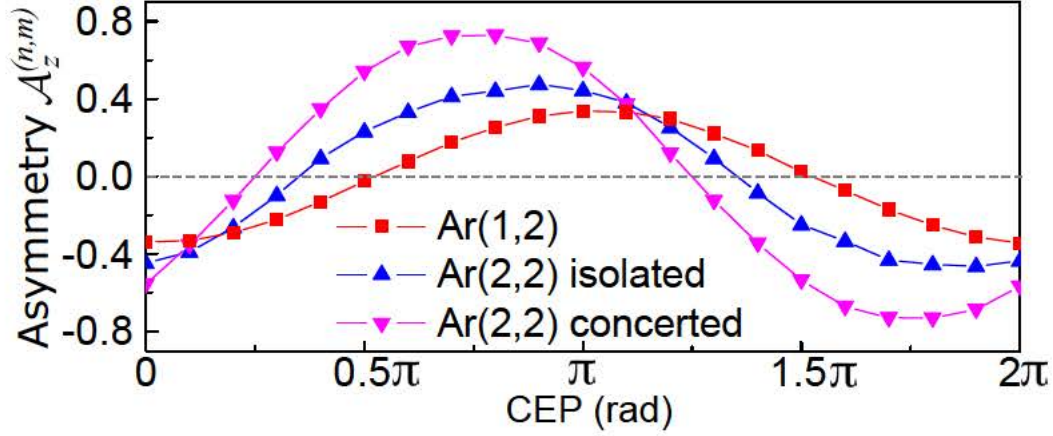
Figure 4.4.2: Simulated CEP-dependence of the asymmetry $\mathcal{A}_z$ for channels Ar(1,2) and Ar(2,2). The latter is separated into isolated and concerted two-electron emissions based on $\Delta t = t_{1st} - t_{A,B,C}$, where $t_{A,B,C}$ (indicated in Fig. 4.3.1) are the instants of the laser field-maxima right before a given t_{1st} peak that initiates the electron emission at t_{1st}: Isolated for $0 \leq \Delta t \leq 0.25T$, concerted for $0.25T \leq \Delta t \leq 0.5T$.

by a laser half-cycle to its initiating laser field-peak [see the t_{2nd} distributions in Figs. 4.3.1(f)-(h)]. Likewise, also the double-peak structure of t_{1st} can be explained by LITE: In the concerted cases of DI the first electron is transferred and therefore is emitted with delay, giving rise to the second peak. The first, undelayed peak arises during the isolated cases of DI and during single ionization (SI) to Ar(1,2). The delayed peak in SI corresponds to cases where the first electron becomes transferred but the second electron stays bound, see Fig. 4.5.2.

Finally, based on the fact that the first ionization step proceeds similarly for the Ar(1,2) and Ar(2,2) channels [see Figs. 4.3.1(c)-(h)], we can now investigate which of the two DI cases, the isolated or the concerted one, is responsible for the distinct CEP-shift observed between the $\mathcal{A}_z^{(1,2)}$ and $\mathcal{A}_z^{(2,2)}$ curves in Figs. 4.3.1(a,b). To see this, in Fig. 4.4.2 $\mathcal{A}_z^{(2,2)}$ separately for the isolated and concerted contributions to Ar(2,2) are plotted, in comparison with $\mathcal{A}_z^{(1,2)}$ taken from Fig. 4.3.1(b). The separated curves reveal that the uncorrelated two-electron emission of the isolated case introduces a notable shift, but the main shift is introduced by the concerted pathway. The reason
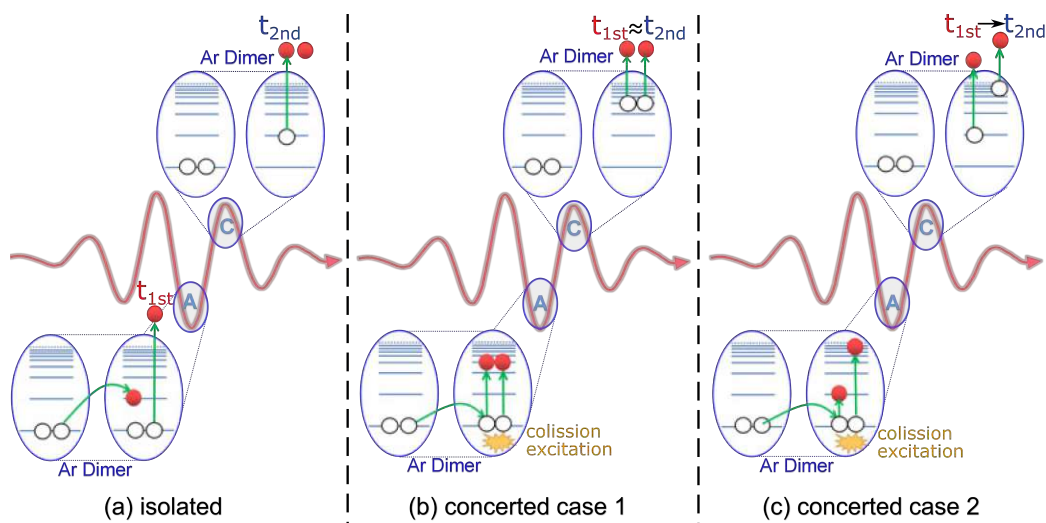
Figure 4.5.1: Visualizations of the influence of the LITE process in the double-ionization dynamics leading to $Ar(2,2)$. The three types of double-ionization described (isolated and concerted cases 1 and 2) are depicted in (a) to (c). The instants of the first (t_{1st}) and second (t_{2nd}) ionization steps are indicated. See text for details.

is that for this case the electron-electron interaction dynamics triggered in the excited argon atom upon electron-transfer by LITE leads to electron emission over a much broader range of time within the laser cycle as compared to a purely field-driven ionization dynamics confined to around the crests of the laser cycle.

4.5 Additional details on the LITE process

Above, in section 4.4 we find by detailed analysis of the electron emission timing that the conspicuous CEP left-shift of the measured asymmetry parameter $\mathcal{A}$ of the $Ar(2,2)$ channel with respect to that of the $Ar(1,2)$ channel is caused by the laser-induced transfer of an electron from one argon atom to the neighboring one (the LITE process).

It is briefly described in Fig. 4.4.1 and corresponding text, that upon transfer of the electron, double ionization may take place via three different cases: in an isolated manner, and two cases of concerted electron emissions. The

different electron dynamics underlying these three cases are visualized in the sketches in Fig. 4.5.1 and will be now discussed in more detail.

In the **isolated** type of double ionization, sketched in Fig. 4.5.1(a), the first electron becomes field-ionized at a peak of the laser field (denoted A in the figure) and is driven away from its own parent nucleus. The second electron, in contrast, is transferred to the other argon ion, where it is temporally captured by this ion's Coulomb potential. It becomes ionized only during the next laser-half-cycle around the peak of the field (denoted C).

In the **concerted case 1** of double ionization, depicted in Fig. 4.5.1(b), one of the electrons is emitted by field-ionization at one argon ion during a peak of the laser field (denoted A in the figure). The electron is then transferred to the other argon ion by the laser field, where it is re-captured by this ion's Coulomb potential. Through collision with the electron already at this site a doubly excited neutral atom, i.e., an Ar^{2+}-Ar^{**} dimer, is created. The two electrons of the highly excited Ar^{**} atom are then emitted quasi-simultaneously during the next peak of the laser field (denoted C), resulting in an $Ar(2, 2)$ dimer.

In the **concerted case 2**, visualized in Fig. 4.5.1(c), an electron is transferred around a peak of the laser field (denoted A in the figure), as in case 1. However, in case 2, the collision of the transferred electron with the electron initially on this site happens such that one of them gains enough energy to ionize soon after. The other electron loses some of its energy and is trapped by the Coulomb potential, forming a transient Ar^{2+}-Ar^{+*} complex. The captured electron finally ionizes around the next peak of the laser field (denoted C) and produces an $Ar(2, 2)$ dimer, such that this second ionization step is delayed by some time to the first one. Case 2 is reminiscent of the recollision-induced excitation with subsequent field ionization (RESI) process well-known for monomers [38, 39]. Here, however, the collision-excitation step takes place on a distant entity and is enabled only by a preceding LITE process.

Electron emission in the $Ar(1, 2)$ channel: As described above in con-
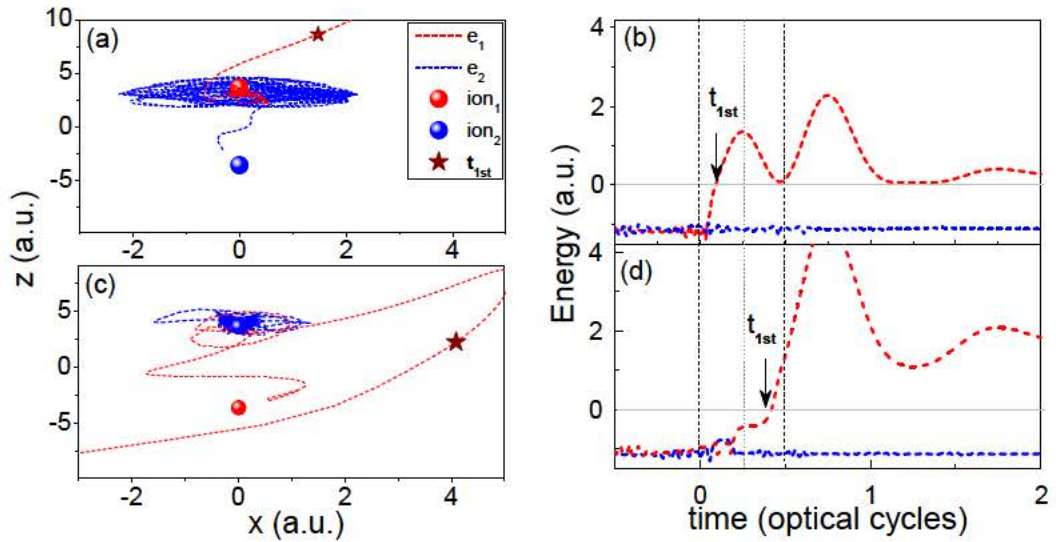
Figure 4.5.2: Typical electron trajectories in space, (a) and (c), and over time, (b) and (d), for channel $Ar(1,2)$. The trajectories in (a) and (b) visualize the emission dynamics leading to the first, undelayed peak in the t_{1st} distributions in Figs. 4.3.1(c)-(e) , while the trajectories in (c) and (d) illustrate the emission dynamics responsible for the second, delayed peak in the t_{1st} distributions. See text for details.

nection to Fig. 4.3.1, the LITE process also plays a significant role for the emission times of the first electron and is responsible for the double peak structure in the distribution of the ionization times t_{1st} in Figs. 4.3.1(c)-(e). Fig. 4.5.2 shows typical electron trajectories in space and over time for the two scenarios underlying the two peaks in the t_{1st} distributions. The trajectories displayed in Figs. 4.5.2(a) and 4.5.2(b) depict dynamics that are similar to the isolated case of double ionization to the $Ar(2,2)$ channel. The electron drawn in red is emitted directly from its nucleus around the peak of the laser field. The electron drawn in blue is transferred to the neighboring ion where it becomes trapped by this ion's Coulomb potential such that only one electron is emitted and the $Ar(1,2)$ channel is reached. This is the dynamics that underlies the first, undelayed peak in the t_{1st} distributions in Figs. 2(c)-(e). The trajectories depicted in Figs. 4.5.2(c) and 4.5.2(d) visualize the dynamics that lead to the appearance of the second, delayed peak in the t_{1st} distributions in Figs. 2(c)-(e). In this case the electron trajectory

76
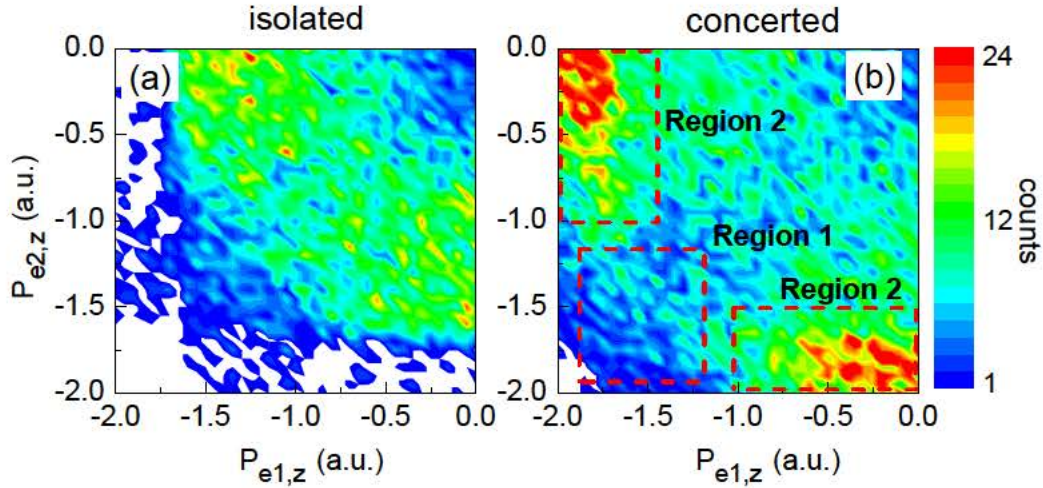
Figure 4.5.3: Two-electron momentum distributions (along z-direction) for electron pairs emitted during isolated (a) and concerted (b) double ionizations.

drawn in blue color stays bound and the electron trajectory drawn in red is transferred to the neighboring argon ion, where it is temporally captured by this ion's Coulomb potential. It becomes ionized only during the next laser-half-cycle around the peak of the field, giving rise to the delayed t_{1st} peak.

With the help of the simulations, additional insight into the details of the LITE process can be obtained from

1. the momentum correlation of the two emitted electrons; see Section 4.5.1

2. the spatiotemporal evolution of electron trajectories; see Section 4.5.2

3. an analysis of the influence of the dimer orientation and the driving forces involved in the electron transfer; see Section 4.5.3.

4.5.1 Two-electron momentum distributions and electron-electron correlation

The different double ionization dynamics leading to $Ar(2,2)$, visualized in Fig. 4.5.1, is largely determined by the field-driven electron-transfer from

one argon ion to the other one (the LITE process). Depending on the specific laser-sub-cycle timing, the transferred electron can excite different electronic dynamics on the distant entity. The three discussed cases of electronic dynamics that can be excited by LITE are also reflected in two-electron momentum distributions, which are a particularly intuitive way of visualizing light-driven sub-cycle electron-electron interaction [122, 166, 167].

Fig. 4.5.3 depicts the momentum of one electron along z versus the same quantity of the other electron, separated into the isolated case [panel (a)] and the two concerted cases [panel (b)] of double ionization. The separation criterion is the instant of the first ionization step, as described above, in the text corresponding to Fig. 4.4.1. In the isolated case, the two electrons are emitted with a significant delay and therefore do not interact with each other. Accordingly, the two electrons are not expected to be momentum correlated with each other. Indeed, this is what can be seen in Fig. 4.5.3(a): The two electrons are emitted over broad ranges of momenta with no particular clustering of probability in the two-electron momentum distribution, consistent with an uncorrelated emission dynamics.

In contrast, the two-electron momentum distribution corresponding to the concerted cases of two-electron emission, depicted in Fig. 4.5.3(b), shows that the two electrons are emitted with a pronounced momentum correlation between them. This is particularly visible in the two areas marked by *Region 2*. In these areas, one of the two electrons is dominantly emitted with a high momentum and the other one with a low momentum. This is consistent with case 2 of the concerted two-electron emission dynamics [visualized in Fig. 4.5.1(c)], during which the two electrons collide with each other after the LITE process. This collision causes that one electron becomes highly excited, ionizes soon after the collision and reaches high momentum, while the other one becomes more strongly trapped on the argon ion, ionizes later and reaches smaller momentum.

To a lesser degree the momentum correlation after the LITE-mediated collision can also be noticed in the momentum region marked by *Region 1*. In this region the two electrons are both emitted with high momentum. This is con-

sistent with the double-ionization dynamics of the concerted case 1 visualized in Fig. 4.5.1(b). As described above, during case 1 one electron is transferred to the neighboring ion by the LITE process, where it collides with the other electron and a doubly-excited argon ion is created. Then both electrons ionize quasi-simultaneously and reach both high momenta. By comparison with the two-electron momentum distribution corresponding to the isolated case, shown in Fig. 4.5.3(a), it can be seen that this quasi-simultaneous emission leads to some enhancement of the probability in this correlated momentum area marked *Region 1*.

4.5.2 Spatiotemporal analysis of electron-electron interaction

Fig. 4.4.1 features example trajectories for the three cases of double-ionization dynamics that are enabled by the LITE process [visualized in Fig. 4.5.1]. To prove that the LITE process is at work during essentially all double ionization events in the $Ar(2, 2)$ channel, and not only during the examples in Fig. 4.4.1 the statistics of the minimum distance $D_{\min}$ between one electron e_i and the neighboring argon ion ion_j for all the trajectories in the $Ar(2, 2)$ channel that fulfill $i, j = 1, 2 \quad i \neq j$ and for three exemplary values of the CEP will be discussed. These distributions are shown in Fig. 4.5.4(a). As can be seen in the figure, the distribution of minimum distances between one electron and the neighboring ion peaks around 0.5 a.u., which is far less than $R_{eq}/2$ for all CEP-values (here $R_{eq} \approx 7.1$ a.u. is the equilibrium distance of the argon dimer). From this it can be deduced that the transfer process, i.e. LITE, takes place for essentially all of the trajectories in the $Ar(2, 2)$ channel.

The same conclusion can be drawn from the distributions of the time Δt that the transferred electrons stay in a small region around the neighboring ion. Fig. 4.5.4(b) depicts these distributions for the same three value of the CEP as in Fig. 4.5.4(a). It can be seen that almost all of the transferred electrons stay only less than half a laser cycle ($\Delta t < 0.5$ optical cycles) in a small region (< 3.6 a.u.) around the neighboring ion. The probability distribution is bimodal with the dominant peak around $\Delta t \approx 0.4$ optical
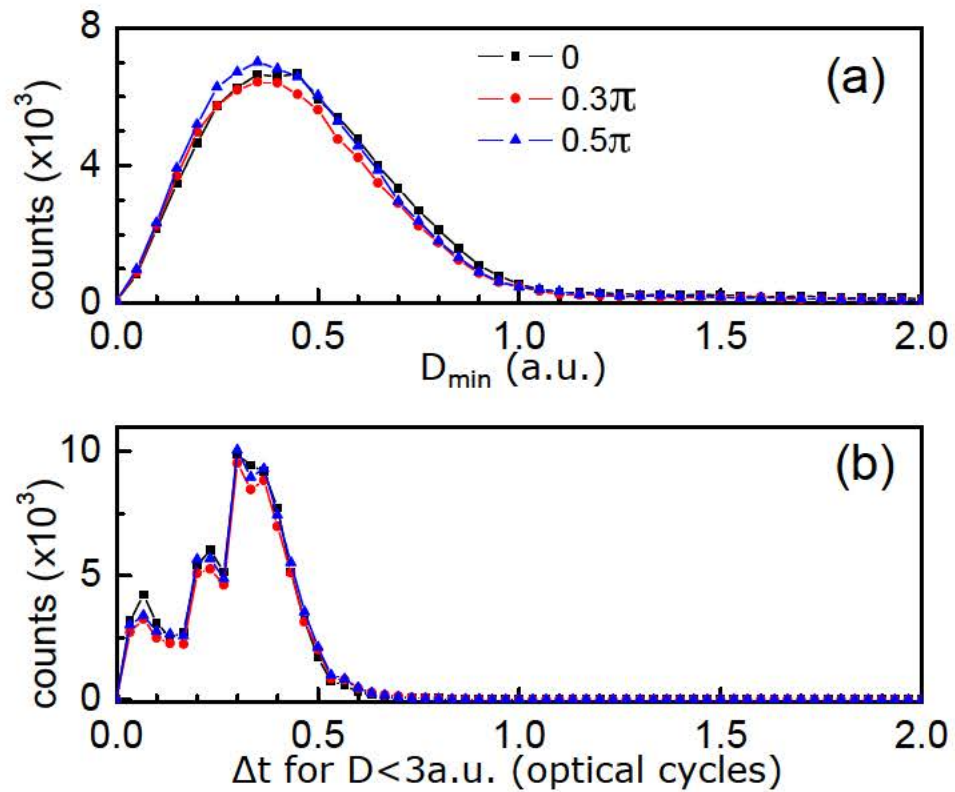
Figure 4.5.4: (a) Distributions (for three values of the CEP) of the minimum distance $D_{\min}$ between one electron and the neighboring ion for all trajectories in the Ar(2, 2) channel. (b) The three distributions corresponding to (a) of the time Δt that the transferred electrons stay in a small region (< 3.6 a.u.) around the neighboring ion.

cycles and a smaller peak around $\Delta t \approx 0.1$ optical cycles. By tracing the corresponding trajectories we find that trajectories in the peak around $\Delta t \approx 0.1$ optical cycles, after their transfer to the neighboring ion by LITE, make mostly only one roundtrip around the ion and then escape. Trajectories that make up the peak around $\Delta t \approx 0.4$ optical cycles make three to four roundtrips around the neighboring argon atom before escaping. These 0.4 optical cycles constitute the dominant contribution to the ionization delay of the transferred electron. In addition, it takes about 0.1 optical cycles for the transferred electron to escape the system. An example trajectory visualizing this timing is depicted in Fig. 4.5.5(b). In that figure the instants when the transferred electron enters and leaves the region around the argon atom to which it is transferred to (t_{in} and t_{out}, respectively) and its ionization time t_{2nd} are indicated. In between t_{in} and t_{out} the transferred electrons makes three roundtrips around the nucleus within about 0.4 optical cycles and then it takes another 0.1 optical cycles to escape the ion's Coulomb potential, leading to a total ionization delay of $\Delta t \approx 0.5$ optical cycles.

Thus, in sum, the distributions in Fig. 4.5.4 clearly prove that essentially all double ionization events in the $\text{Ar}(2, 2)$ channel are dominated by the field-induced transfer of one of the two electrons to the neighboring ion, i.e., by the LITE process.

4.5.3 Influence of dimer orientation

Valuable insight into the dynamics of the LITE process and the double ionization dynamics that it enables can also be obtained from an analysis of the influence of the dimer orientation with respect to the laser polarization direction and the driving forces involved in the electron transfer. Intuitively one would expect some influence of the dimer orientation on the effectiveness of the transfer- and collision processes that underlie the LITE process and therewith the CEP-left shift of the $\text{Ar}(2, 2)$ channel that is revealed by the presented experiments.

To investigate the influence of the dimer orientation in Fig. 4.5.5(a) the CEP-
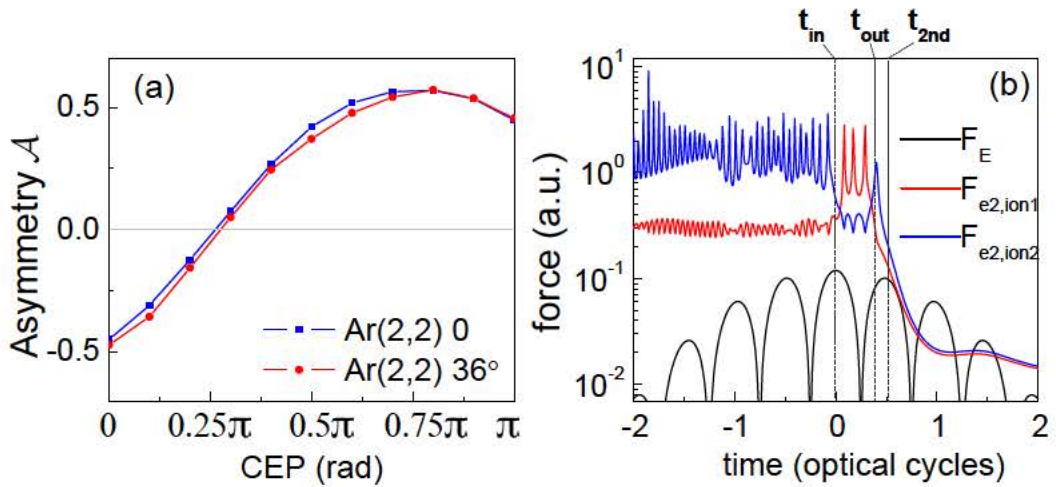
Figure 4.5.5: (a) Simulated asymmetry parameter as a function of CEP for the Ar(2, 2) channel for two orientation angles (0° and 36°) of the dimer axis with respect to the laser polarization direction. (b) Absolute value over time of the force on the transferred electron shown by the blue trajectory in Figs. 4.4.1(f) and 4.4.1(g) , separated into the different contributions due to the laser electric field, F_E (black), the Coulomb force between this electron and its neighboring ion, $F_{e2,ion1}$ (red), and the Coulomb force between this electron and its own ion, $F_{e2,ion2}$ (blue). The instants when the transferred electron enters and leaves a small radius around the argon atom to which it is transferred to (t_{in} and t_{out}, respectively) and its ionization time t_{2nd} are indicated. See text corresponding to Fig. 4.5.4 for a detailed description of these times.

dependence of $\mathcal{A}_z^{(2,2)}$ at the two orientation angles $0°$ and $36°$ with respect to the laser polarization direction is plotted. The relatively small angle $36°$ is chosen to ensure a high enough yield of the $\text{Ar}(2,2)$ channel, which peaks strongly along the laser polarization direction [49, 116, 145, 147]. For $0°$ the Ar dimer axis is parallel to the laser polarization. Therefore, as the opposing Ar atom is situated directly along the direction of the laser field's force, the LITE process is expected to happen with a higher probability as compared to a dimer aligned with $36°$ to the laser polarization direction. Therefore, since the LITE process is responsible for the CEP-left shift in the presented experiments, as established in 4.4, one would expect that the asymmetry parameter for the $0°$ case is further left-shifted from that of the $36°$ case. Indeed, this is what Fig. 4.5.5(a) shows. However, the left-shift is very small. Thus, the dimer alignment with respect to the laser polarization direction has little influence on the LITE process.

The reason for this minor influence of the dimer orientation on the LITE process can be ascribed to the fact that the Coulomb forces between the transferred electron and the argon ions rather than the laser field play the main role in the LITE process. This is shown in Fig. 4.5.5(b) for a representative example trajectory [displayed in Figs. 4.4.1(f) and 4.4.1(g)]. As long as the transferred electron is in the vicinity of its parent ion, the Coulomb force of this ion (in blue) dominates over the force due to the laser electric field (in black). Around the peak of the laser pulse the electron is transferred to the neighboring ion. At this point, the Coulomb force of that ion (in red) becomes the dominant one, and the electron becomes transiently trapped by the neighboring ion. After a short time of about a laser half cycle the electron becomes driven away by the laser force. In sum, because the Coulomb force of the neighboring ion dominates the transfer and transient trapping process, the dimer orientation with respect to the laser polarization direction is of minor importance and only marginally affects the CEP-dependence of $\mathcal{A}_z^{(2,2)}$.

4.6   Conclusion

In conclusion, in this chapter an experimentally and theoretically study on the ionization- fragmentation dynamics of argon dimers in intense few-cycle laser pulses with a known CEP was discussed. A distinct CEP-shift of the electron emission asymmetry between the $Ar^+ + Ar^{2+}$ and $Ar^{2+} + Ar^{2+}$ fragmentation channels was observed. Using a classical ensemble model it is found that this CEP-shift is due to electron-electron interaction mediated by a field-driven electron transfer process (LITE) from one argon atom to the other. This work, thus, heralds the possibility to use strong laser fields for controlling sub-cycle inter-molecular electron-transfer processes where the transferred electron can excite electronic dynamics on a distant molecule. This finding opens up a new route for controlling molecular processes with intense laser pulses beyond mere bond-breaking reactions.

"Life gets really complicated if you think too much."

— Sir Terry Pratchett, *Nation*

Chapter 5

Laser-subcycle control of electronic excitation across system boundaries

In this chapter the results of a joint experimental and numerical study on the sub-cycle laser field-driven electron dynamics that underlie the population of highly excited electronic states in multiply ionized argon dimers by electron recapture processes will be discussed. The experiments using few-cycle laser pulses with a known carrier-envelope phase (CEP) in combination with re-action microscopy reveal a distinct CEP-dependence of the electron emission and recapture process and, furthermore, a small but significant CEP shift to the scenario in which no excited argon dimers are produced. With the help of classical ensemble trajectory simulations these different CEP-dependencies are traced down to subtle differences in the laser-driven sub-cycle electron trajectory dynamics that involve in both cases the transfer of an electron from one argon ion across the system boundary to the neighboring ion and its transient capture on this ion.

85

5.1 Motivation

One of the most intensely studied process of the last 15 years in strong-field laser-matter interaction was the control of intramolecular electron-localization during the ionization-dissociation of isolated, small molecules with tailored laser fields. Such localization was demonstrated along one spatial dimension using the CEP of linearly polarized intense few-cycle laser pulses [132–136], the relative phase between different frequencies in intense multicolor waveforms [168–173], and even in two spatial dimensions using the CEP of elliptically polarized few-cycle pulses [174] or different two-dimensional intense multicolor waveforms [175–177]. More important for applications than the localization of charge within a *single* molecule is, however, the relocalization of charge between *different* molecules: Charge transfer between closely-spaced molecules is the main driving action behind immensely important processes such as photosynthesis [130, 131], photocatalysis [128, 129, 178], or solar-driven energy production [126, 127].

In the previous chapter, also using the argon dimer Ar_2 as a model system for two closely-spaced but separate quantum entities, for the first time CEP-control over electron transfer reactions across system boundaries was demonstrated. It was shown that an electron emitted from one argon atom and driven to the other atom by the strong laser field, can become transiently captured before it leaves towards the detector. This process was titled LITE. In order that the transferred electron can initiate a reaction at the distant site, such as it is the case upon charge-transfer in the processes mentioned above, it is crucial that the transferred electron is not only transiently captured but becomes trapped at the acceptor site in an excited electronic state. It has been shown that population of excited states or even highly excited (Rydberg) states can entail a variety of molecular reactions. In the simplest case this can lead to the breakage of a bond in the excited molecule [53–55, 59, 60]. However, it can also initiate extremely complex dynamics. For example, the transfer of an electron can entail bond-breaking in the donor or acceptor molecule coupled with the transfer of a (radical) moiety to or from the acceptor molecule [56–58, 61], a process of fundamental importance

across many areas of chemistry and biology.

It has been shown in many experiments that also this process, the population of Rydberg states, can take place in a strong laser field. In this process, known as FFI, laser field-emitted electrons that have negligible kinetic energy after the completion of the intense laser pulse, become trapped by the attractive Coulomb potential of an atomic or molecular ion [43, 46–49, 145, 146, 152, 179–184]. In detail, the trapping process not only depends on the energy of the electrons but also on the shape and orientation of their orbits. Capitalizing on this, control over the population of Rydberg states by FFI using orthogonal two-color (OTC) fields was demonstrated [47].

In this chapter, the results of a joint experimental and numerical work conducted with the aim of obtaining insight into the sub-cycle laser field-driven electron dynamics that underlie the population of excited states by the FFI process in a quantum system with two separate entities are reported and discussed. As in the previous chapter, also for this investigation, the argon dimer was chosen as model system with two independent atoms separated by the relatively large distance of a vdW bond. In the experiments, few-cycle laser pulses with a known CEP in combination with reaction microscopy [113, 114] to record the products of the laser-dimer interaction are used. By that, a distinct CEP-dependence of the electron emission and subsequent electron trapping (or recapture) process that is responsible for the population of excited (Rydberg) states is found. Moreover, a slightly different CEP-dependence of the electron emission process in the argon dimers where no excited states are populated are found, which manifests itself as a small CEP-shift to the recapture case. With the help of simulations using a three-dimensional (3D) classical ensemble trajectory model the CEP-dependencies and CEP-shift are traced down to subtle differences in the intricate laser-driven sub-cycle electron trajectory dynamics. These involve in both cases the transfer of an electron from one argon ion across the system boundary to the neighboring ion and its transient capture on this ion. Furthermore, the localization of the Rydberg electron during fragmentation of the argon dimer via Coulomb explosion will be discussed.

5.2   Experiment

In the experiments, the supersonic expansion of a few bars of argon gas into an ultra-high vacuum chamber produces a dilute gas jet that contains a small fraction (few percent) of vdW-bound argon dimers. The gas jet, propagating along the x-direction of the lab coordinate system, is intersected in the interaction chamber (background pressure $< 10^{-10}$ mbar) of a COLTRIMS reaction microscope, also applied, e.g., in Refs. [4, 46, 47, 174, 184], with a laser beam propagating along y-direction delivered by a Titanium-Sapphire multi-pass laser amplifier system, focused onto the gas jet by a spherical mirror with a focal length of 60 mm. The pulses in the beam were linearly polarized along z-direction and had an FWHM duration in intensity of 4.5 fs, a center wavelength $\lambda = 750$ nm and a peak intensity, calibrated in *in situ* [163], of 5×10^{14} W cm^{-2}. The few-cycle laser pulses were generated by spectral broadening in a gas-filled hollow-core capillary and subsequent temporal recompression of the 25 fs pulses emerging from the laser amplifier system.

The interaction of the intense few-cycle laser pulses with the atoms and dimers in the gas jet led to ionization of the argon atoms and ionization-fragmentation of the argon dimers. The generated ions were guided over a distance of 5.7 cm towards a position sensitive multi hit-capable detector by a weak electric field of 3 V/cm, where the position and time-of-flight (TOF) of each ion was recorded. The emitted electrons were not detected in the present experiments. From the ions' impact positions and TOF values the three-dimensional momentum of each detected ion was calculated. In the argon dimers, the vdW-bound argon atoms are separated by their R_{eq} and upon multiple laser ionization undergo fragmentation via Coulomb explosion described by the reactions $Ar_2 \xrightarrow{\text{Laser}} Ar_2^{(n+m)+} + 2e \rightarrow Ar^{n+} + Ar^{m+} + 2e$. These different ionization-fragmentation channels that result in the production of two argon ions, Ar^{n+} and Ar^{m+}, are denoted by $Ar(n, m)$.

In order to select a specific two-body channel $Ar(n, m)$, the density of the gas jet was kept low, such that on average less than 0.3 ions per laser shot hit

the detector. Under these coincidence conditions, a specific channel $Ar(n, m)$ can be selected in the offline data analysis from the more abundant atomic ionization events by imposing momentum conservation conditions. From the many different ionization-fragmentation channels that were detected in the experiments, in this chapter we are specifically interested in the channels Ar(1,2) and Ar(2,2).

In the experiments, the CEP of the few-cycle laser pulses was allowed to fluctuate freely and a single-shot stereo electron spectrometer in phase-tagging mode [105, 185] was used to measure the CEP of each and every laser pulse and additionally to monitor the duration of the laser pulses [107] during the experiments. In the offline data analysis the CEP of each laser pulse was linked to the momenta of the ions detected for this pulse. The unknown constant offset value of the measured CEP values that is inherent to the phase-tagging technique was calibrated to the absolute CEP values of the simulations by overlapping the measured and simulated asymmetry values (defined below) of electron/ion emission over CEP in the single ionization channel $Ar \xrightarrow{\text{Laser}} Ar^+ + e^-$ of the argon monomer. Because the Ar^+ monomer ions are the most abundant species produced both in the simulations and experiments, the statistical error bars in the data are very small. As a result, they can be fitted by sinusoidal functions with very high accuracy. The uncertainty in the CEP obtained from these fits was about $0.005\,\text{rad}$ and $0.003\,\text{rad}$ for the measured and simulated data, respectively. Thus, by this procedure the unknown, constant CEP-offset of the experiment is precisely connected to the CEP-value of the simulations. Further details on the few-cycle laser setup and reaction microscope can be found in chapter 3 and Refs. [1, 4, 42, 174, 186].

The KER during the Coulomb explosion leading to the channels Ar(1,2) and Ar(2,2) was calculated from the measured momentum vectors. The KER-distributions, depicted in Fig. 5.2.1(a), show characteristic peaks. In each fragmentation channel, the most dominant peak can be attributed to the Coulomb explosion from the equilibrium internuclear distance (R_{eq}) of about $7.1\,\text{a.u.}$ and weaker peaks at higher KER to FFI [49, 145, 146]. The FFI
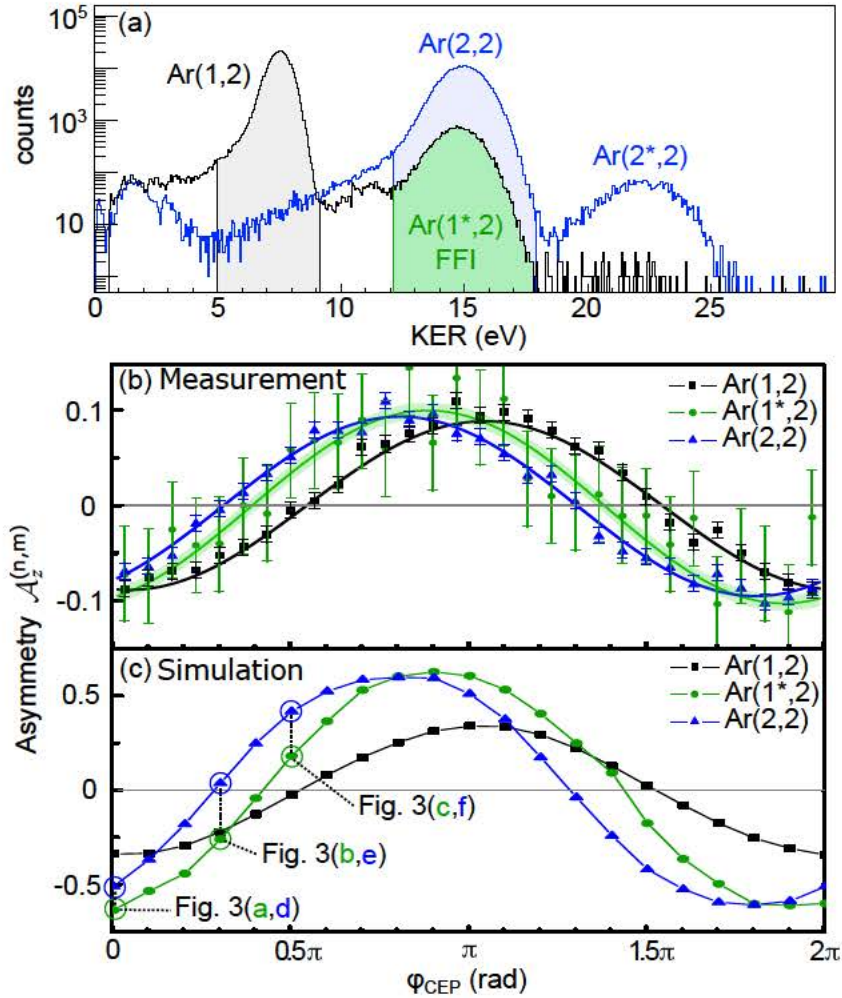
Figure 5.2.1: (a) Kinetic energy released (KER) distributions of fragmentation channels Ar(1,2) and Ar(2,2). The shaded green area around 15 eV highlights the KER peak corresponding to the Ar(1*,2) channel, where each of the two argon atoms becomes first doubly ionized and subsequently one of the electrons is recaptured in a Rydberg state at one of the two Ar^{2+} ions. (b) Experimentally determined asymmetry $\mathcal{A}_z^{(n,m)}$ of electron emission along the laser polarization direction z for the fragmentation channels Ar(1,2), Ar(2,2) and Ar(1*,2) over CEP, reconstructed from the measured ion momenta as described in the text. Statistical error bars corresponding to $\pm 1\sigma$ around the mean values are indicated for all channels. The lines are fits to the data points using the Levenberg-Marquardt algorithm, taking into account the statistical error bars. The $\pm 1\sigma$ confidence interval of the fit is indicated for the Ar(1*,2) channel by the green shaded area around the curve. For the two other channel the confidence interval of the fits is smaller than the width of the lines. (c) Asymmetry values of the same channels $\mathcal{A}_z^{(n,m)}$ as in (b), but simulated using the 3D classical ensemble model described in the text.

90

process starts with the $n + m + 1$ times ionization of the argon atoms in the dimer. Subsequently, one of the released electrons is recaptured by the Coulomb potential of one of the two argon ions into a Rydberg state, leading to the formation of a highly excited argon ion.

In the following we will focus on the case where each argon atom is ionized two times and one of the four emitted electrons is recaptured by one of the two argon ions leading to a dimer $Ar^{+*} - Ar^{2+}$ that is composed of a dication and a highly excited singly charged ion. Upon Coulomb explosion of this dimer, the excited Ar^{+*} ion is detected as a singly charged ion in coincidence with a doubly charged ion. Thus, these Coulomb explosion events are selected as belonging to the Ar(1,2) channel. However, because the Rydberg electron on the Ar^{+*} with its widely extended wavefunction only weakly shields the nuclear charge, its effective charge state sensed by the neighboring ion in the dimer is not $+1$ but almost $+2$. Therefore, the mean KER value obtained during the Coulomb explosion of the $Ar^{+*} - Ar^{2+}$ dimer is almost as high as that in the Ar(2,2) channel [49, 145, 146], cf. Fig. 5.2.1(a). We will from now on refer to this ionization-fragmentation channel as Ar(1*,2).

A corresponding FFI process takes place for argon dimers in the jet, from which initially three respectively two electrons are emitted from each argon atom and an $Ar^{3+} - Ar^{2+}$ dimer is formed upon ionization. At the conclusion of the laser pulse one of the released electrons is recaptured by the Ar^{3+} ion and a highly excited Ar^{2+*} ion is formed. The Coulomb explosion of this $Ar^{2+*} - Ar^{2+}$ dimer is reflected by the KER-peak around 23 eV in the distribution corresponding to the Ar(2,2) channel.

As described above, in this chapter we are interested in the laser field-driven electron dynamics that underlies the electron recapture process to a Rydberg state in an argon dimer. It was shown in the previous chapter that detailed insight into the field-driven electron emission dynamics can be gained from the CEP-dependence of the mean electron sum momentum of all emitted electrons. By this approach, the importance of the electron transfer process (LITE) in the ionization-fragmentation dynamics of the dimers was shown. Motivated by this result, this approach is readopted in the present work.

Because here we are interested in the combined action of the LITE and FFI-excitation processes, we compare in the following the CEP-dependencies of the mean electron momentum in the Ar(1*,2) and Ar(2,2) channels. Since the formation of both channels starts with the emission of two electrons from each argon atom in the dimers, but the field-driven dynamics differs by the recapture process to the Rydberg state, it is reasonable to expect that information on the recapture process can be gained from the differences in the CEP-dependence of the mean electron momentum.

To obtain the mean electron momentum, momentum conservation is used. Due to momentum conservation, the center of mass recoil momentum of the detected argon ions $\mathbf{p}_{R}^{(n,m)} = \mathbf{p}_{Ar}^{n} + \mathbf{p}_{Ar}^{m}$ is connected to the sum momentum of the emitted electrons $\mathbf{p}_{\Sigma e}^{(n,m)} = \sum_{i=1}^{n+m} \mathbf{p}_{ei}$, with $\mathbf{p}_{ei}$ the momentum of the ith electron, via the relation $\mathbf{p}_{\Sigma e}^{(n,m)} = -\mathbf{p}_{R}^{(n,m)}$ (for which the small photon momenta are neglected). From the measured ion momenta, thus the mean value of the electron sum momentum distribution can be obtained, which for the channel Ar(n, m) will be denoted by $\langle \mathbf{p}_{\Sigma e}^{(n,m)} \rangle = -\langle \mathbf{p}_{R}^{(n,m)} \rangle$. As the laser field is linearly polarized along z, the electrons are mainly driven along this direction and the CEP-dependence of the laser-dimer interaction can be well studied by analyzing the mean value of the center of mass ion momentum distribution along z, which is $\langle p_{R,z}^{(n,m)} \rangle$ (see also chapter 4).

However, as was shown previously, in section 3.6.1 , that alternatively to $\langle p_{\Sigma e,z}^{(n,m)} \rangle = -\langle p_{R,z}^{(n,m)} \rangle$ an asymmetry-parameter with the same information content can be used to quantify the electron emission. This asymmetry-parameter has the advantage that it can be directly compared to the simulated electron ionization time distributions that will be introduced in Fig. 5.4.1. The asymmetry-parameter is defined as $\mathcal{A}_{z}^{(n,m)} = (n_{up}^{e} - n_{dn}^{e})/(n_{up}^{e} + n_{dn}^{e})$, where n_{up}^{e} (n_{dn}^{e}) are the number of events with a positive (negative) electron sum momentum in z-direction in the Ar(n, m) channel. However, because in the experiments only the ions are detected, the number of events n_{up}^{i} (n_{dn}^{i}) with positive (negative) ion sum momentum, $p_{R,z}^{(n,m)}$, was used instead to calculate the asymmetry-parameter for the ions $\mathcal{A}_{z}^{i,(n,m)} = (n_{up}^{i} - n_{dn}^{i})/(n_{up}^{i} + n_{dn}^{i})$. This asymmetry parameter is unambiguously connected to the electron

asymmetry parameter analyzed in the following by $\mathcal{A}_z^{(n,m)} = -\mathcal{A}_z^{i,(n,m)}$.

The measured and simulated $\mathcal{A}_z^{(n,m)}$ curves over CEP for the two channels of interest, Ar(2,2) and Ar(1*,2), are shown in Figs. 5.2.1(b) and 5.2.1(c), respectively. As a reference, the $\mathcal{A}_z$-curves for the channel Ar(1, 2) are also shown in the figures. The relatively large CEP-shift of $\mathcal{A}_z$ between the channels Ar(1, 2) (black curve) and Ar(2, 2) (blue curve) was investigated in the previous chapter and was found to be caused by the transient recapture of an electron that is transferred from one argon atom to the other, i.e. by the LITE mechanism.

In the present chapter we are interested in the origins of the much smaller CEP-shift of $\mathcal{A}_z$ between the channels Ar(2,2) and Ar(1*,2). Because both channels start with the emission of two electrons from each argon atom, one is tempted to assume that the CEP-shift is due to the electron recapture process that is present for the Ar(1*,2) but not for the Ar(2,2) channel. However, as will be shown below, in detail the situation is much more complicated.

Given the small CEP-shift between the Ar(2,2) and Ar(1*,2) channels and the relatively low event numbers in the Ar(1*,2) channel, a thorough statistical analysis to corroborate the significance of this small CEP-shift and to obtain its value was performed. The measured distributions of $\mathbf{p}_{\Sigma e} = -\mathbf{p}_R$ for the two channels, from which the corresponding asymmetry parameters $\mathcal{A}_z$ are obtained, contain about 2.7×10^4 and 3.9×10^5 events for the channels Ar(1*,2) and Ar(2,2), respectively. These distributions are divided into 30 bins for the CEP-range 0 to 2π. For each of the 30 bins filled with about 890 respectively 1.3×10^4 events, assuming normal distribution, the mean value of the $\mathcal{A}_z$ value and the statistical $\pm 1\sigma$ error bar was calculated. These are the data shown in Fig. 5.2.1(b). The data were then fitted by sinusoidal functions $f(\varphi_{CEP}) = A\sin(\omega\varphi_{CEP} + \varphi_0) + f_0$ with a fixed periodicity of $\omega = 2\pi$ using the Levenberg-Marquardt algorithm, taking into account the statistical error bars. The $\pm 1\sigma$ confidence interval of φ_0 for the Ar(1*,2) channel is indicated in Fig. 5.2.1(b) by a green shaded area around the curve. For the other channels shown in the figure this confidence interval is smaller than the width of the lines. To quantify the value of the CEP-shift between

the Ar(2,2) and Ar(1*,2) channels, Welch's t-test was used, testing for the hypothesis that the difference of $\varphi_{0,1} - \varphi_{0,2} > \Delta$, where Δ is a certain test-value of the experimentally observed CEP-shift between the two channels Ar(1*,2) and Ar(2,2), which is denoted here for the sake of brevity by 1 and 2, respectively. For a significance level of 0.05 and the number of events and bins given above, the maximum CEP-shift Δ that still fulfills the test-hypothesis (p-value 0.0499) is 11.25° equivalent to 0.063π rad.

5.3 Simulation

As mentioned previously, to gain insight into the field-driven electron dynamics underlying the experimentally observed CEP-shift between the $\mathcal{A}_z$-curves of the Ar(1*,2) and the Ar(2,2) channels depicted in Fig. 5.2.1(b), 3D classical ensemble model calculations [115, 116] were performed by the collaborating group of Xiaojun Liu from APM. This numerical model incorporates the interaction between electrons and nuclei in the intense laser field using Newton's classical equations and allows tracing their trajectories during and after the laser pulse. For more details about the simulation method see section 3.6. My interpretation of the produced simulation data is given in this and the following sections.

The simulated CEP-dependence of $\mathcal{A}_z$ for the three channels of interest is depicted in Fig. 5.2.1(c). As can be seen, the amplitude of the $\mathcal{A}_z$-modulation is significantly larger in the simulated data than in the experimental one. This is a consequence of the neglect of quantum effects in the model and possibly also of treating the ions as point charges. As a consequence, the simulated electron momentum distributions are somewhat narrower than the measured ones (see Fig. 3.6.2), translating into larger asymmetry values. However, Fig. 5.2.1(b) shows that the simulated CEP-dependence of $\mathcal{A}_z$ is very similar to the measured curves for all three channels of interest. In particular, the right phase shift between the Ar(1*,2) and Ar(2,2) channels observed in the experiment is well reproduced, albeit with a slightly larger value of about 0.1π rad. As mentioned above, the CEP-shift between the
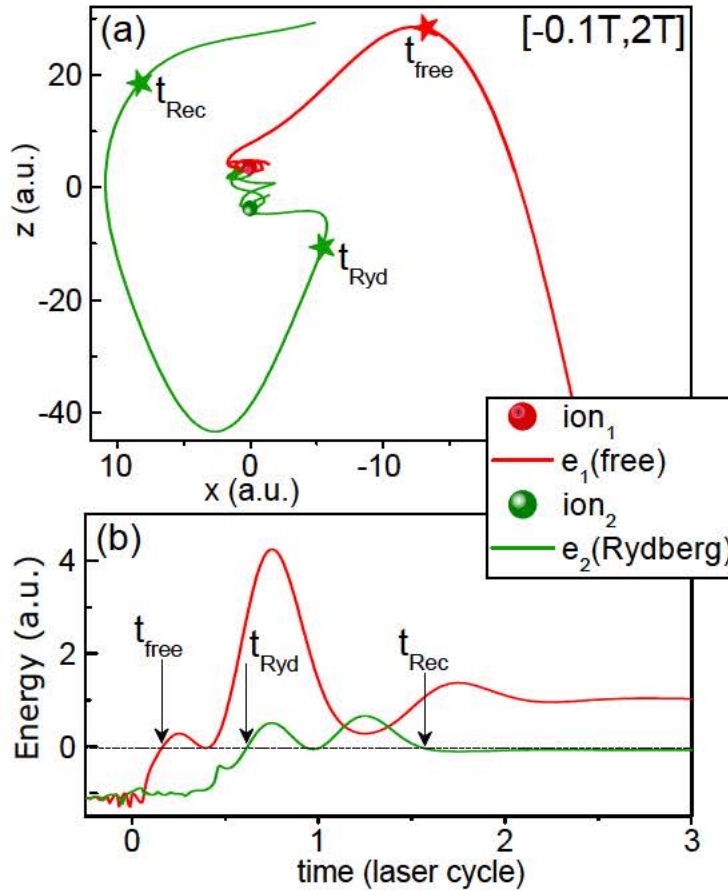
Figure 5.3.1: (a) Typical electron trajectories in the polarization plane xz of the Ar(1*,2) channel for the time range $[-0.1T, 2T]$, where T is the laser cycle duration. (b) The energy of the two trajectories from (a) over time. The instants t_{free}, t_{Ryd} and t_{Rec} are defined in the text.

Ar(1, 2) and Ar(2,2) channels is due to the LITE process that leads to a time delay for the ionization of the second electron. The origin of the much smaller CEP-shift between the Ar(1*,2) and Ar(2,2) channels will be discussed in the following.

To obtain insight into the experimentally observed CEP-shift between the Ar(1*,2) and Ar(2,2) channels the aforementioned numerical model is used (section 3.6). It has been shown previously that in about 80% of all cases Rydberg states in argon dimers are populated by electron recapture via the FFI mechanism rather than by resonant excitation [49, 145, 146]. An analysis of

the electron trajectories simulated using the aforementioned model confirms this value. Hence, the CEP-shift between the Ar(1*,2) and Ar(2,2) channels is dominantly caused by differences in the motion of the field-driven electrons rather than absorption and emission processes. To reveal these differences the 3D classical trajectory model described above was used to simulate the field-driven two-electron emission dynamics $Ar^+ - Ar^+ \rightarrow Ar^{2+} - Ar^{2+} + 2e$ for the Ar(2,2), and the two-electron emission dynamics with the subsequent recapture process $Ar^+ - Ar^+ \rightarrow Ar^{2+} - Ar^{2+} + 2e \rightarrow Ar^{+*} - Ar^{2+} + e$ for the Ar(1*,2) channel, respectively. A typical electron trajectory in space and energy over time leading to channel Ar(1*,2) as predicted by the simulation model is shown in Figs. 5.3.1(a) and 5.3.1(b), respectively. The corresponding figures for a typical trajectory that leads to the Ar(2,2) channel can be found in chapter 4.

For a statistical analysis of the about 10^6, 6×10^3 and 7.5×10^4 trajectories in the Ar(1,2), Ar(1*,2) and Ar(2,2) channels, respectively, that were propagated in the simulations decisive instants that characterize each trajectory were defined. For the trajectories of the two electrons in the Ar(2,2) channel these are t_{1st} and $t_{2nd} > t_{1st}$, which are the instants when the two electrons become emitted. These instants are defined by the criterion that the energies of the respective trajectories exceed the binding energy of their parent argon cation for the first time. For the trajectories of the two electrons in the Ar(1*,2) channel the situation is somewhat complicated by the fact that one of the two electrons is not only emitted but becomes recaptured some time after its emission. Thus, it necessitates two instants, t_{Ryd} and t_{Rec}, to characterize this recaptured trajectory. The first instant, t_{Ryd}, marks the moment of the emission of this trajectory, defined by the same energy criterion as in the other channel. The second instant, t_{Rec}, marks the moment when the trajectory becomes recaptured, defined as the instant when the energy of the trajectory changes from positive to negative and stays negative until the end of the simulation long after the laser pulse has passed. To characterize the other, non-recaptured trajectory in the Ar(1*,2) channel it is sufficient to only define its time of emission, t_{free}, by the same energy criterion as all

96
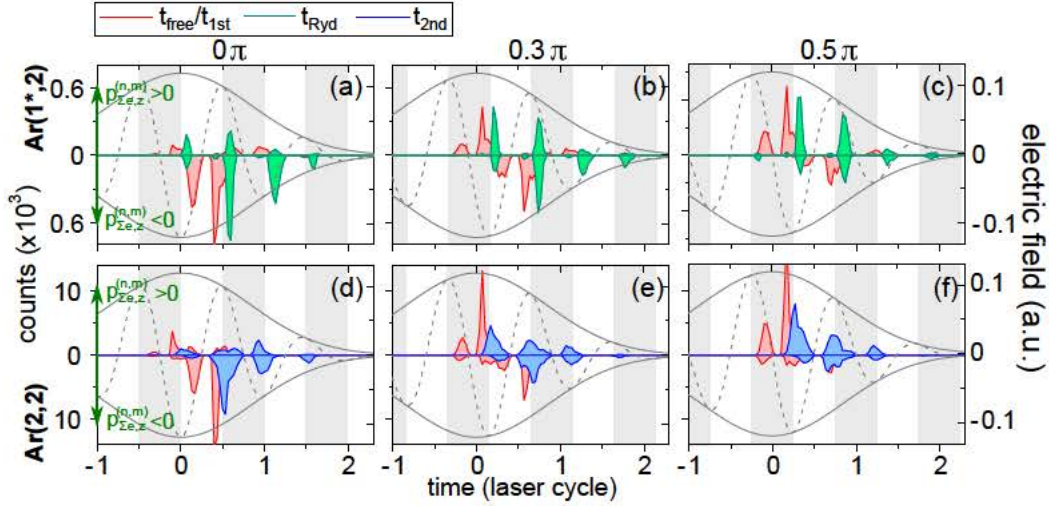
Figure 5.4.1: (a)-(c) Simulated electron emission time distributions in the Ar(1*,2) channel for CEP-values of 0π, 0.3π and 0.5π. (d)-(f) Same as upper row but for the Ar(2,2) channel. The emission times of the two electrons in the Ar(1*,2) channel (t_{free} and t_{Ryd}) and the two electrons in the Ar(2,2) channel (t_{1st}, t_{2nd}) are defined in Fig. 5.3.1 and in the text. The upper (lower) half in each figure shows the emission time distributions where the sum momentum of the two emitted electrons, $p_{\Sigma e,z}$, is positive (negative).

the other emission times. The instants for the Ar(1*,2) channel are marked in Figs. 5.3.1(a) and 5.3.1(b).

5.4 Discussion

5.4.1 Electron emission dynamics

The distributions of these decisive instants, separated for events with a positive or negative electron sum momentum along the laser polarization direction z, $p_{\Sigma e,z}$, are shown in Fig. 5.4.1 for CEP-values of 0π, 0.3π and 0.5π, respectively. For a first intuitive assessment of the simulated emission time distributions it seems helpful to compare them to distributions that would be expected if the ionic potential, in particular that of the neighboring ion, had no influence on the electron emission dynamics. In that case, the emission time distributions would be solely dictated by the shape of the laser electric

field respectively the laser vector potential. For a strong field such as the one used here, the electron emission rate $w(t_i)$ at any given instant of ionization t_i is, to first order, exponentially sensitive to the laser electric field strength, $w(t_i) \propto \exp(-\frac{2(2I_p)^{3/2}}{3|E(t_i)|})$ [187, 188], where $E(t) = |\mathbf{E}(t)|$ and I_p is the ionization potential of the considered bound state. The momentum of an electron emitted at time t_i after the laser pulse is given by (in atomic units) $\mathbf{p}_e = -\mathbf{A}(t_i)$ [19, 37]. The gray shaded areas in Fig. 5.4.1 indicate the time windows where the laser vector potential $\mathbf{A}(t) = -\int_{-\infty}^{t} \mathbf{E}(t')dt'$ is negative, $\mathbf{A}(t) < 0$, whereas the white areas correspond to times where $\mathbf{A}(t) > 0$. Consequently, electrons emitted by field-ionization within the gray (white) time windows should exhibit $p_{e,z} > 0$ ($p_{e,z} < 0$) and their emission rate should peak at the peaks of the laser electric field. Indeed, the red-colored distributions of t_{free} [channel Ar(1*,2) in Figs. 5.4.1(a-c)] and t_{1st} [channel Ar(2,2) in Figs. 5.4.1(d-f)] roughly follow this simple picture. However, on closer inspection, the distributions also markedly deviate from that expected for purely field-driven electron dynamics: The negative and positive areas are not equally distributed within a laser half cycle, they feature irregular shapes, and there also exist small peaks in between the main peaks. Thus, the binding potential of the dimer obviously crucially influences the trajectories of the emitted electrons.

To elucidate the details of the influence of the dimer potential on the electron emission dynamics and to understand the shapes of the t_{free} and t_{1st} distributions, an in-depth statistical trajectory analysis for the Ar(1*,2) channel was performed. A similar analysis was done for the Ar(2,2) channel in chapter 4. The results of the analysis for the Ar(1*,2) channel are summarized in Fig. 5.4.2. The green data points in this figure correspond to the recaptured trajectories and will be discussed below. For now we are only concerned with the red data points that correspond to the red-shaded t_{free} distributions of the trajectories that become free after the laser pulse, shown in the upper row of Fig. 5.4.1. Fig. 5.4.2(a) depicts for these trajectories the distribution of their minimum distance, D_{min}, to the neighboring argon ion. Two peaks can be noticed, one centered at a very small distance of $D_{\text{min}} \approx 0.5$ a.u., and another

one at a much larger value of $D_{\min} \approx 6$ a.u. The latter peak corresponds to trajectories that keep a relatively large distance to the neighboring argon ion on their way to the detector and do not interact with the neighboring ion, such as the red trajectory displayed in Fig. 5.3.1. The trajectories that form the peak at small $D_{\min}$, in contrast, on their way to the detector transit the Coulomb potential well of the neighboring argon ion and may or may not become transiently trapped by it.

As can be seen from Fig. 5.4.2(b) that plots the distribution of the time span Δt that these transiting electrons spend in close proximity ($D < 3.6$ a.u) to the neighboring ion, a bit less than half of the trajectories pass by the Coulomb potential very quickly ($\Delta t < 0.15$ laser cycles). We find that a large portion of them makes one roundtrip around the ion and then escapes. The other roughly half of the trajectories become transiently trapped by the Coulomb potential for on average about 0.4 laser cycles and are emitted only during the next laser half cycle around the peak of the field. Thus, we find that a substantial fraction of the trajectories in the peak $D_{\min} < 2$ a.u in Fig. 5.4.2(a) undergo the LITE process, in which an electron is transferred by a strong laser field across system boundaries, in the present case from one argon ion to the other, where it becomes transiently captured by the Coulomb potential of the distant entity. This means that the non-recaptured electrons in the Ar(1*,2) channel behave very similar to the first emitted electrons in the Ar(2,2) channel. Also for those electrons, we found in chapter 4, that their majority is emitted by field-ionization and a fraction undergoes the LITE process before emission. This explains the similarity of the t_{free} and t_{1st} distributions in Fig. 5.4.1. Because the emission direction of trajectories that become transiently trapped is strongly determined by the ion's Coulomb field and is not directly related to the sign of the laser vector potential at the time of emission, it are these trajectories that cause the deviations of the t_{free} and t_{1st} distributions in Fig. 5.4.1 from a pattern that would be expected if the dimer's binding potential had no influence on the emitted electrons. In addition, also the directly emitted trajectories that circle around the neighboring ion, such as the red example trajectory in Fig. 5.3.1, lead
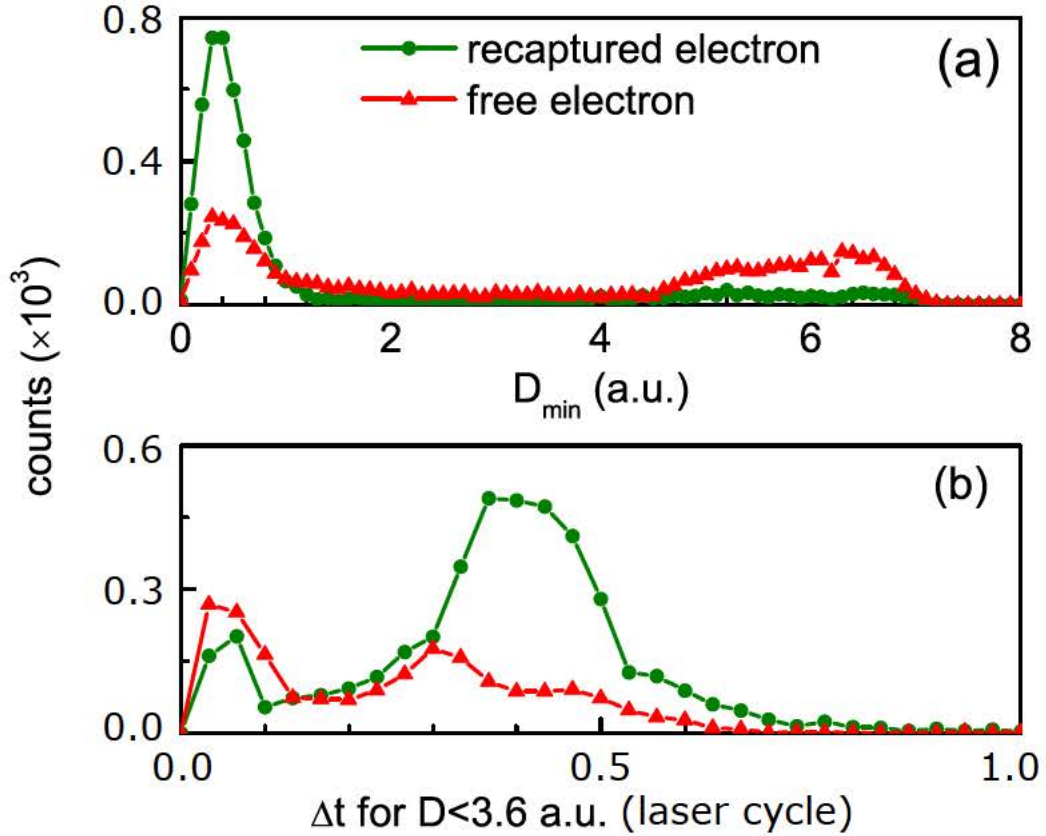
Figure 5.4.2: (a) Distributions of the minimum distance D_{min} to the neighboring ion of each trajectory emitted in the Ar(1*,2) channel for $\varphi_{CEP} = 0$. The distributions are separated into recaptured (green) and not recaptured trajectories (red). (b) The distributions of the time intervals Δt that the trajectories from (a) stay in a small region $D < 3.6$ a.u. around the neighboring ion.

to the deviations of the t_{free} and t_{1st} distributions from regular double peak structures. All in all this explains their shapes in Fig. 5.4.1.

Now we turn to the distributions of the instants t_{Ryd}, green colored in Figs. 5.4.1(a)-(c). These are the emission instants of the trajectories that undergo FFI and become recaptured in Rydberg states after the laser pulse. Their green D_{min} distribution in Fig. 5.4.2(a) shows that the absolute majority of all recaptured trajectories approach the neighboring argon ion very closely. And the corresponding Δt distribution in Fig. 5.4.2(b) shows that from these trajectories again the absolute majority becomes transiently trapped

in the Coulomb field of the neighboring argon ion for about 0.4 laser cycles and, thus, are emitted only during the next laser half cycle. That is, we find that almost all of the recaptured trajectories undergo the LITE process before their emission and subsequent recapture to a Rydberg state.

Thus, it seems that the LITE mechanism and the transient trapping on the neighboring ion following this process, leads to a higher chance for FFI. Even though this speculation cannot be substantiated with the acquired data, a plausible reason for this behavior could be that the delay in emission of the transiently trapped trajectories after LITE causes that these trajectories are emitted into the field only when the laser pulse already starts to fade. As a consequence, these trajectories are not driven away from the argon dimer very far and also do not reach very high kinetic energy. Therefore, their recapture probability might be enhanced as compared to trajectories emitted earlier at higher field strength. The green-colored recaptured trajectory in Fig. 5.3.1 exemplifies this behavior.

As was shown in chapter 4, also almost all of the second emitted electrons in the Ar(2,2) channel undergo the LITE process before emission. This is reflected in the $t_{2\text{nd}}$ distributions in Figs. 5.4.1(d)-(f), as the emission direction of the corresponding trajectories does not consistently follow the laser vector potential because of the strong influence of the ionic Coulomb potential on the transiently trapped trajectories, as mentioned above. Also, the $t_{2\text{nd}}$ distributions peak close to the field maxima, which reflects the fact that the transiently trapped trajectories are relatively weakly bound. However, even though both the recaptured trajectories in the Ar(1*,2) channel and the second emitted electrons in the Ar(2,2) channel are subject to LITE before emission, the t_{Ryd} emission distributions are markedly narrower than the $t_{2\text{nd}}$ distributions and also feature a small but significant time delay with respect to the laser field maxima. The origin and consequences of these differences will be the content of the following section.

5.4.2 CEP-dependence of $\mathcal{A}_z$ and CEP-shift between Ar(1*,2) and Ar(2,2) channels

With the help of the emission time distributions in Fig. 5.4.1 the measured CEP-dependence of $\mathcal{A}_z$, shown in Fig. 5.2.1(b), can be elucidated. The measured $\mathcal{A}_z$ over CEP of the Ar(2,2) and Ar(1*,2) channels are separated by only about 0.1π and thus exhibit similar CEP-dependence. They show both negative extremal values for small values of the CEP around $\varphi_{\text{CEP}} = 0\pi$, and increase with increasing CEP to positive maxima around $\varphi_{\text{CEP}} = 0.8\pi$. The emission time distributions in Fig. 5.4.1 explain this trend: As the CEP increases, all distributions change from being dominated by peaks pointing into $p_{\Sigma e,z} < 0$ ($\mathcal{A}_z < 0$) at $\varphi_{\text{CEP}} = 0\pi$, via roughly balanced distributions ($\mathcal{A}_z \approx 0$) at $\varphi_{\text{CEP}} = 0.3\pi$, to being dominated by distributions pointing into $p_{\Sigma e,z} > 0$ ($\mathcal{A}_z > 0$) at $\varphi_{\text{CEP}} = 0.5\pi$. Thus, the measured large-scale CEP-dependence of electron emission that is similar for the Ar(2,2) and Ar(1*,2) channels (except for their small offset of about 0.1π), although partly determined by complex electron transfer and transient recapture processes, can be precisely understood based on the sub-cycle ionization timing revealed through the simulations.

To explain the small CEP-shift between the Ar(2,2) and Ar(1*,2) channels it is, however, not sufficient to only regard the overall, integrated positive or negative directionality of the electron emission peaks. In order to understand the CEP-shift it is necessary, as will be shown, to also consider the precise positions and even the shapes of the emission peaks. The shapes and positions of the t_{1st} and t_{free} distributions in the Ar(2,2) respectively Ar(1*,2) channels are quite similar, see Fig. 5.4.1. Thus, they alone cannot account for the observed CEP shift between these two channels. More prominent differences, though, can be noticed between the emission distributions of the other electrons released in each channel, i.e., between the t_{Ryd} and t_{2nd} distributions.

As can be clearly seen, the t_{Ryd} distributions of the recaptured electrons in the Ar(1*,2) channel are much narrower than the t_{2nd} distributions in the

Ar(2,2) channel. This is due to the fact that the recapture of the electron in a Rydberg state requires that it returns to the nucleus with almost zero momentum. When the force due to the laser electric field dominates the electron motion, this imposes onto the electron the requirement that it is emitted within a narrow time-range around the maxima of the electric field. This can be understood from the relation $\mathbf{p}_e = -\mathbf{A}(t_i)$. To reach negligible momentum $|\mathbf{p}_e| \approx 0$ upon conclusion of the laser pulse this relation dictates that the electron emission times $t_i = t_{\mathrm{Ryd}}$ are confined to narrow ranges around the zeros of the laser vector potential $\mathbf{A}(t)$ or, equivalently, the maxima of the laser electric field $\mathbf{E}(t)$. In reality, the influence of the ionic Coulomb field leads to a small shift of the narrow emission time distributions away from the field's maxima [45, 189]. Both, the narrow shape and small shift are clearly visible in the t_{Ryd} distributions in Fig. 5.4.1.

In comparison with the t_{Ryd} distributions, the t_{2nd} distributions in the Ar(2,2) channel are significantly broader. That is because in contrast to the emission of the recaptured electrons, this ionization step is subject to no specific timing constraints. As a result, the emissions of these transiently captured (due to LITE, as explained above) and therefore relatively weakly bound trajectories take place dominantly by field ionization. Thus, the corresponding emission time distributions peak close to the field maxima, cf. Figs. 5.4.1(d)-(f).

As shown in Fig. 5.2.1, the sign of the CEP-shift is such that at any given value of φ_{CEP} within the range $\varphi_{\mathrm{CEP}} = [0, 0.8\pi]$ the $\mathcal{A}_z$-value of the Ar(2,2) channel is always more positive than that of the Ar(1*,2) channel. The opposite is true for $\varphi_{\mathrm{CEP}} = [0.9\pi, 1.7\pi]$. Thus, in the CEP-range $\varphi_{\mathrm{CEP}} = [0, 0.8\pi]$ that is covered by the three values 0, 0.3π and 0.5π depicted in Fig. 5.4.1, the mean sum momentum of the emitted electrons along z, $p_{\Sigma e,z}$, must always be more positive for the Ar(2,2) channel than for the Ar(1*,2) channel. Obviously, the broader shape of the t_{2nd} distributions in combination with the small Coulomb-induced delay to the laser field-maxima of the much narrower t_{Ryd} distributions cause that overall the second emitted electrons in the Ar(2,2) channel have a slightly higher chance to be emitted at instants that favor a positive electron momentum than the recaptured electron in the
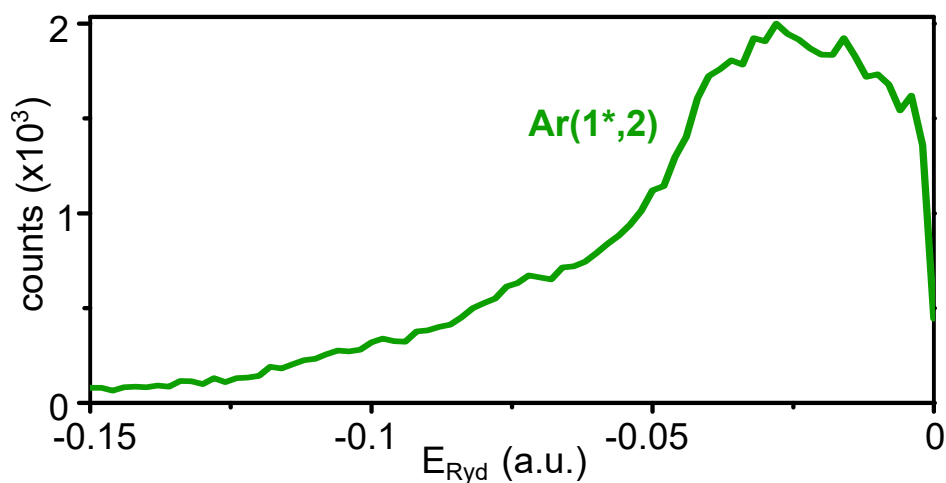
Figure 5.4.3: Simulated energy distribution of the recaptured trajectories in the Ar(1*,2) channel at the end of the simulation time long after the laser pulse.

Ar(1*,2) channel, which explains the small relative CEP-shift between the $\mathcal{A}_z$ curves of the Ar(1*,2) and Ar(2,2) channels.

5.4.3 Electron recapture and localization

This study of the origins of the CEP-dependent electron emission in the Ar(1*,2) channel has revealed unprecedented insight into the electron recapture dynamics on sub-cycle times. As was shown, of the two emitted electrons in this channel, it is the recaptured rather than the directly emitted one that is transiently transferred across the system boundary to the other argon ion. Paired with the mere fact that the recapture process is amenable to the shape of the laser field at all, this raises hopes for the possibility to implement laser field control of molecular reactions initiated by strong field-driven donor-acceptor electron transfer processes. In the following we will discuss to what extent the presented implementation comes close to this vision, and how future work could mitigate certain shortcomings of this approach.

One of the two key processes investigated by this study is the electron recapture process through FFI, which results in a highly excited argon ion after the laser pulse. In molecules, the population of a (highly) excited electronic

state is an important mechanism for inducing molecular reactions such as dissociation. The outcome of such reactions crucially depends on the energy of the populated excited state. The simulations reveal that in the experiment mostly loosely bound Rydberg states with a mean binding energy of 0.025 a.u., which corresponds to a principal quantum number of $n \approx 8$, are populated, see Fig. 5.4.3. This is in good agreement with previous experimental and theoretical studies on the atomic [43, 45–48] as well as the argon dimer case [49].

The population of a weakly bound Rydberg state can open up a number of molecular reactions, including dissociation, fragmentation and the generation of radicals [53–55, 59, 60]. However, in quantum control it is preferred that a specific reaction is triggered, which usually means that more strongly bound electronic states should be populated [42, 190–193]. However, as in FFI a slow electron is recaptured by an ion's Coulomb potential, this process by its nature prefers weakly bound states. Nevertheless, in Ref. [46] it was shown that states down to $n = 5$ are populated by FFI. Such states are highly relevant for molecular dissociation reactions [54, 55, 59].

Yet, FFI leads to the population of bound states with a broad energy spectrum. It is, thus, important to harness the FFI process such that preferentially more strongly bound states with a narrower spectrum are populated. One possibility for this seem to be two-dimensional laser waveforms composed of two colors, e.g., OTC fields [194–196] or counter-rotating circular two-color fields [123, 197, 198]. With such waveforms not only the emission and recollision timing of recaptured electrons can be controlled, as in the present work using the CEP of few-cycle pulses, but also the trajectory of the recolliding electron within the laser polarization plane. It was previously shown that for Rydberg electrons the use of OTC fields opens up control over the properties of their Kepler orbits such as their angular momentum, direction and shape [47]. It seems, therefore, possible that carefully designed two-dimensional waveforms can also be used to influence the energy spectrum of recaptured electrons.

The second key process investigated in the present chapter is the electron
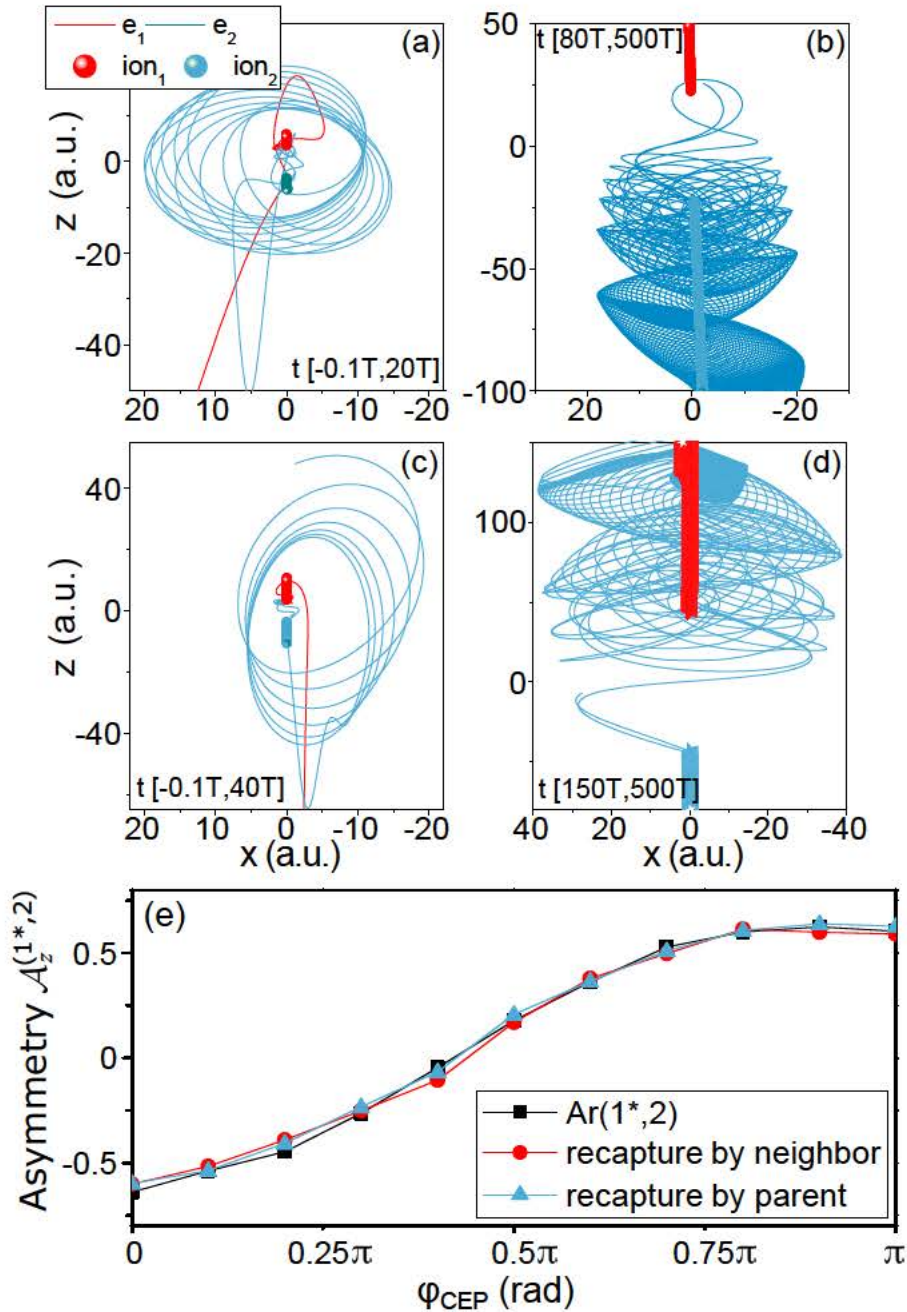
Figure 5.4.4: (a,b) Example of a simulated electron trajectory in the Ar(1*,2) channel where the trajectory is recaptured by its own parent ion, shown for times during the laser pulse (a) and over a longer period long after the laser pulse (b). (c,d) Same as (a,b) but for a case where the trajectory localizes at the neighboring argon ion after the laser pulse. (e) Electron emission asymmetry, $\mathcal{A}_z$, over CEP for the trajectories in (a,b), shown in blue, in comparison with the same quantity for the trajectories in (c,d), shown in red, and all recaptured trajectories in the Ar(1*,2) channel (black).

transfer through the LITE mechanism. It was shown above that almost all of the recaptured electrons first undergo this transfer process to the neighboring argon ion where they become transiently trapped and are emitted by field-ionization only up to almost a laser half cycle later. To understand whether this transfer and transient trapping step influences the recapture location, all computed electron trajectories were divided into events where the Rydberg electron has localized at its parent ion or the neighboring ion after the two ions have become well separated at the end of the simulation run. An example trajectory that visualizes the recapture of the electron at its parent ion during fragmentation of the argon dimer into two Ar^{2+} ions is depicted in Figs. 5.4.4(a) and (b). The other case, recapture on the neighboring ion, is visualized in Figs. 5.4.4(c) and (d). The left figure panels [Figs. 5.4.4(a) and (c)] show the trajectories during and shortly after the laser pulse, the right panels [Fig. 5.4.4(b) and (d)] long after the laser pulse.

It can be seen that upon conclusion of the pulse the electron is in both cases already recaptured in a Rydberg orbit. Because the two argon ions are moving much slower than the electrons, at that time their distance is still small (close to the R_{eq}) and the Rydberg orbit cannot be assigned to either of the two argon nuclei. Only much later, as the distance of the two argon ions increases due to Coulomb explosion, the electron finally localizes at either of the two [Figs. 5.4.4(b) and (d)]. Thus the localization process is temporally well separated from both the recapture process and the transfer process through LITE. Furthermore, the simulations reveal that both cases, recapture on the parent ion or on the neighboring ion, take place almost equally likely. That means, in the experiment the localization of the Rydberg electron is a statistical process. This is understandable since for a symmetric dimer with two ions of the same charge state both ions exert the same attractive force on the electron that orbits around both ions. The situation is different for dimers where the two ions exhibit different charge states. In that case the electron localizes more likely on the ion with the higher charge due to its higher attractive force [146, 183]. Therefore, it will be interesting to investigate the sub-cycle electron dynamics leading to electron recapture

and its dependence on the shape of the laser field in asymmetric channels, particularly for molecular dimers, where each of the molecules can also dissociate.

Because the Rydberg electron localization takes place long after the laser pulse, also the CEP of the laser pulses is irrelevant for the localization process. This is confirmed by Fig. 5.4.4(e) which depicts $\mathcal{A}_z$ as a function of the CEP separated into the events where the recaptured electron localizes on its parent argon ion and the neighboring ion. Both curves agree with each other and with the combined $\mathcal{A}_z$ curve reproduced from Fig. 5.2.1(c), confirming the independence of the localization process from the CEP. As a consequence, we can conclude that the measured CEP-dependence of the parameter $\mathcal{A}_z$ in the Ar(1*,2) channel shown in Fig. 5.2.1(b) is entirely due to electron emission by field-ionization, the electron transfer by LITE and the recapture process due to FFI but not due to the Rydberg electron localization on the ions. Influence of the localization process by the laser field shape might be possible with the two-dimensional waveforms mentioned above. This is motivated by the fact that they can determine the properties of the Rydberg orbits [47] and therewith cause some preponderance for localization on one of the two ions in the dimer. Additionally, a narrower and deeper lying energy spectrum of the recaptured electron that might be possible with these laser waveforms would also be beneficial for control over the localization process.

5.5   Conclusion

In conclusion, in this chapter, electron recapture processes in argon dimers driven by intense few-cycle laser pulses with a known CEP were investigated. The main motivation was to obtain insight into the sub-cycle laser field-driven electron dynamics that underlie the electron recapture process responsible for the FFI. To this end, the CEP-dependence of the mean electron sum momentum of all emitted electrons in two ionization-fragmentation channels, Ar(1*,2) and Ar(2,2), were compared. In both channels two electrons are emitted from each argon ion, but in the Ar(1*,2) channel one of them is

recaptured by the Coulomb potential of the argon ions.

In the experiments a distinct CEP-dependence of the electron emission asymmetry for both channels, and a small relative CEP-shift between the two channels was found. With the help of a classical ensemble trajectory model it was explained that almost all of the later recaptured electron trajectories in the Ar(1*,2) channel are initially transferred to the neighboring argon ion by the LITE-process where they are transiently captured. Subsequently, after up to roughly half a laser cycle, they are emitted by field-ionization and finally, upon conclusion of the laser pulse, they are recaptured in a Rydberg state. Thus, the electron emission step is very similar to the Ar(2,2) channel for which a similar emission behavior was found in chapter 4. The small relative CEP-shift between the channels arises through a subtle difference in the emission timing caused by the momentum restrictions of the recaptured electrons which dictate that these electrons, in contrast to the non-recaptured electrons, exhibit near-zero momentum upon conclusion of the laser pulse.

The CEP-dependence of the electron transfer process that was identified as a key step in the population of highly excited states in the Ar(1*,2) channel could indicate that laser field control of molecular reactions on a distant entity initiated by strong field-driven donor-acceptor electron transfer processes might become possible. The simulations show that the electron is recaptured to Rydberg states with a mean principal quantum number $n \approx 8$. Its orbit surrounds both ions in the argon dimer. Upon the slow separation of the two argon ions due to the repulsive Coulomb force, which takes place mainly after the pulse, the electron statistically localizes on one of the two ions with roughly equal probability. Thus, control over the sub-cycle electron emission timing and the recapture process, as demonstrated here using the CEP of few-cycle pulses, is not sufficient to also determine the electron localization necessary to determine a reaction on the distant entity. Such localization control may, however, be possible using two-dimensional laser waveforms, e.g., with orthogonal two-color fields [194–196], for which it was shown previously that they can influence the shape, direction and angular momentum of the Rydberg orbits populated by the electron recapture process [47].

"Give a man a fire and he is warm for a day, but set fire to him and he is warm for the rest of his life."

— Sir Terry Pratchett, *Jingo*

Chapter 6

HHG at the Carbon K-edge directly driven by SRS red-shifted pulses from an Yb amplifier

In this chapter, a new approach to drive high-order harmonic generation (HHG) in gases with pulses from an Yb:CaF$_2$ amplifier post-compressed and red-shifted by stimulated Raman scattering (SRS) in a nitrogen-filled stretched hollow core fiber (HCF) is presented. This driving scheme is operating in the low-efficiency window of parametric amplifiers at 1100-1300 nm, which is suitable for optimizing HHG flux in the specific 200-300 eV region of interest. The extension of the cut-off energy of HHG up to the carbon K-edge without the need for laser frequency conversion via parametric processes is experimentally demonstrated. Due to the combination of energy scalability of low quantum defect ytterbium based laser system with the high conversion efficiency (up to 80 %) of the SRS technique, significant increase of generated photon flux is expected in comparison with established platforms for HHG in the water window. A comparison between HHG driven by the SRS scheme and the conventional self phase modulation (SPM) scheme is shown.

111

6.1 Motivation

HHG in gases, driven by NIR femtosecond laser pulses, has been widely used for time-resolved investigations of ultrafast electronic and molecular dynamics with a variety of techniques. More recently, the generation of soft X-ray pulses in the water-window spectral region [199, 200] has been used for time-resolved investigations of molecular dynamics by transient absorption at the near edge (K or L edge) of the constituting elements of organic molecules in gas [201] or liquid phase [202]. The transparency of water in this spectral region also enables observation of molecules in aqueous solution [203], often the most natural environment of biochemical compounds. Also, because absorption edges of several key elements (K-edges of carbon at 284 eV, nitrogen at 410 eV and oxygen at 540 eV) of organic and biochemical important molecules are situated in the water window it is particularly interesting for near-edge x-ray absorption fine structure (NEXAFS) based techniques [201, 204, 205]. Among the elements that exhibit absorption edges in the water window especially carbon provides the core structure for organic chemistry and therefore a vast research target, due to its ability to form a variety of stable bonds (single, double, triple and structures with de-localized electrons) with many elements, including itself. To give a few examples, the elemental specificity and chemical sensitivity of NEXAFS enabled the time resolved observation of ultrafast ring-opening [206, 207], intersystem crossing [208] and bond dissociation [209, 210].

In general, HHG is achieved by focusing intense, NIR, femtosecond laser pulses in a noble gas, where the the strongly non-linear light-matter interaction results in the emission of light at much higher frequencies (XUV or soft X-ray) as compared to the one of the driver (NIR). This process is well understood both at the microscopic level of the single atom response [17, 32] and at the macroscopic level through the phase matching conditions [67] (see also section 2.5). The generated spectrum features a broadband plateau which quickly drops at the so-called cut-off energy. When targeting HHG in a specific spectral region, the main scaling laws to be taken into account are the dependence of the cut-off energy $E_{cut-off} \propto I\lambda^2$ [17, 32] and of the

harmonic photon flux $\Phi \propto \lambda^{-5} - \lambda^{-6}$ [63, 64] on the driver wavelength. These two opposing wavelength dependencies define the range of the optimal NIR driver wavelengths so that the generated harmonics cover the targeted spectral region and the photon flux therein is not excessively diminished. In other words, the highest HHG conversion efficiency is achieved for the shortest NIR wavelength that can drive a certain XUV cut-off energy. In this work it is verified that, in agreement with [211], the maximum cut-off energy by driving HHG in helium at 1030 nm is about 220 eV. As shown in table 6.1.1, several works show cut-off energies of 300 eV with a driver wavelength of 1300 nm [205, 206, 212]. Thus, in the specific case of HHG targeting the 220-300 eV range (covering, among others, the sulfur L-edge and the carbon K-edge), the optimal driving wavelength would be in the 1100-1300 nm range.

Given the intrinsic extremely low conversion efficiency from the NIR driver into the soft X-ray spectral region via HHG in gases, the main limitation of this technique lies in the difficulty to increase the photon flux. Such an increase would be extremely beneficial, as it would allow to study more complex molecular samples, the quantitative determination of the branching ratios in the transient products of the reaction as well as the study of molecular dynamics for samples in liquid solutions rather than in gas phase which - for most sample - is quite an artificial environment.

An ideal driver for HHG should deliver energetic (several mJ), short (tens of fs) pulses, with tunable wavelength in the NIR and at high repetition rate (kHz). The requirements of high peak power pulses and high repetition rate narrow down the pool of possible laser sources to Ti:Sa (800 nm, 20-50 fs) and ytterbium based amplifiers (1030 nm, 200 fs). However, to achieve cut-off energies beyond 220 eV, in both cases an intermediate step is necessary for converting the laser fundamental into a longer wavelength for the HHG driver.

A typical way to obtain tunable few-mJ pulses with duration of several tens of fs is by optical parametric amplification (OPA). The conversion efficiency and spectral bandwidth of OPA is limited by the properties of nonlinear crystals, such as nonlinear coefficient d_{eff}, group velocity mismatch between

Table 6.1.1: Comparison of laser systems capable of driving HHG in the water window spectral region [204, 206, 212–222] with recent approaches using SRS based red-shift and post-compression [223, 224] and this work. References marked with * also include the successful application to absorption spectroscopy. The colors distinguish the different gases used for HHG and highlight the driving wavelength that are most efficient for targeting the carbon K-edge in green.

HHG Cutoff [eV]	gas	System	Wavelength [um]	Pulse duration [fs]	Rep. Rate [Hz]	Pulse Energy [mJ]	Power [mW]	Ref.
330	He	Ti:Sa +OP(CP)A	1,30	35	10	5,50	55	[212]
300	He		1,32	50	1000	2,80	2800	[206]*
400	Ne		1,50	50	1000	1,60	1600	[213]
270	Ne		1,55	45	10	100,00	1000	[214]*
340	He							
320	Ne		1,60	9	1000	0,55	550	[215]
300	Ne		1,60	35	10	2,20	22	[216]
450	He					4,50	45	
350	Ne		1,80	50	1000	2,50	2500	[204]*
375	Ne		1,80	8	1000	0,70	700	[217]*
390	Ne		1,85	12	1000	0,40	400	[218]
350	Ne		1,85	12	1000	0,40	400	[219]
500	He							
395	Ne		2,00	40	10	2,40	24	[220]
530	He							
450	Ne	Yb+OPCPA	2,10	32	1000	1,35	1350	[221]
1600	He		3,90	80	20	10,00	200	[222]
80	Ar	Yb+SRS	1,20	<10	50000	0,245	12250	[223]
80	Ar	Ti:Sa +SRS	0,940	10,8	100	2,42	242	[224]
165	Ne	Yb+SPM	1,03	18,5	500	9,00	4500	This Work
220	He		1,03	18,5	500	9,00	4500	
200	Ne	Yb+SRS	1,23	22,0	500	8,00	4000	
290	He		1,23	22,0	500	8,00	4000	

the interacting pulses, crystal length, and optical damage threshold [225–227]. At moderate pump energies of several mJ the conversion efficiency of pump to both signal and idler waves combined, when close to the doubled pump wavelength, can be as high as 50 % [228]. However it drops fast with detuning from this degeneracy point. Following Manle-Rowe relations [226], typical conversion efficiency of ~10 - 25 % and 2 - 10 % can be achieved solely in signal and idler pulses correspondingly. Working at the high conversion efficiency regime and therefore at high intensities, leads to degradation of the beam due to a parametric back conversion at the center of the beam and might affect the pulse quality. Keeping a high beam fidelity and scaling to higher energies requires to lower the intensity and increase the size of the beam. Often, this energy scaling is restricted by available crystal apertures, their spatial homogeneity, onset of small-scale self-focusing and subsequent nucleation of the beam. However, it is still possible by using optical parametric chirped pulse amplification (OPCPA) approach [229, 230]. OPCPA systems allow to generate ultrashort pulses with tens of mJ energies, however require complex dispersion management and therefore are limited in wavelength-tunability.

An alternative is the recently demonstrated possibility by SRS to induce an asymmetric spectral broadening towards the longer wavelengths in laser pulses from both Ti:Sa and ytterbium based lasers by propagation in a long, stretched, HCF filled with molecular gases. Here, the new spectral components at longer wavelengths can contain more than 80% of the pulse energy [99, 223, 224]. This effect can be seen as a spectral broadening combined with moderate red-shift, and it is indeed suitable for the generation of compressed pulses as in the case of SPM, but red-shifted in the vicinity of the laser wavelength. See also sections 2.7 and 3.2.2 for more information about Raman scattering and its application for laser pulse preparation.

Figure 6.1.1 shows a schematic concept of the approach to increase the achievable photon flux Φ at the carbon K-edge by tackling this task from each of the three steps involved: the efficiency of conversion of the HHG process, the efficiency of conversion from the laser fundamental into the driver wavelength,
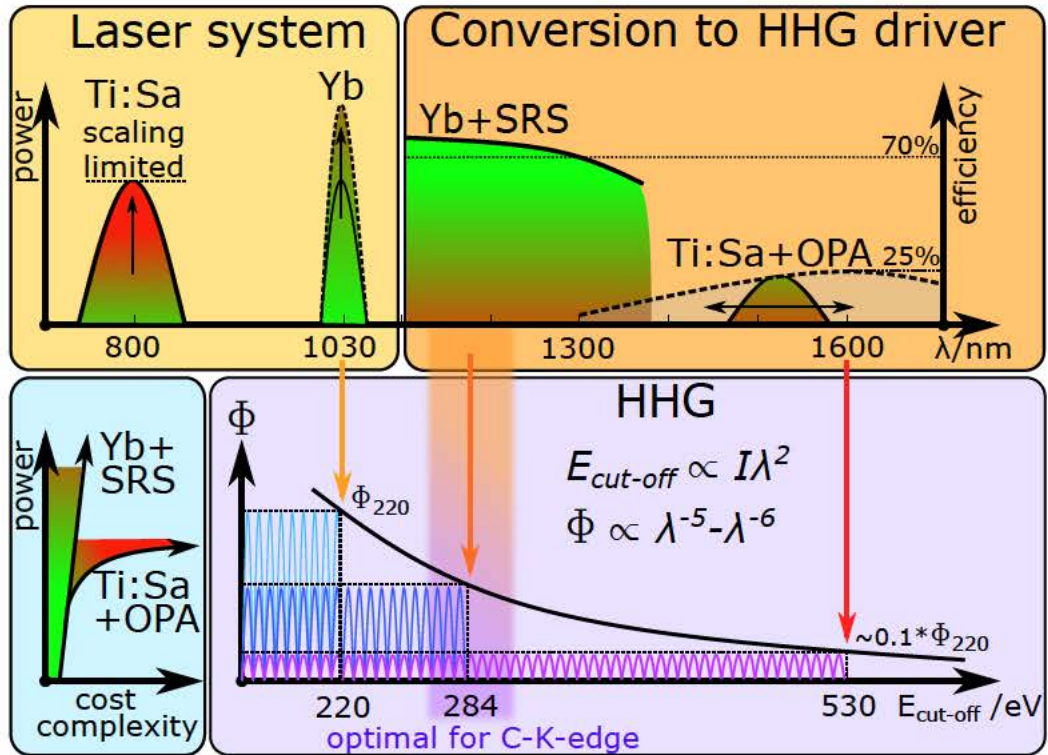
Figure 6.1.1: Schematic concept of the approach to increase the photon flux Φ at the carbon K-edge: The efficient power scalability of ytterbium laser systems is employed in combination with the high conversion efficiency of the SRS technique to produce high power driving laser pulses in the optimal wavelength range for HHG at the carbon K-edge. The bottom left plot shows a schematic of power scaling versus cost and complexity for the two systems. And the bottom right plot shows the dependence between achievable cut-off energy $E_{cut-off}$ and photon flux Φ as determined by the scaling laws of HHG for the driving laser wavelengths λ given by the upper plot. The values for $E_{cut-off}$ are estimates based on the $220\,\text{eV}$ cut-off energy achieved by direct driving with the $Yb:CaF_2$ laser system at $1030\,\text{nm}$.

and the power scaling of the laser source.

The efficiency of conversion of the HHG process is improved by properly choosing the optimal wavelength for the driver, i.e. the shortest one which still allows to cover the desired cut-off energy. Then the combination of laser system and wavelength conversion process can be determined that can access this optimal wavelength with the highest efficiency. A further increase of the flux in the soft X-ray spectrum can be achieved by the power scaling of the laser source. Following this concept, below it will be discussed that the proposed scheme of ytterbium laser system in combination with SRS based wavelength conversion represents the ideal platform for scaling the photon flux at the carbon K-edge.

Ti:Sa laser and OPA are well established and reliable technologies, which also means that their improvement in terms of power scaling and efficiency can be only incremental. In details, Ti:Sa amplifiers have been, till recently, pumped indirectly: typically, a diode laser at 808 nm pumps a Nd:YAG laser, which emits light at 1064 nm, which is subsequently frequency doubled to 532 nm to pump the Ti:Sa amplifier. In the perspective of power scaling, the efficiency, limitations and complexity of each of these steps must be accounted for. Even though nowadays Ti:Sa laser can be directly pumped by diodes in the blue (450 nm)[88] or green (520 nm)[89] wavelength range to produce laser pulses around 800 nm, their power scalability suffers fundamentally from the higher quantum defect when compared with ytterbium based laser systems that are directly diode pumped around 970 nm to deliver laser pulses at 1030 nm. Therefore, due to their smaller quantum defect, ytterbium based gain media represent the best option for power scalability of ultrashort laser pulses. On the other hand, their smaller gain bandwidth limits the directly achievable pulse duration, as compared to Ti:Sa. Given the possibility to post-compress the pulses from ytterbium amplifiers by SPM in a HCF to tens of fs or below [95], the longer wavelength is particularly advantageous when targeting HHG in the 100-200 eV region [211, 231], but insufficient to reach the carbon K-edge. For this, longer driving wavelengths are required, as can be provided by SRS in a HCF. It has been demonstrated that this SRS technique is suitable

also for driving HHG [223, 224], but these first investigations showed only the possibility to reach 80 eV when focusing the red-shifted and compressed pulses in argon.

Now, the advantage expected from SRS, but not confirmed prior to this work, is the possibility to efficiently extend the cut-off energy of generated harmonics due to the red-shift in the fundamental wavelength beyond the limits of pulses compressed by SPM. It will be shown, that the combination of Yb:CaF$_2$ laser with SRS in HCF allows us to extend the cut-off of HHG in helium from 220 to 290 eV, thus reaching the carbon K-edge, with an optimal driving wavelength without additional conversion losses and complexity from an OPA stage.

A comparison of several laser systems capable of driving HHG in the water window with recent attempts of driving HHG with pulses produced via SRS and this work is shown in table 6.1.1. Recently, considerable effort went into increasing the pulse energies in the water window spectral region [214]. Considering the requirements of pulse energy, repetition rate and pulse duration, the preferred platform for near edge transient absorption experiment has been Ti:Sa lasers in combination with OPA [199–201] and experiments so far relied on driving NIR wavelengths above 1300 nm. The choice of this driving wavelength is dictated by the range of efficient conversion of OPA rather than by the optimum for the HHG process. Of the shown platforms, only [206] and [212] employ a driver wavelength close to the optimal range for targeting the carbon K-edge due to the unfavorable efficiency of OPA systems towards the pump wavelength. Longer driving wavelength for HHG also covers the carbon K-edge, but for a given HHG gas at a reduced conversion efficiency [204, 213–222]. This work demonstrates the successful application of SRS red-shifted pulses as a driver to generate phase matched harmonics with a cut-off extended well beyond the limit of laser pulses at the un-shifted fundamental laser wavelength produced by SPM. Most importantly, it demonstrates the extension of the cut-off up to the carbon K-edge at 284 eV with HHG driven in helium.
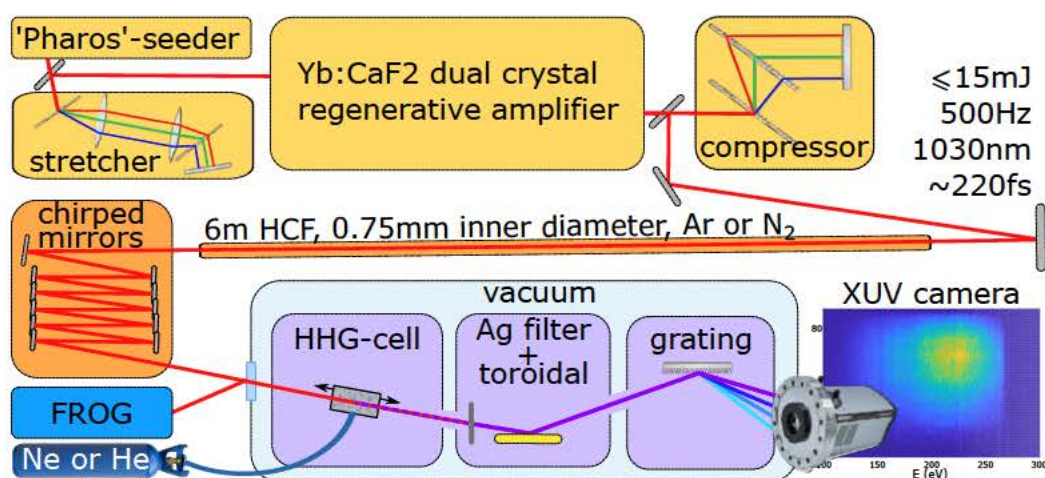
Figure 6.2.1: Schematic of the experimental setup, for details see the text. The output of the laser system (up to 15 mJ, 220 fs pulses with center wavelength 1030 nm) are spectrally broadened and red-shifted in a 6 m long HCF by SRS in nitrogen and afterwards compressed by a set of chirped mirrors. Then the pulses enter a vacuum system for HHG. The back-reflection of the entrance window to the vacuum system is used for SHG FROG measurement.

6.2 Experimental Setup

Figure 6.2.1 shows the experimental setup. The laser system uses a CPA scheme [91]. A "Pharos" femtosecond ytterbium laser (*Light Conversion*) is used as a seeder of sub-mJ pulses that are stretched in a Martinez-type stretcher to 500 ps. Stretched pulses are then amplified in a home-built Yb:CaF$_2$ cryogenically-cooled dual-crystal regenerative amplifier up to 15 mJ. The amplified pulses are then compressed in a Treacy-type compressor to sub 220 fs duration. The system operated at 500 Hz repetition rate, but can be tuned to repetition rates of up to 10 kHz. See also section 3.1.2.

The laser beam is then coupled into a long, stretched HCF (*Few-cycle Inc.*, 6 m length, 0.75 mm inner diameter), where the pulses are either spectrally broadened by SPM in argon or spectrally broadened and simultaneously red shifted by SRS in nitrogen. As discussed in the previous section, the wavelength scaling laws for photon flux and cut-off that govern HHG dictate an optimal wavelength when targeting a specific spectral region. For generating

harmonics in helium around and above the carbon K-shell absorption edge at 284 eV, based on the achieved cut-off when driving directly at 1030 nm and the scaling laws, we can estimate this central wavelength to be between 1200 nm and 1300 nm. To reach this desired wavelength, the recently reported technique of red-shifting and simultaneous spectral broadening enabled through SRS by propagation in a HCF filled with molecular gas was employed [99, 223, 224]. By adjusting the nitrogen gas pressure in the HCF the amount of red-shift $\Delta\omega$, which is proportional to the product of gas pressure (p) and laser intensity (I): $\Delta\omega \propto pI$, can be continuously tuned until it is limited by the pressure-dependent critical power of self focusing [100]. By this, the broadened spectrum reaches up to 1300 nm, with a center wavelength of 1230 nm.

Afterwards a set of chirped mirrors that support a bandwidth from 650 nm to 1350 nm (PC147 by *Ultrafast Innovations*) is used to compress the pulses to about 20 fs (see SHG FROG measurement in Fig. 6.2.2). See also section 3.2 for more details about pulse preparation by combination of SPM or SRS with chirped mirrors. Typically, by coupling 12.5 mJ pulses into the HCF with a nitrogen gas pressure of 500 mbar, output pulse energies of 8 mJ can be achieved.

The SHG FROG setup used in the experiments was designed for pulses in excess of 20 fs. Therefore, the pulse duration measurements, summarized in Fig. 6.2.2, might have overestimated the real pulse duration [103]. From the spectra transform limited pulse durations of about 15 fs can be derived.

The laser pulses then enter a vacuum system for HHG and are focused with a f=40 cm mirror into a movable gas cell of 14 mm length with a backing pressure of about 1 bar. The pulse energy can be finely tuned by closing an iris. The generated harmonic spectra shown in this chapter were acquired with 4.8 mJ pulses. The pressure in the gas cell is controlled with a variable flow valve. A 300 nm thin silver filter is used to suppress the fundamental NIR laser beam before the generated harmonics are re-focused by a golden coated toroidal mirror (f=120 cm) at 4° angle of grazing incidence on the entrance slit of a soft X-ray spectrometer (grating 001-0450 by *Hitachi* and
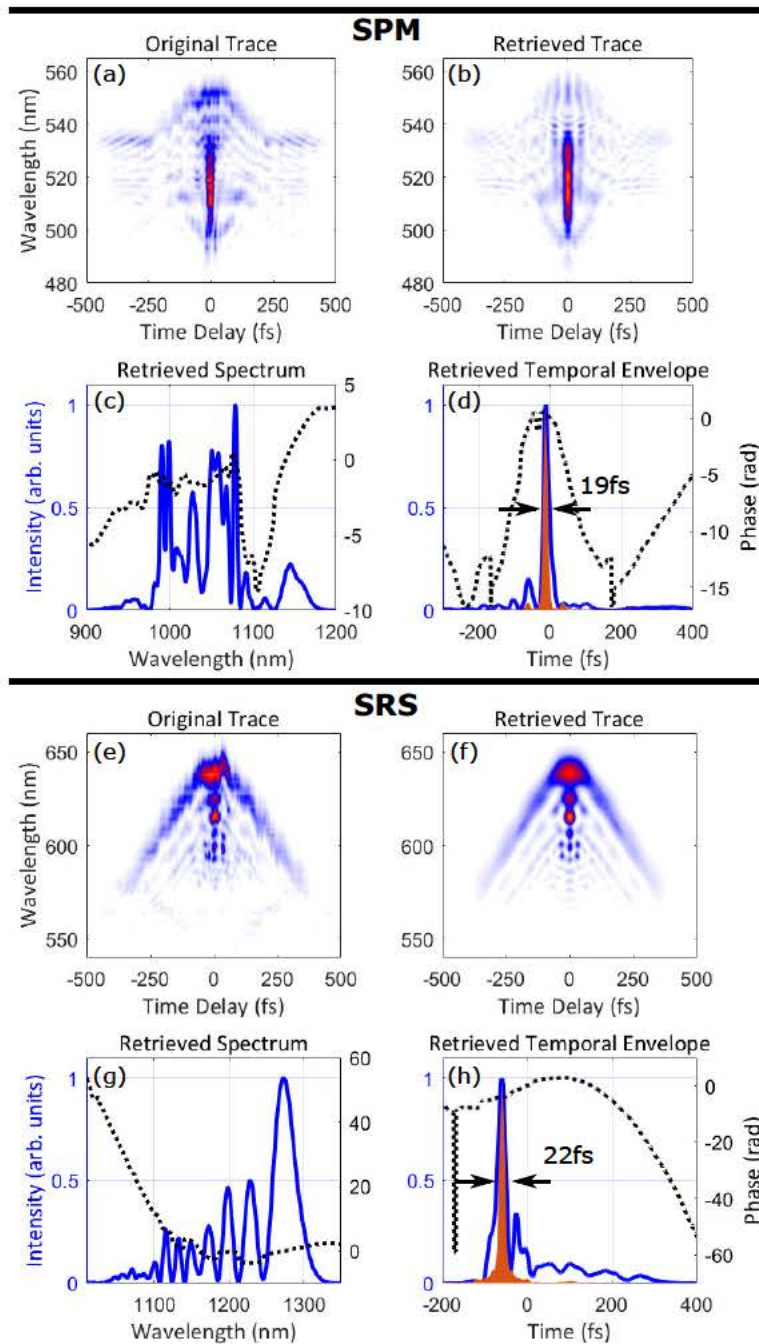
Figure 6.2.2: SHG FROG measurements of the laser pulses after SPM (top) and SRS (bottom) in the HCF and compression by chirped mirrors. Measured (a,e) and reconstructed (b,f) SHG FROG traces. Retrieved spectral (c,g) and temporal (d,h) envelope of pulses with temporal FWHM <19 fs (SPM) and <22 fs (SRS) used for HHG. Shown as orange areas in (d) and (h) are calculated transform limited pulses with duration of 15 fs and 14.7 fs respectively.
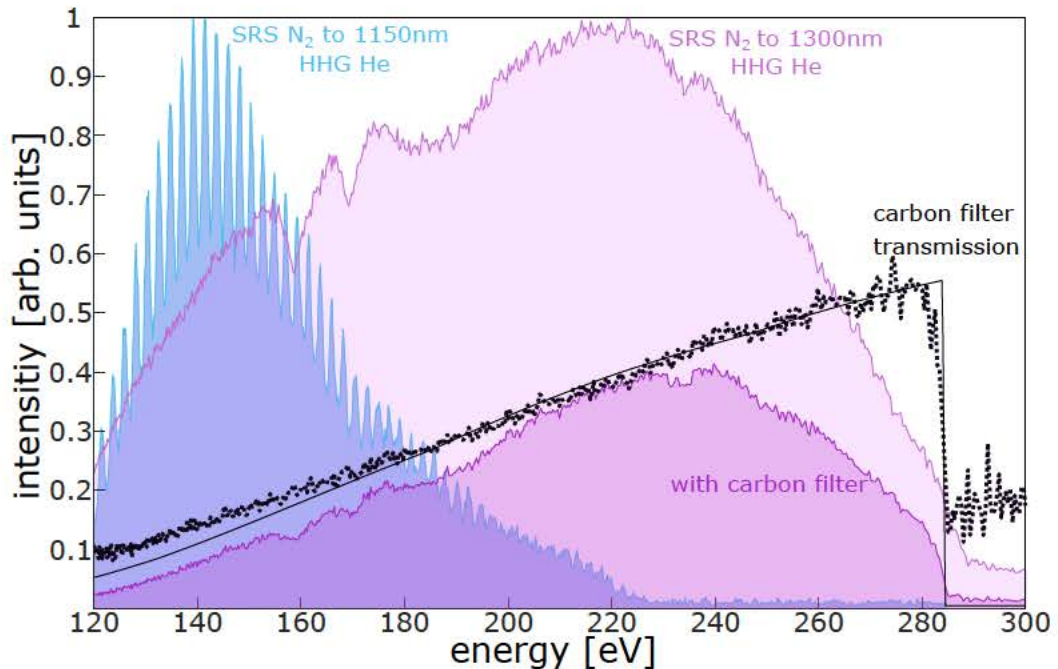
Figure 6.3.1: Shown in blue is the spectrum with harmonic structure that is generated when the driving laser spectrum is extended by SRS only up to the limit dictated by the old set of chirped mirrors of 1150 nm. After upgrading the set of chirped mirrors and by setting the amount of red-shift from SRS to reach up to 1300 nm, the cut-off energy is extended up to 290 eV (purple spectra), covering the carbon K-edge. This is verified by the insertion of a carbon filter. The ratio between the spectra recorded with and without the carbon filter (dashed black) agrees well with the filter transmission from [232] (black line).

XUV sensitive CCD camera Newton SO by *Andor*). Additional zirconium and carbon filters can be inserted to verify the measured harmonic spectra.

6.3   HHG extension to the carbon K-edge

In the first attempts, a set of chirped mirrors available at the time (PC1611 by *Ultafast Innovations*) was used, supporting a spectral bandwidth 850-1180 nm. Even though it was possible to broaden the spectrum via SRS up to 1300 nm, pulse compression was possible only for pulses with a bandwidth compatible with the chirped mirrors. With this limitation, there was no sig-

nificant advantage in terms of cut-off extension when broadening the driving pulses with SRS (see blue spectrum in Fig. 6.3.1) as compared to previous results with SPM [211]. In both cases, it is not possible to exceed 220 eV. Therefore, the setup was upgraded with a set of chirped mirrors supporting a bandwidth up to 1350 nm (PC147 by *Ultafast Innovations*). HHG spectra driven by pulses with extended bandwidth and larger red-shift show a clear extension of the cut-off, as well as a more continuous structure. This is in agreement with the expectation that for shorter pulse duration and longer driving wavelengths, less laser cycles contribute to the HHG process [67].

With this setting, the purple HHG spectrum shown in Fig. 6.3.1 is generated and the carbon K-shell absorption edge is verified by the insertion of a thin carbon filter. Also in Fig. 6.3.1 the good agreement between carbon filter transmission from literature (black)[232] and calculation from acquired spectra (dashed black) is shown.

With a set of chirped mirrors fulfilling the bandwidth requirements for both SPM and SRS, it is possible to switch between the two techniques with the same experimental setup simply by filling the HCF with a noble or a molecular gas (argon and nitrogen respectively, in this work). The SHG FROG characterization of post-compressed pulses via SPM and SRS is shown in Fig. 6.2.2. The compressed pulses obtained with the two techniques are then applied for driving HHG in neon and helium. In Fig. 6.3.2, the extension of the cut-off due to the red-shift of the central wavelength of the driving pulses is summarized.

For HHG driven in neon the cut-off is increased from 165 eV to 200 eV and for driving in helium it is increased from 220 eV to 290 eV. The four spectra shown in Fig. 6.3.2 are all recorded with a silver and a carbon filter and with the same acquisition parameters to be comparable among each other. The achieved flux is higher for HHG driven in neon than in helium, as expected, and the flux achieved by SPM and SRS are very similar. What may look like an increase in flux for SRS over SPM is due to the increase in transmission of the thin film filters for higher photon energies.
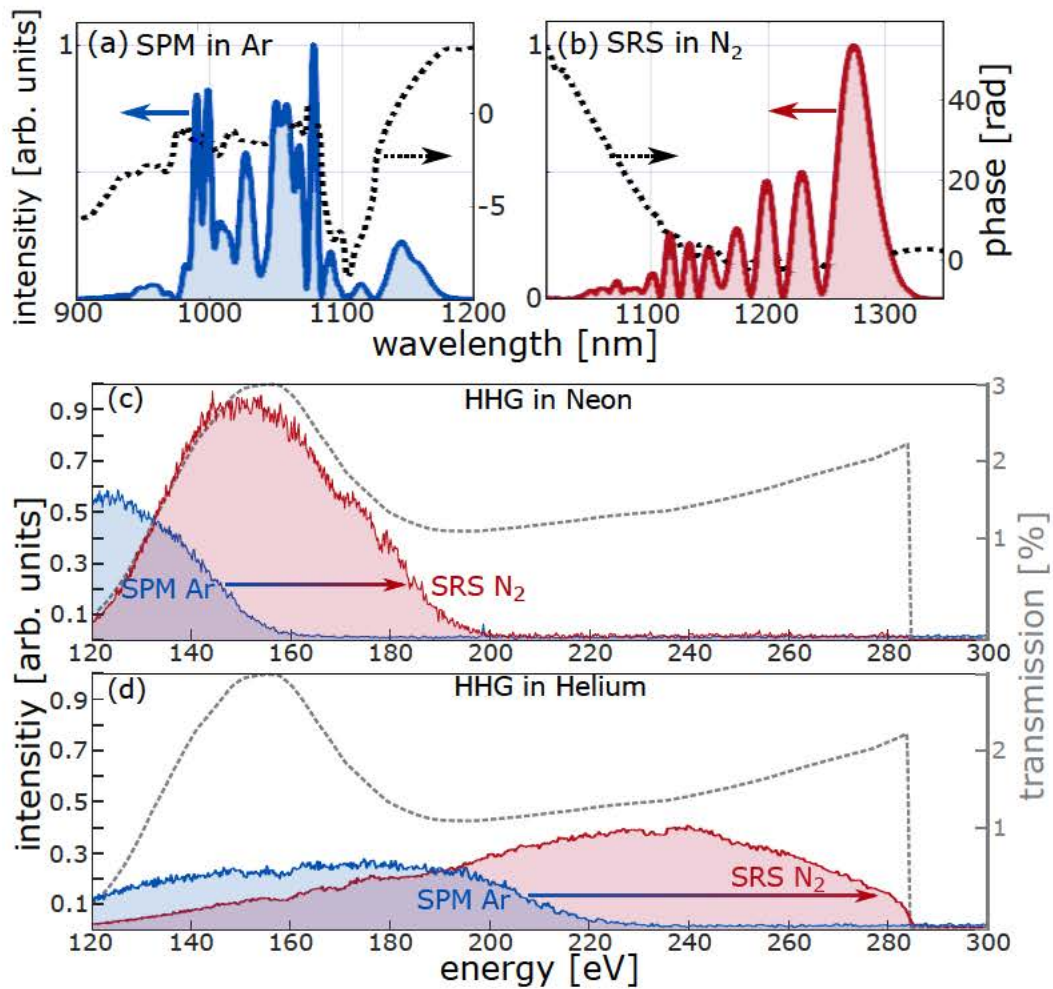
Figure 6.3.2: Top: Spectra of laser pulses after SPM (a) and SRS (b) in the HCF and compression by chirped mirrors. These spectra can support transform limited pulses with durations of 15 fs and 14.7 fs respectively. Bottom: Cut-off extension for HHG in neon (c) and helium (d) when driving with pulses red-shifted by SRS in nitrogen (red) as compared to pulses from SPM in argon (blue). All spectra with the additional carbon filter and the same acquisition parameters. The combined transmission of silver and carbon thin film filters and toroidal mirror is shown as dashed grey line.

6.4 Conclusion

In this chapter, the extension of the cut-off of phase-matched HHG, driven by ytterbium laser in combination with SRS in a HCF, to the carbon K-edge is demonstrated. This is the first demonstration of a driving scheme based on ytterbium lasers capable to reach such photon energy without relying on OPA or OPCPA frequency down-conversion. Considering the importance of drastically increasing the photon flux at the carbon K-edge for future spectro-scopic applications, there are three factors which make the proposed driving scheme particularly appealing. First, the laser source: ytterbium amplifiers are particularly suitable for energy and power scaling [233]. Second, the efficiency of conversion (from the laser to the HHG driver wavelength): not only the efficiency of SRS is higher than OPA, but on top of the red-shift it also induces enough spectral broadening to support pulse durations on the order of 20 fs. As a result, the performances in terms of delivered pulse duration can be superior than the typical scheme of Ti:Sa in combination with OPA. Third, the spectral range of the HHG driver: the moderate red-shift in the vicinity of the laser wavelength (1030nm) grants the possibility to drive HHG at the carbon K-edge with the optimal wavelength (<1300 nm), i.e. the shortest wavelength for which the target cut-off can still be reached. As an outlook, the scheme can be further improved by slightly increasing the bandwidth and the red-shift of the driving pulses in order to up-shift the maximum of the HHG spectrum. To summarize, the potential for the power scaling of the laser source and the optimized efficiency for the two frequency conversion processes involved, from the laser to the NIR driver and from the NIR driver to the soft X-rays, make the proposed driving scheme the ideal platform for the future developments of HHG sources in the water window, both for standard laboratories and large laser facilities.

"Nothing's louder than the end of a song that's always been there."

— Sir Terry Pratchett, *The Wee Free Men*

Chapter 7

Summary

Summarizing this thesis, intense ultrashort laser pulses were applied to the control of three dynamic electronic processes that occur on attosecond time scales. As established by the fundamentals of strong-field matter interaction, this is possible due to the direct coupling and sub-laser-cycle temporal mapping between electron dynamics and the laser electric field.

The first process that was investigated was the transient transfer of electrons between separate quantum entities, from one argon atom to the other within an argon dimer, dubbed LITE, was found to be influenced by the CEP of few-cycle laser pulses. This is identified as a possible route to the control of dynamics in molecular compounds as it is linked to the timing and momenta of subsequent electron emission via electron-electron interaction. Then, in the same sample system of argon dimers, these newfound concepts were refined. It was shown that in this system LITE also plays a decisive role in the process of FFI, demonstrating for the first time the control of electronic excitation across system boundaries via CEP. In asymmetric systems and/or with carefully designed two-dimensional laser waveforms, further control of the energy spectrum or localization of recaptured electrons might be possible. Such a charge transfer and excitation processes are crucial in many important processes between closely-spaced but separate quantum systems, such as photosynthesis, photocatalysis or solar-driven energy production.

127

Finally, on the process of HHG, a new and practical approach to drive HHG by a combination of an ytterbium based laser system operating at 1030 nm and further pulse preparation by SRS in a HCF is presented. This approach is successfully utilized to generate harmonic radiation surpassing the carbon K-edge of 284 eV, thus exceeding previous limitations. Due to the energy scalability of the laser system and high efficiency of the wavelength conversion from the fundamental pulse to the red-shifted HHG driver pulse, this is a promising new platform for scaling of HHG photon flux, especially in the 200-300 eV spectral region. It is expected that this driving scheme can be further developed to also extend farther into the water window spectral region such that it could become the go-to platform for investigations therein.

130

List of abbreviations

I_p ionization potential. 17–19, 26

R_{eq} equilibrium internuclear distance. 57, 65, 66, 88, 89, 107

U_p ponderomotive energy. 20–22, 26, 50

APM Innovation Academy for Precision Measurement Science and Technology. 56, 67, 94

ATI above threshold ionization. 17, 18, 22, 49, 50

CEP carrier-envelope phase. 14, 19, 23, 33, 36, 46, 48–51, 53, 55, 58–70, 73, 74, 79–81, 83–87, 89–97, 102–106, 108, 109, 127

COLTRIMS cold target recoil ion momentum spectroscopy. 14, 33, 51, 53, 54, 65, 88

CPA chirped pulse amplifier. 34, 35, 37, 38, 119

EWP electron wave packet. 15, 17–23, 25, 26

FFI frustrated field ionization. 14, 22–25, 30, 56, 87, 89, 91, 92, 95, 100, 101, 104, 105, 108, 127

HCF hollow core fiber. 30, 32, 33, 36–40, 42–45, 111, 115, 117–121, 123–125, 128

List of abbreviations

HHG high-order harmonic generation. 14–16, 22, 23, 25–28, 34, 39, 111–113, 115–121, 123–125, 128

KER kinetic energy released. 58, 66, 89–91

LITE laser-induced transfer of electron. 14, 16, 30, 60, 65, 72–79, 81, 83, 84, 86, 91–93, 95, 99, 101, 103, 107–109, 127

MCP micro channel plates. 49, 50, 53, 54

MPI multi photon ionization. 17, 18, 31

NEXAFS near-edge x-ray absorption fine structure. 112

NIR near infra-red. 31, 112, 113, 118, 120, 125

OPA optical parametric amplification. 113, 117, 118, 125

OPCPA optical parametric chirped pulse amplification. 115, 125

SFA strong field approximation. 19, 20

SHG FROG second harmonic generation frequency resolved optical gating. 33, 46–48, 119–121, 123

SPM self phase modulation. 33, 35–43, 45, 46, 111, 115, 117–121, 123, 124

SRS stimulated Raman scattering. 14, 30, 32, 33, 38–40, 42–46, 111, 115–125, 128

Ti:Sa titanium doped sapphire. 33, 35–37, 39, 113, 115, 117, 118, 125

TOF time-of-flight. 53–55, 88

vdW van der Waals. 29, 52, 64, 65, 87, 88

XUV extreme ultra-violet. 14, 15, 25, 28, 112, 113, 122

Yb:CaF$_2$ ytterbium-doped calcium fluoride. 35, 39, 111, 116, 118, 119

132

Bibliography

[1] V. Hanus, S. Kangaparambil, S. Larimian, M. Dorner-Kirchner, X. Xie, M. S. Schöffler, G. G. Paulus, A. Baltuška, A. Staudte, and M. Kitzler-Zeiler, "Subfemtosecond Tracing of Molecular Dynamics during Strong-Field Interaction," Phys. Rev. Lett. **123**, 263201 (2019). (Cited on p. 89.)

[2] V. Hanus, S. Kangaparambil, S. Larimian, M. Dorner-Kirchner, X. Xie, M. S. Schöffler, G. G. Paulus, A. Baltuška, A. Staudte, and M. Kitzler-Zeiler, "Experimental separation of subcycle ionization bursts in strong-field double ionization of h_2," Phys. Rev. Lett. **124**, 103201 (2020). (cited in Publication List)

[3] S. Kangaparambil, V. Hanus, M. Dorner-Kirchner, P. He, S. Larimian, G. Paulus, A. Baltuška, X. Xie, K. Yamanouchi, F. He, E. Lötstedt, and M. Kitzler-Zeiler, "Generalized phase sensitivity of directional bond breaking in the laser-molecule interaction," Phys. Rev. Lett. **125**, 023202 (2020). (cited in Publication List)

[4] Y. Wang, X. Lai, S. Yu, R. Sun, X. Liu, M. Dorner-Kirchner, S. Erattupuzha, S. Larimian, M. Koch, V. Hanus, S. Kangaparambil, G. Paulus, A. Baltuška, X. Xie, and M. Kitzler-Zeiler, "Laser-induced electron transfer in the dissociative multiple ionization of argon dimers," Phys. Rev. Lett. **125**, 063202 (2020). (Cited on p. 14, 88, and 89.)

[5] V. Hanus, S. Kangaparambil, S. Larimian, M. Dorner-Kirchner, X. Xie,

A. Baltuška, and M. Kitzler-Zeiler, "Exploring photoelectron angular distributions emitted from molecular dimers by two delayed intense laser pulses," Phys. Rev. A **102**, 053115 (2020). (cited in Publication List)

[6] H. Hu, S. Kangaparambi, M. Dorner-Kirchner, V. Hanus, A. Baltuška, M. Kitzler-Zeiler, and X. Xie, "Quantitative retrieval of the angular dependence of laser-induced electron rescattering in molecules," Phys. Rev. A **103**, 013114 (2021). (cited in Publication List)

[7] M. Dorner-Kirchner, S. Erattupuzha, S. Larimian, M. Koch, V. Hanus, S. Kangaparambil, G. Paulus, A. Baltuška, X. Xie, M. Kitzler-Zeiler, Y. Wang, X. Lai, S. Yu, R. Sun, and X. Liu, "Laser-subcycle control of electronic excitation across system boundaries," Journal of Physics B: Atomic, Molecular and Optical Physics **54**, 164004 (2021). (Cited on p. 14.)

[8] M. Dorner-Kirchner, V. Shumakova, G. Coccia, E. Kaksis, B. Schmidt, V. Pervak, A. Pugzlys, A. Baltuška, M. Kitzler-Zeiler, and P.-A. Carpeggiani, "Hhg at the carbon k-edge directly driven by srs red-shifted pulses from an ytterbium amplifier," In Preparation **-**, – (2022). (Cited on p. 14.)

[9] S. R. Leone, C. W. McCurdy, J. Burgdörfer, L. S. Cederbaum, Z. Chang, N. Dudovich, J. Feist, C. H. Greene, M. Ivanov, R. Kienberger, U. Keller, M. F. Kling, Z.-H. Loh, T. Pfeifer, A. N. Pfeiffer, R. Santra, K. Schafer, A. Stolow, U. Thumm, and M. J. J. Vrakking, "What will it take to observe processes in 'real time'?" Nat. Photonics **8**, 162–166 (2014). (Cited on p. 13.)

[10] M. Kitzler and S. Gräfe, eds., *Ultrafast Dynamics Driven by Intense Light Pulses*, vol. 86 of *Springer Series on Atomic, Optical, and Plasma Physics* (Springer International Publishing, Cham, 2016). (Cited on p. 13.)

[11] A. H. Zewail, "Femtochemistry. Past, present, and future," Pure Appl.

Chem. **72**, 2219–2231 (2000). (Cited on p. 13.)

[12] C. Maharjan, A. Alnaser, X. Tong, B. Ulrich, P. Ranitovic, S. Ghimire, Z. Chang, I. Litvinyuk, and C. Cocke, "Momentum imaging of doubly charged ions of Ne and Ar in the sequential ionization region," Phys. Rev. A **72**, 041403 (2005). (Cited on p. 14.)

[13] T. Udem, T. Hänsch, and R. Holzwarth, "Optical frequency metrology," Nature **416**, 233–237 (2002). (Cited on p. 14.)

[14] S.-W. Huang, G. Cirmi, J. Moses, K.-h. Hong, S. Bhardwaj, J. R. Birge, L.-j. Chen, E. Li, B. J. Eggleton, G. Cerullo, and F. X. Kärtner, "High-energy pulse synthesis with sub-cycle waveform control for strong-field physics," Nat. Photonics **5**, 475–479 (2011). (Cited on p. 14.)

[15] F. Krausz, "The birth of attosecond physics and its coming of age," Phys. Scr. **91**, 063011 (2016). (Cited on p. 14.)

[16] J. L. Krause, K. J. Schafer, and K. C. Kulander, "High-order harmonic generation from atoms and ions in the high intensity regime," Physical Review Letters **68**, 3535–3538 (1992). (Cited on p. 15.)

[17] P. B. Corkum, "Plasma perspective on strong field multiphoton ionization," Physical Review Letters **71**, 1994–1997 (1993). (Cited on p. 15, 23, 25, 26, and 112.)

[18] K. J. Schafer, B. Yang, L. F. Dimauro, and K. C. Kulander, "Above threshold ionization beyond the high harmonic cutoff," Phys. Rev. Lett. **70**, 1599–1602 (1993). (Cited on p. 15.)

[19] G. G. Paulus, W. Becker, W. Nicklich, and H. Walther, "Rescattering effects in above-threshold ionization: a classical model," J. Phys. B At. Mol. Opt. Phys. **27**, L703–L708 (1994). (Cited on p. 15 and 98.)

[20] G. S. Voronov and N. B. Delone, "Ionization of the xenon atom by the electric field of ruby laser emission," Soviet Journal of Experimental and Theoretical Physics Letters **1**, 66 (1965). (Cited on p. 17.)

[21] P. Agostini, F. Fabre, G. Mainfray, G. Petite, and N. Rahman, "Free-

Free Transitions Following Six-Photon Ionization of Xenon Atoms," Phys. Rev. Lett. **42**, 1127–1130 (1979). (Cited on p. 18.)

[22] D. G. Arbó, S. Yoshida, E. Persson, K. Dimitriou, and J. Burgdörfer, "Interference Oscillations in the Angular Distribution of Laser-Ionized Electrons near Ionization Threshold," Phys. Rev. Lett. **96**, 143003 (2006). (Cited on p. 18.)

[23] D. G. Arbó, K. L. Ishikawa, K. Schiessl, E. Persson, and J. Burgdörfer, "Intracycle and intercycle interferences in above-threshold ionization: The time grating," Phys. Rev. A **81**, 021403 (2010). (Cited on p. 18.)

[24] L. Keldysh, "Ionization in the field of a strong electromagnetic wave," Zh. Eksp. Teor. Fiz. **47**, 1945–1957 (1964). (Cited on p. 18 and 19.)

[25] G. Paulus, F. Lindner, H. Walther, A. Baltuška, E. Goulielmakis, M. Lezius, and F. Krausz, "Measurement of the Phase of Few-Cycle Laser Pulses," Phys. Rev. Lett. **91**, 253004 (2003). (Cited on p. 19 and 49.)

[26] T. Wittmann, B. Horvath, W. Helml, M. Schätzel, X. Gu, A. Cavalieri, G. Paulus, and R. Kienberger, "Single-shot carrier-envelope phase measurement of few-cycle laser pulses," Nat. Phys. **5**, 357–362 (2009). (Cited on p. 19 and 49.)

[27] A. Scrinzi, M. Geissler, and T. Brabec, "Ionization Above the Coulomb Barrier," Phys. Rev. Lett. **83**, 706–709 (1999). (Cited on p. 19, 56, and 67.)

[28] F. Faisal, "Multiple absorption of laser photons by atoms," J. Phys. B At. Mol. **6**, L89 (1973). (Cited on p. 19 and 69.)

[29] H. Reiss, "Effect of an intense electromagnetic field on a weakly bound system," Phys. Rev. A **22**, 1786–1813 (1980). (Cited on p. 19 and 69.)

[30] P. Dietrich, N. Burnett, M. Ivanov, and P. Corkum, "High-harmonic generation and correlated two-electron multiphoton ionization with

elliptically polarized light," Phys. Rev. A **50**, R3585–R3588 (1994). (Cited on p. 21.)

[31] P. Corkum, "Plasma perspective on strong field multiphoton ionization," Phys. Rev. Lett. **71**, 1994–1997 (1993). (Cited on p. 21.)

[32] M. Lewenstein, P. Balcou, M. Y. Ivanov, A. L'Huillier, and P. B. Corkum, "Theory of high-harmonic generation by low-frequency laser fields," Physical Review A **49**, 2117–2132 (1994). (Cited on p. 21, 26, and 112.)

[33] S. Baker, J. S. Robinson, C. A. Haworth, H. Teng, R. A. Smith, C. C. Chirila, M. Lein, J. W. G. Tisch, and J. P. Marangos, "Probing proton dynamics in molecules on an attosecond time scale." Science **312**, 424–7 (2006). (Cited on p. 22.)

[34] M. Lein, "Molecular imaging using recolliding electrons," J. Phys. B At. Mol. Opt. Phys. **40**, R135–R173 (2007). (Cited on p. 22.)

[35] B. Yang, K. J. Schafer, B. Walker, K. C. Kulander, P. Agostini, and L. F. DiMauro, "Intensity-dependent scattering rings in high order above-threshold ionization," Phys. Rev. Lett. **71**, 3770–3773 (1993). (Cited on p. 22.)

[36] G. Paulus, W. Nicklich, H. Xu, P. Lambropoulos, and H. Walther, "Plateau in above threshold ionization spectra," Phys. Rev. Lett. **72**, 2851–2854 (1994). (Cited on p. 22.)

[37] W. Becker, F. Grasbon, R. Kopold, D. B. Milosevic, G. G. Paulus, and H. Walther, "Above-threshold ionization: From classical features to quantum effects," Adv. At. Mol. Opt. Phys. **48**, 35–98 (2002). (Cited on p. 22 and 98.)

[38] B. Feuerstein, R. Moshammer, D. Fischer, A. Dorn, C. Schröter, J. Deipenwisch, J. Crespo Lopez-Urrutia, C. Höhr, P. Neumayer, J. Ullrich, H. Rottke, C. Trump, M. Wittmann, G. Korn, and W. Sandner, "Separation of Recollision Mechanisms in Nonsequential Strong Field

Double Ionization of Ar: The Role of Excitation Tunneling," Phys. Rev. Lett. **87**, 043003 (2001). (Cited on p. 23, 72, and 75.)

[39] A. Rudenko, K. Zrost, B. Feuerstein, V. de Jesus, C. Schröter, R. Moshammer, and J. Ullrich, "Correlated Multielectron Dynamics in Ultrafast Laser Pulse Interactions with Atoms," Phys. Rev. Lett. **93**, 253001 (2004). (Cited on p. 23, 72, and 75.)

[40] X. Liu and C. Figueira de Morisson Faria, "Nonsequential Double Ionization with Few-Cycle Laser Pulses," Phys. Rev. Lett. **92**, 133006 (2004). (Cited on p. 23.)

[41] X. Liu, H. Rottke, E. Eremina, W. Sandner, E. Goulielmakis, K. O'Keeffe, M. Lezius, F. Krausz, F. Lindner, M. Schätzel, G. Paulus, and H. Walther, "Nonsequential Double Ionization at the Single-Optical-Cycle Limit," Phys. Rev. Lett. **93**, 263001 (2004). (Cited on p. 23.)

[42] X. Xie, K. Doblhoff-Dier, S. Roither, M. S. Schöffler, D. Kartashov, H. Xu, T. Rathje, G. G. Paulus, A. Baltuška, S. Gräfe, and M. Kitzler, "Attosecond-Recollision-Controlled Selective Fragmentation of Polyatomic Molecules," Phys. Rev. Lett. **109**, 243001 (2012). (Cited on p. 23, 65, 89, and 105.)

[43] T. Nubbemeyer, K. Gorling, A. Saenz, U. Eichmann, and W. Sandner, "Strong-Field Tunneling without Ionization," Phys. Rev. Lett. **101**, 233001 (2008). (Cited on p. 23, 24, 87, and 105.)

[44] J. Krause, K. Schafer, and K. Kulander, "High-order harmonic generation from atoms and ions in the high intensity regime," Phys. Rev. Lett. **68**, 3535–3538 (1992). (Cited on p. 23 and 25.)

[45] N. I. Shvetsov-Shilovski, S. P. Goreslavski, S. V. Popruzhenko, and W. Becker, "Capture into rydberg states and momentum distributions of ionized electrons," Laser Phys. **19**, 1550–1558 (2009). (Cited on p. 24, 103, and 105.)

[46] S. Larimian, S. Erattupuzha, C. Lemell, S. Yoshida, S. Nagele, R. Mau-

rer, A. Baltuška, J. Burgdörfer, M. Kitzler, and X. Xie, "Coincidence spectroscopy of high-lying Rydberg states produced in strong laser fields," Phys. Rev. A **94**, 033401 (2016). (Cited on p. 24, 87, 88, and 105.)

[47] S. Larimian, C. Lemell, V. Stummer, J.-W. Geng, S. Roither, D. Kartashov, L. Zhang, M.-X. Wang, Q. Gong, L.-Y. Peng, S. Yoshida, J. Burgdörfer, A. Baltuška, M. Kitzler, and X. Xie, "Localizing high-lying Rydberg wave packets with two-color laser fields," Phys. Rev. A **96**, 021403 (2017). (Cited on p. 24, 54, 56, 87, 88, 105, 108, and 109.)

[48] S. Larimian, S. Erattupuzha, A. Baltuška, M. Kitzler-Zeiler, and X. Xie, "Frustrated double ionization of argon atoms in strong laser fields," Phys. Rev. Res. **2**, 013021 (2020). (Cited on p. 24, 87, and 105.)

[49] B. Manschwetus, H. Rottke, G. Steinmeyer, L. Foucar, A. Czasch, H. Schmidt-Böcking, and W. Sandner, "Mechanisms underlying strong-field double ionization of argon dimers," Phys. Rev. A **82**, 013413 (2010). (Cited on p. 24, 64, 66, 83, 87, 89, 91, 95, and 105.)

[50] A. Mokhberi, M. Hennrich, and F. Schmidt-Kaler, *Trapped Rydberg ions: A new platform for quantum information processing* (Academic Press, 2020), vol. 69 of *Advances In Atomic, Molecular, and Optical Physics*, chap. 4, pp. 233–306. (Cited on p. 24.)

[51] G. Higgins, "A single trapped rydberg ion," Phd thesis, Stockholm University, Department of Physics and University of Innsbruck, Institute for Experimental Physics (2018). (Cited on p. 24.)

[52] N. Šibalić and C. S. Adams, *Rydberg Physics*, 2399-2891 (IOP Publishing, 2018). (Cited on p. 24.)

[53] J. Nee, M. Suto, and L. Lee, "Photoexcitation processes of CH3OH: Rydberg states and photofragment fluorescence," Chem. Phys. **98**, 147–155 (1985). (Cited on p. 24, 86, and 105.)

[54] M. N. R. Ashfold, G. A. King, D. Murdock, M. G. D. Nix, T. A. A. Oliver, and A. G. Sage, "πσ* excited states in molecular photochem-

istry," Phys. Chem. Chem. Phys. **12**, 1218–1238 (2010). (Cited on p. 24, 86, and 105.)

[55] Z. Chen, A. T. J. B. Eppink, B. Jiang, G. C. Groenenboom, X. Yang, and D. H. Parker, "Product pair correlation in CH 3 OH photodissociation at 157 nm: the OH + CH 3 channel," Phys. Chem. Chem. Phys. **13**, 2350–2355 (2011). (Cited on p. 24, 86, and 105.)

[56] D. R. Weinberg, C. J. Gagliardi, J. F. Hull, C. F. Murphy, C. A. Kent, B. C. Westlake, A. Paul, D. H. Ess, D. G. McCafferty, and T. J. Meyer, "Proton-Coupled Electron Transfer," Chem. Rev. **112**, 4016–4093 (2012). (Cited on p. 24 and 86.)

[57] X. Liu, T. N. V. Karsili, A. L. Sobolewski, and W. Domcke, "Photocatalytic Water Splitting with the Acridine Chromophore: A Computational Study," J. Phys. Chem. B **119**, 10664–10672 (2015). (Cited on p. 24 and 86.)

[58] D. A. Horke, H. M. Watts, A. D. Smith, E. Jager, E. Springate, O. Alexander, C. Cacho, R. T. Chapman, and R. S. Minns, "Hydrogen Bonds in Excited State Proton Transfer," Phys. Rev. Lett. **117**, 163002 (2016). (Cited on p. 24, 64, and 86.)

[59] M. Koch, P. Heim, B. Thaler, M. Kitzler, and W. E. Ernst, "Direct observation of a photochemical activation energy: a case study of acetone photodissociation," J. Phys. B At. Mol. Opt. Phys. **50**, 125102 (2017). (Cited on p. 24, 86, and 105.)

[60] B. Jochim, R. Siemering, M. Zohrabi, O. Voznyuk, J. B. Mahowald, D. G. Schmitz, K. J. Betsch, B. Berry, T. Severt, N. G. Kling, T. G. Burwitz, K. D. Carnes, M. F. Kling, I. Ben-Itzhak, E. Wells, and R. de Vivie-Riedle, "The importance of Rydberg orbitals in dissociative ionization of small hydrocarbon molecules in intense laser fields," Sci. Rep. **7**, 4441 (2017). (Cited on p. 24, 86, and 105.)

[61] E. J. Rabe, K. L. Corp, A. L. Sobolewski, W. Domcke, and C. W. Schlenker, "Proton-Coupled Electron Transfer from Water to a Model

Heptazine-Based Molecular Photocatalyst," J. Phys. Chem. Lett. **9**, 6257–6261 (2018). (Cited on p. 24, 64, and 86.)

[62] M. Saffman, T. G. Walker, and K. Mølmer, "Quantum information with rydberg atoms," Rev. Mod. Phys. **82**, 2313–2363 (2010). (Cited on p. 24.)

[63] J. Tate, T. Auguste, H. G. Muller, P. Salières, P. Agostini, and L. F. DiMauro, "Scaling of wave-packet dynamics in an intense midinfrared field," Physical Review Letters **98** (2007). (Cited on p. 26 and 113.)

[64] A. D. Shiner, C. Trallero-Herrero, N. Kajumba, H.-C. Bandulet, D. Comtois, F. Légaré, M. Giguère, J.-C. Kieffer, P. B. Corkum, and D. M. Villeneuve, "Wavelength scaling of high harmonic generation efficiency," Physical Review Letters **103** (2009). (Cited on p. 26 and 113.)

[65] M. Hentschel, R. Kienberger, C. Spielmann, G. Reider, N. Milosevic, T. Brabec, P. Corkum, U. Heinzmann, M. Drescher, and F. Krausz, "Attosecond metrology," Nature **414**, 509–513 (2001). (Cited on p. 27.)

[66] P. B. Corkum, N. H. Burnett, and M. Y. Ivanov, "Subfemtosecond pulses," Opt. Lett. **19**, 1870 (1994). (Cited on p. 27.)

[67] T. Popmintchev, M.-C. Chen, P. Arpin, M. M. Murnane, and H. C. Kapteyn, "The attosecond nonlinear optics of bright coherent X-ray generation," Nat. Photonics **4**, 822–832 (2010). (Cited on p. 27, 28, 112, and 123.)

[68] E. Constant, D. Garzella, P. Breger, E. Mével, C. Dorrer, C. Le Blanc, F. Salin, and P. Agostini, "Optimizing High Harmonic Generation in Absorbing Gases: Model and Experiment," Phys. Rev. Lett. **82**, 1668–1671 (1999). (Cited on p. 28.)

[69] J. P. Marangos, "Development of high harmonic generation spectroscopy of organic molecules and biomolecules," J. Phys. B At. Mol. Opt. Phys. **49**, 132001 (2016). (Cited on p. 28.)

[70] R. Ganeev, "Harmonic generation in laser-produced plasmas containing

atoms, ions and clusters: a review," J. Mod. Opt. **59**, 409–439 (2012). (Cited on p. 28.)

[71] T. T. Luu, Z. Yin, A. Jain, T. Gaumnitz, Y. Pertot, J. Ma, and H. J. Wörner, "Extreme–ultraviolet high–harmonic generation in liquids," Nature Communications **9**, 3723 (2018). (Cited on p. 28.)

[72] S. Ghimire, G. Ndabashimiye, A. D. DiChiara, E. Sistrunk, M. I. Stockman, P. Agostini, L. F. DiMauro, and D. A. Reis, "Strong-field and attosecond physics in solids," J. Phys. B At. Mol. Opt. Phys. **47**, 204030 (2014). (Cited on p. 28.)

[73] A. von Veltheim, "Noble gas dimers in strong laser fields," Phd thesis, TU Berlin (2015). (Cited on p. 29.)

[74] Z. Ansari, M. Böttcher, B. Manschwetus, H. Rottke, W. Sandner, A. Verhoef, M. Lezius, G. G. Paulus, A. Saenz, and D. B. Milošević, "Interference in strong-field ionization of a two-centre atomic system," New Journal of Physics **10**, 093027 (2008). (Cited on p. 29.)

[75] T. Pradeep, B. Niu, and D. A. Shirley, "Photoelectron spectroscopy of rare gas dimers revisited: Vibrationally resolved photoelectron spectrum of argon dimer," The Journal of Chemical Physics **98**, 5269–5275 (1993). (Cited on p. 30.)

[76] R. Signorell, A. Wüest, and F. Merkt, "The first adiabatic ionization potential of ar2," The Journal of Chemical Physics **107**, 10819–10822 (1997). (Cited on p. 30.)

[77] G. Mie, "Beiträge zur optik trüber medien, speziell kolloidaler metallösungen," Annalen der Physik **330**, 377–445 (1908). (Cited on p. 31.)

[78] J. W. Strutt (3rd Baron Rayleigh), "Xxxiv. on the transmission of light through an atmosphere containing small particles in suspension, and on the origin of the blue of the sky," The London, Edinburgh, and Dublin Philosophical Magazine and Journal of Science **47**, 375–384 (1899). (Cited on p. 31.)

[79] C. V. Raman, "A new radiation (reproduced from indian j. phys., 1928, 2, 387-398)," Current Science **74**, 382–386 (1998). (Cited on p. 31 and 32.)

[80] G. G. Stokes, *On the change of refrangibility of light* (Royal Society London, 1852), vol. 142 of *Philosophical Transactions of the Royal Society of London*, chap. 21, pp. 463–562. (Cited on p. 32.)

[81] D. C. Harris and M. D. Bertolucci, *Symmetry and Spectroscopy* (Dover Publications, 1989). (Cited on p. 32.)

[82] W. E. Lamb, "Theory of an optical maser," Phys. Rev. **134**, A1429–A1450 (1964). (Cited on p. 34.)

[83] L. E. Hargrove, R. L. Fork, and M. A. Pollack, "Locking of he-ne laser modes induced by synchronous intracavity modulation," Applied Physics Letters **5**, 4–5 (1964). (Cited on p. 34.)

[84] D. Strickland and G. Mourou, "Compression of amplified chirped optical pulses," Opt. Commun. **56**, 219–221 (1985). (Cited on p. 34.)

[85] D. E. Spence, P. N. Kean, and W. Sibbett, "60-fsec pulse generation from a self-mode-locked ti:sapphire laser," Opt. Lett. **16**, 42–44 (1991). (Cited on p. 34.)

[86] F. Salin, J. Squier, and M. Piché, "Mode locking of ti:al2o3 lasers and self-focusing: a gaussian approximation," Opt. Lett. **16**, 1674–1676 (1991). (Cited on p. 34.)

[87] F. Verluise, V. Laude, Z. Cheng, C. Spielmann, and P. Tournois, "Amplitude and phase control of ultrashort pulses by use of an acousto-optic programmable dispersive filter: pulse compression and shaping," Opt. Lett. **25**, 575–577 (2000). (Cited on p. 37.)

[88] P. W. Roth, A. J. Maclean, D. Burns, and A. J. Kemp, "Directly diode-laser-pumped ti:sapphire laser," Opt. Lett. **34**, 3334–3336 (2009). (Cited on p. 37 and 117.)

[89] S. Sawai, A. Hosaka, H. Kawauchi, K. Hirosawa, and F. Kannari,

"Demonstration of a ti:sapphire mode-locked laser pumped directly with a green diode laser," Applied Physics Express **7**, 022702 (2014). (Cited on p. 37 and 117.)

[90] T. Fan, "Heat generation in nd:yag and yb:yag," IEEE Journal of Quantum Electronics **29**, 1457–1459 (1993). (Cited on p. 37.)

[91] G. Andriukaitis, E. Kaksis, T. Flöry, A. Pugžlys, and A. Baltuška, "Cryogenically cooled 30-mj yb:caf2 regenerative amplifier," in "Lasers Congress 2016 (ASSL, LSC, LAC)," (Optica Publishing Group, 2016), p. ATh4A.4. (Cited on p. 37 and 119.)

[92] O. Martinez, "3000 times grating compressor with positive group velocity dispersion: Application to fiber compensation in 1.3-1.6 μm region," IEEE Journal of Quantum Electronics **23**, 59–64 (1987). (Cited on p. 39.)

[93] E. Treacy, "Optical pulse compression with diffraction gratings," IEEE Journal of Quantum Electronics **5**, 454–458 (1969). (Cited on p. 39.)

[94] I. Yakovlev, "Stretchers and compressors for ultra-high power laser systems," Quantum Electronics **44**, 393 (2014). (Cited on p. 39.)

[95] Y.-G. Jeong, R. Piccoli, D. Ferachou, V. Cardin, M. Chini, S. Hädrich, J. Limpert, R. Morandotti, F. Légaré, B. E. Schmidt, and L. Razzari, "Direct compression of 170-fs 50-cycle pulses down to 1.5 cycles with 70% transmission," Scientific Reports **8**, 11794 (2018). (Cited on p. 39 and 117.)

[96] F. Shimizu, "Frequency broadening in liquids by a short light pulse," Phys. Rev. Lett. **19**, 1097–1100 (1967). (Cited on p. 40.)

[97] R. R. Alfano and S. L. Shapiro, "Observation of self-phase modulation and small-scale filaments in crystals and glasses," Phys. Rev. Lett. **24**, 592–594 (1970). (Cited on p. 40.)

[98] M. Nisoli, S. Stagira, S. De Silvestri, O. Svelto, S. Sartania, Z. Cheng, M. Lenzner, C. Spielmann, and F. Krausz, "A novel-high energy pulse

compression system: generation of multigigawatt sub-5-fs pulses," Appl. Phys. B Lasers Opt. **65**, 189–196 (1997). (Cited on p. 42.)

[99] P. A. Carpeggiani, G. Coccia, G. Fan, E. Kaksis, A. Pugžlys, A. Baltuška, R. Piccoli, Y.-G. Jeong, A. Rovere, R. Morandotti, L. Razzari, B. E. Schmidt, A. A. Voronin, and A. M. Zheltikov, "Extreme raman red shift: ultrafast multimode nonlinear space-time dynamics, pulse compression, and broadly tunable frequency conversion," Optica **7**, 1349 (2020). (Cited on p. 42, 43, 44, 45, 115, and 120.)

[100] C. Vozzi, M. Nisoli, G. Sansone, S. Stagira, and S. De Silvestri, "Optimal spectral broadening in hollow-fiber compressor systems," Applied Physics B **80**, 285–289 (2005). (Cited on p. 45 and 120.)

[101] R. Szipöcs, K. Ferencz, C. Spielmann, and F. Krausz, "Chirped multilayer coatings for broadband dispersion control in femtosecond lasers," Opt. Lett. **19**, 201–203 (1994). (Cited on p. 45.)

[102] R. Trebino, K. W. DeLong, D. N. Fittinghoff, J. N. Sweetser, M. A. Krumbügel, B. a. Richman, and D. J. Kane, "Measuring ultrashort laser pulses in the time-frequency domain using frequency-resolved optical gating," Rev. Sci. Instrum. **68**, 3277–3295 (1997). (Cited on p. 46 and 47.)

[103] G. Fan, T. Balčiūnas, C. Fourcade-Dutin, S. Haessler, A. A. Voronin, A. M. Zheltikov, F. Gérôme, F. Benabid, A. Baltuška, and T. Witting, "X-sea-f-spider characterization of over octave spanning pulses in the infrared range," Opt. Express **24**, 12713–12729 (2016). (Cited on p. 48 and 120.)

[104] A. Baltuska, M. Pshenichnikov, and D. Wiersma, "Second-harmonic generation frequency-resolved optical gating in the single-cycle regime," IEEE Journal of Quantum Electronics **35**, 459–478 (1999). (Cited on p. 48.)

[105] T. Rathje, N. G. Johnson, M. Möller, F. Süßmann, D. Adolph, M. Kübel, R. Kienberger, M. F. Kling, G. G. Paulus, and A. M. Sayler,

"Review of attosecond resolved measurement and control via carrier-envelope phase tagging with above-threshold ionization," J. Phys. B At. Mol. Opt. Phys. **45**, 074003 (2012). (Cited on p. 49, 50, 65, and 89.)

[106] S. Fukahori, T. Ando, S. Miura, R. Kanya, K. Yamanouchi, T. Rathje, and G. G. Paulus, "Determination of the absolute carrier-envelope phase by angle-resolved photoelectron spectra of Ar by intense circularly polarized few-cycle pulses," Phys. Rev. A **95**, 053410 (2017). (Cited on p. 51.)

[107] A. M. Sayler, T. Rathje, W. Müller, C. Kürbis, K. Rühle, G. Stibenz, and G. G. Paulus, "Real-time pulse length measurement of few-cycle laser pulses using above-threshold ionization," Opt. Express **19**, 4464 (2011). (Cited on p. 51 and 89.)

[108] G. Tejeda, B. Maté, J. M. Fernández-Sánchez, and S. Montero, "Temperature and density mapping of supersonic jet expansions using linear raman spectroscopy," Phys. Rev. Lett. **76**, 34–37 (1996). (Cited on p. 51 and 52.)

[109] S. Roither, "Investigation of strong laser field-induced fragmentation dynamics of hydrocarbon molecules using coincidence momentum imaging," Phd thesis, TU Wien (2011). (Cited on p. 51 and 53.)

[110] J. M. Calo, "Dimer formation in supersonic water vapor molecular beams," J. Chem. Phys. **62**, 4904–4910 (1975). (Cited on p. 52.)

[111] E. L. Knuth, "Dimer-formation rate coefficients from measurements of terminal dimer concentrations in free-jet expansions," The Journal of Chemical Physics **66**, 3515–3525 (1977). (Cited on p. 52.)

[112] J. Ullrich, R. Moshammer, R. Dörner, O. Jagutzki, V. Mergel, H. Schmidt-Böcking, and L. Spielberger, "Recoil-ion momentum spectroscopy," J. Phys. B At. Mol. Opt. Phys. **30**, 2917–2974 (1997). (Cited on p. 53.)

[113] R. Dörner, V. Mergel, O. Jagutzki, L. Spielberger, J. Ullrich, R. Moshammer, and H. Schmidt-Böcking, "Cold Target Recoil Ion

Momentum Spectroscopy: a momentum microscope to view atomic collision dynamics," Phys. Rep. **330**, 95–192 (2000). (Cited on p. 53, 65, and 87.)

[114] J. Ullrich, R. Moshammer, A. Dorn, R. Dörner, L. P. H. Schmidt, and H. Schmidt-Böcking, "Recoil-ion and electron momentum spectroscopy: reaction-microscopes," Reports Prog. Phys. **66**, 1463–1545 (2003). (Cited on p. 53 and 87.)

[115] X. Xie, C. Wu, Z. Yuan, D. Ye, P. Wang, Y. Deng, L. Fu, J. Liu, Y. Liu, and Q. Gong, "Dynamical coupling of electrons and nuclei for Coulomb explosion of argon trimers in intense laser fields," Phys. Rev. A **92**, 023417 (2015). (Cited on p. 56, 57, 67, and 94.)

[116] Q. Cheng, X. Xie, Z. Yuan, X. Zhong, Y. Liu, Q. Gong, and C. Wu, "Dissociative Ionization of Argon Dimer by Intense Femtosecond Laser Pulses," J. Phys. Chem. A **121**, 3891–3897 (2017). (Cited on p. 56, 57, 64, 67, 83, and 94.)

[117] X. Xie, S. Roither, S. Gräfe, D. Kartashov, E. Persson, C. Lemell, L. Zhang, M. S. Schöffler, A. Baltuška, J. Burgdörfer, and M. Kitzler, "Probing the influence of the Coulomb field on atomic ionization by sculpted two-color laser fields," New J. Phys. **15**, 043050 (2013). (Cited on p. 56.)

[118] L. Zhang, X. Xie, S. Roither, D. Kartashov, Y. Wang, C. Wang, M. Schöffler, D. Shafir, P. B. Corkum, A. Baltuška, I. Ivanov, A. Kheifets, X. Liu, A. Staudte, and M. Kitzler, "Laser-sub-cycle two-dimensional electron-momentum mapping using orthogonal two-color fields," Phys. Rev. A **90**, 061401 (2014). (Cited on p. 56 and 65.)

[119] M. S. Schöffler, X. Xie, P. Wustelt, M. Möller, S. Roither, D. Kartashov, A. M. Sayler, A. Baltuska, G. G. Paulus, and M. Kitzler, "Laser-subcycle control of sequential double-ionization dynamics of helium," Phys. Rev. A **93**, 063421 (2016). (Cited on p. 56.)

[120] P. Wustelt, M. Möller, M. S. Schöffler, X. Xie, V. Hanus, A. M. Sayler,

A. Baltuska, G. G. Paulus, and M. Kitzler, "Numerical investigation of the sequential-double-ionization dynamics of helium in different few-cycle-laser-field shapes," Phys. Rev. A **95**, 023411 (2017). (Cited on p. 56.)

[121] P. Ho, R. Panfili, S. Haan, and J. Eberly, "Nonsequential Double Ionization as a Completely Classical Photoelectric Effect," Phys. Rev. Lett. **94**, 093002 (2005). (Cited on p. 56.)

[122] L. Zhang, X. Xie, S. Roither, Y. Zhou, P. Lu, D. Kartashov, M. Schöffler, D. Shafir, P. B. Corkum, A. Baltuška, A. Staudte, and M. Kitzler, "Subcycle Control of Electron-Electron Correlation in Double Ionization," Phys. Rev. Lett. **112**, 193002 (2014). (Cited on p. 56 and 78.)

[123] S. Eckart, M. Richter, M. Kunitski, A. Hartung, J. Rist, K. Henrichs, N. Schlott, H. Kang, T. Bauer, H. Sann, L. P. H. Schmidt, M. Schöffler, T. Jahnke, and R. Dörner, "Nonsequential Double Ionization by Counterrotating Circularly Polarized Two-Color Laser Fields," Phys. Rev. Lett. **117**, 133202 (2016). (Cited on p. 56 and 105.)

[124] S. Augst, D. D. Meyerhofer, D. Strickland, and S. L. Chin, "Laser ionization of noble gases by Coulomb-barrier suppression," J. Opt. Soc. Am. B **8**, 858 (1991). (Cited on p. 56 and 67.)

[125] P. Slavíĉek, R. Kalus, P. Paŝka, I. Odvárková, P. Hobza, and A. Malijevský, "State-of-the-art correlated ab initio potential energy curves for heavy rare gas dimers: Ar2, kr2, and xe2," The Journal of Chemical Physics **119**, 2102–2119 (2003). (Cited on p. 57.)

[126] A. Yella, H.-W. Lee, H. N. Tsao, C. Yi, A. K. Chandiran, M. K. Nazeeruddin, E. W.-G. Diau, C.-Y. Yeh, S. M. Zakeeruddin, and M. Gratzel, "Porphyrin-Sensitized Solar Cells with Cobalt (II/III)-Based Redox Electrolyte Exceed 12 Percent Efficiency," Science **334**, 629–634 (2011). (Cited on p. 64 and 86.)

[127] J. Lu, S. Liu, and M. Wang, "Push-Pull Zinc Porphyrins as Light-

Harvesters for Efficient Dye-Sensitized Solar Cells," Front. Chem. **6** (2018). (Cited on p. 64 and 86.)

[128] O. Morawski, K. Izdebska, E. Karpiuk, J. Nowacki, A. Suchocki, and A. L. Sobolewski, "Photoinduced water splitting with oxotitanium tetraphenylporphyrin," Phys. Chem. Chem. Phys. **16**, 15256–15262 (2014). (Cited on p. 64 and 86.)

[129] M. D. Kärkäs, O. Verho, E. V. Johnston, and B. Åkermark, "Artificial Photosynthesis: Molecular Systems for Catalytic Water Oxidation," Chem. Rev. **114**, 11863–12001 (2014). (Cited on p. 64 and 86.)

[130] J. Barber, "Photosynthetic energy conversion: natural and artificial," Chem. Soc. Rev. **38**, 185–196 (2009). (Cited on p. 64 and 86.)

[131] J.-D. Rochaix, "Regulation of photosynthetic electron transport," Biochim. Biophys. Acta - Bioenerg. **1807**, 375–383 (2011). (Cited on p. 64 and 86.)

[132] M. F. Kling, C. Siedschlag, A. J. Verhoef, J. I. Khan, M. Schultze, T. Uphues, Y. Ni, M. Uiberacker, M. Drescher, F. Krausz, and M. J. J. Vrakking, "Control of electron localization in molecular dissociation." Science **312**, 246–8 (2006). (Cited on p. 64 and 86.)

[133] M. F. Kling, P. von den Hoff, I. Znakovskaya, and R. de Vivie-Riedle, "(Sub-)femtosecond control of molecular reactions via tailoring the electric field of light." Phys. Chem. Chem. Phys. **15**, 9448–67 (2013). (Cited on p. 64 and 86.)

[134] M. Kremer, B. Fischer, B. Feuerstein, V. L. B. de Jesus, V. Sharma, C. Hofrichter, A. Rudenko, U. Thumm, C. D. Schröter, R. Moshammer, and J. Ullrich, "Electron Localization in Molecular Fragmentation of H2 by Carrier-Envelope Phase Stabilized Laser Pulses," Phys. Rev. Lett. **103**, 213003 (2009). (Cited on p. 64 and 86.)

[135] B. Fischer, M. Kremer, T. Pfeifer, B. Feuerstein, V. Sharma, U. Thumm, C. Schröter, R. Moshammer, and J. Ullrich, "Steering

the Electron in H2+ by Nuclear Wave Packet Dynamics," Phys. Rev. Lett. **105**, 223001 (2010). (Cited on p. 64 and 86.)

[136] I. Znakovskaya, P. von den Hoff, G. Marcus, S. Zherebtsov, B. Bergues, X. Gu, Y. Deng, M. Vrakking, R. Kienberger, F. Krausz, R. de Vivie-Riedle, and M. Kling, "Subcycle Controlled Charge-Directed Reactivity with Few-Cycle Midinfrared Pulses," Phys. Rev. Lett. **108**, 063002 (2012). (Cited on p. 64 and 86.)

[137] H. Lippert, V. Stert, C. P. Schulz, I. V. Hertel, and W. Radloff, "Photoinduced hydrogen transfer reaction dynamics in indole-ammonia clusters at different excitation energies," Phys. Chem. Chem. Phys. **6**, 2718–2724 (2004). (Cited on p. 64.)

[138] T. Schultz, E. Samoylova, W. Radloff, I. V. Hertel, A. L. Sobolewski, and W. Domcke, "Efficient Deactivation of a Model Base Pair via Excited-State Hydrogen Transfer," Science **306**, 1765–1768 (2004). (Cited on p. 64.)

[139] J. Ehrmaier, T. N. Karsili, A. L. Sobolewski, and W. Domcke, "Mechanism of Photocatalytic Water Splitting with Graphitic Carbon Nitride: Photochemistry of the Heptazine-Water Complex," J. Phys. Chem. A **121**, 4754–4764 (2017). (Cited on p. 64.)

[140] L. Cederbaum, J. Zobeley, and F. Tarantelli, "Giant Intermolecular Decay and Fragmentation of Clusters," Phys. Rev. Lett. **79**, 4778–4781 (1997). (Cited on p. 64.)

[141] T. Jahnke, A. Czasch, M. S. Schöffler, S. Schössler, A. Knapp, M. Käsz, J. Titze, C. Wimmer, K. Kreidi, R. E. Grisenti, A. Staudte, O. Jagutzki, U. Hergenhahn, H. Schmidt-Böcking, and R. Dörner, "Experimental Observation of Interatomic Coulombic Decay in Neon Dimers," Phys. Rev. Lett. **93**, 163401 (2004). (Cited on p. 64.)

[142] N. Sisourat, N. V. Kryzhevoi, P. Kolorenč, S. Scheit, T. Jahnke, and L. S. Cederbaum, "Ultralong-range energy transfer by interatomic

Coulombic decay in an extreme quantum system," Nat. Phys. **6**, 508–511 (2010). (Cited on p. 64.)

[143] T. Mizuno, P. Cörlin, T. Miteva, K. Gokhberg, A. Kuleff, L. S. Cederbaum, T. Pfeifer, A. Fischer, and R. Moshammer, "Time-resolved observation of interatomic excitation-energy transfer in argon dimers," J. Chem. Phys. **146**, 104305 (2017). (Cited on p. 64.)

[144] X. Ren, E. Jabbour Al Maalouf, A. Dorn, and S. Denifl, "Direct evidence of two interatomic relaxation mechanisms in argon dimers ionized by electron impact," Nat. Commun. **7**, 11093 (2016). (Cited on p. 64.)

[145] B. Ulrich, A. Vredenborg, A. Malakzadeh, M. Meckel, K. Cole, M. Smolarski, Z. Chang, T. Jahnke, and R. Dörner, "Double-ionization mechanisms of the argon dimer in intense laser fields," Phys. Rev. A - At. Mol. Opt. Phys. **82**, 013412 (2010). (Cited on p. 64, 66, 83, 87, 89, 91, and 95.)

[146] J. Wu, A. Vredenborg, B. Ulrich, L. Schmidt, M. Meckel, S. Voss, H. Sann, H. Kim, T. Jahnke, and R. Dörner, "Multiple Recapture of Electrons in Multiple Ionization of the Argon Dimer by a Strong Laser Field," Phys. Rev. Lett. **107**, 043003 (2011). (Cited on p. 64, 66, 87, 89, 91, 95, and 107.)

[147] B. Ulrich, A. Vredenborg, A. Malakzadeh, L. P. H. Schmidt, T. Havermeier, M. Meckel, K. Cole, M. Smolarski, Z. Chang, T. Jahnke, and R. Dörner, "Imaging of the Structure of the Argon and Neon Dimer, Trimer, and Tetramer," J. Phys. Chem. A **115**, 6936–6941 (2011). (Cited on p. 64 and 83.)

[148] J. Wu, A. Vredenborg, B. Ulrich, L. P. H. Schmidt, M. Meckel, S. Voss, H. Sann, H. Kim, T. Jahnke, and R. Dörner, "Nonadiabatic alignment of van der Waals - Force-bound argon dimers by femtosecond laser pulses," Phys. Rev. A - At. Mol. Opt. Phys. **83**, 061403 (2011). (Cited on p. 64.)

[149] J. Wu, M. Kunitski, L. P. H. Schmidt, T. Jahnke, and R. Dörner,

"Structures of N2Ar, O2Ar, and O2Xe dimers studied by Coulomb explosion imaging," J. Chem. Phys. **137**, 104308 (2012). (Cited on p. 64.)

[150] K. Hoshina, H. Hagihara, and M. Tsuge, "Double ionization and coulomb explosion of the formic acid dimer by intense near-infrared femtosecond laser pulses," J. Phys. Chem. A **116**, 826–831 (2012). (Cited on p. 64.)

[151] J. Wu, M. Meckel, L. Schmidt, M. Kunitski, S. Voss, H. Sann, H. Kim, T. Jahnke, A. Czasch, and R. Dörner, "Probing the tunnelling site of electrons in strong field enhanced ionization of molecules," Nat. Commun. **3**, 1113 (2012). (Cited on p. 64.)

[152] A. von Veltheim, B. Manschwetus, W. Quan, B. Borchers, G. Steinmeyer, H. Rottke, and W. Sandner, "Frustrated Tunnel Ionization of Noble Gas Dimers with Rydberg-Electron Shakeoff by Electron Charge Oscillation," Phys. Rev. Lett. **110**, 023001 (2013). (Cited on p. 64 and 87.)

[153] C. Wu, C. Wu, D. Song, H. Su, X. Xie, M. Li, Y. Deng, Y. Liu, and Q. Gong, "Communication: Determining the structure of the N2Ar van der Waals complex with laser-based channel-selected Coulomb explosion," J. Chem. Phys. **140**, 141101 (2014). (Cited on p. 64.)

[154] M. Amada, Y. Sato, M. Tsuge, and K. Hoshina, "Near-infrared femtosecond laser ionization of the acetic acid dimer," Chem. Phys. Lett. **624**, 24–28 (2015). (Cited on p. 64.)

[155] X. Ding, M. Haertelt, S. Schlauderer, M. S. Schuurman, A. Y. Naumov, D. M. Villeneuve, A. R. W. McKellar, P. B. Corkum, and A. Staudte, "Ultrafast Dissociation of Metastable CO2+ in a Dimer," Phys. Rev. Lett. **118**, 153001 (2017). (Cited on p. 64.)

[156] A. S. Bogomolov, V. G. Goldort, S. A. Kochubei, and A. V. Baklanov, "Photodissociation of van der Waals complexes of iodine X-I2 (X = I2

, C2H4) via charge-transfer state: A velocity map imaging investigation," J. Chem. Phys. **147**, 234304 (2017). (Cited on p. 64.)

[157] T. Ditmire, J. W. G. Tisch, E. Springate, M. B. Mason, N. Hay, R. A. Smith, J. Marangos, and M. H. R. Hutchinson, "High-energy ions produced in explosions of superheated atomic clusters," Nature **386**, 54–56 (1997). (Cited on p. 64.)

[158] V. Kumarappan, M. Krishnamurthy, and D. Mathur, "Asymmetric High-Energy Ion Emission from Argon Clusters in Intense Laser Fields," Phys. Rev. Lett. **87**, 085005 (2001). (Cited on p. 64.)

[159] C. Jungreuthmayer, M. Geissler, J. Zanghellini, and T. Brabec, "Microscopic Analysis of Large-Cluster Explosion in Intense Laser Fields," Phys. Rev. Lett. **92**, 133401 (2004). (Cited on p. 64.)

[160] T. Fennel, K. H. Meiwes-Broer, J. Tiggesbäumker, P. G. Reinhard, P. M. Dinh, and E. Suraud, "Laser-driven nonlinear cluster dynamics," Rev. Mod. Phys. **82**, 1793–1842 (2010). (Cited on p. 64.)

[161] B. Schütte, M. Arbeiter, T. Fennel, G. Jabbari, A. Kuleff, M. Vrakking, and A. Rouzée, "Observation of correlated electronic decay in expanding clusters triggered by near-infrared fields," Nat. Commun. **6**, 8596 (2015). (Cited on p. 64.)

[162] B. Schütte, C. Peltz, D. R. Austin, C. Strüber, P. Ye, A. Rouzée, M. J. Vrakking, N. Golubev, A. I. Kuleff, T. Fennel, and J. P. Marangos, "Low-Energy Electron Emission in the Strong-Field Ionization of Rare Gas Clusters," Phys. Rev. Lett. **121**, 063202 (2018). (Cited on p. 64.)

[163] C. Smeenk, J. Z. Salvail, L. Arissian, P. B. Corkum, C. T. Hebeisen, and A. Staudte, "Precise in-situ measurement of laser pulse intensity using strong field ionization," Opt. Express **19**, 9336 (2011). (Cited on p. 65 and 88.)

[164] X. Xie, T. Wang, S. Yu, X. Lai, S. Roither, D. Kartashov, A. Baltuška, X. Liu, A. Staudte, and M. Kitzler, "Disentangling Intracycle Interferences in Photoelectron Momentum Distributions Using Orthogonal

Two-Color Laser Fields," Phys. Rev. Lett. **119**, 243201 (2017). (Cited on p. 65.)

[165] Y. Wang, S. Xu, W. Quan, C. Gong, X. Lai, S. Hu, M. Liu, J. Chen, and X. Liu, "Recoil-ion momentum distribution for nonsequential double ionization of Xe in intense midinfrared laser fields," Phys. Rev. A **94**, 053412 (2016). (Cited on p. 72.)

[166] N. Camus, B. Fischer, M. Kremer, V. Sharma, A. Rudenko, B. Bergues, M. Kübel, N. G. Johnson, M. F. Kling, T. Pfeifer, J. Ullrich, and R. Moshammer, "Attosecond Correlated Dynamics of Two Electrons Passing through a Transition State," Phys. Rev. Lett. **108**, 073003 (2012). (Cited on p. 78.)

[167] B. Bergues, M. Kübel, N. G. Johnson, B. Fischer, N. Camus, K. J. Betsch, O. Herrwerth, A. Senftleben, A. M. Sayler, T. Rathje, T. Pfeifer, I. Ben-Itzhak, R. R. Jones, G. G. Paulus, F. Krausz, R. Moshammer, J. Ullrich, and M. F. Kling, "Attosecond tracing of correlated electron-emission in non-sequential double ionization," Nat. Commun. **3**, 813 (2012). (Cited on p. 78.)

[168] B. Sheehy, B. Walker, and L. DiMauro, "Phase Control in the Two-Color Photodissociation of HD+," Phys. Rev. Lett. **74**, 4799–4802 (1995). (Cited on p. 86.)

[169] D. Ray, F. He, S. De, W. Cao, H. Mashiko, P. Ranitovic, K. Singh, I. Znakovskaya, U. Thumm, G. Paulus, M. Kling, I. Litvinyuk, and C. Cocke, "Ion-Energy Dependence of Asymmetric Dissociation of D2 by a Two-Color Laser Field," Phys. Rev. Lett. **103**, 223201 (2009). (Cited on p. 86.)

[170] V. Tagliamonti, H. Chen, and G. N. Gibson, "Internuclear-separation-resolved asymmetric dissociation of I2 in a two-color laser field," Phys. Rev. A **84**, 043424 (2011). (Cited on p. 86.)

[171] V. Wanie, H. Ibrahim, S. Beaulieu, N. Thiré, B. E. Schmidt, Y. Deng, A. S. Alnaser, I. V. Litvinyuk, X.-M. Tong, and F. Légaré, "Coherent

control of D2/H2 dissociative ionization by a mid-infrared two-color laser field," J. Phys. B At. Mol. Opt. Phys. **49**, 025601 (2016). (Cited on p. 86.)

[172] H. Xu, H. Hu, X.-M. Tong, P. Liu, R. Li, R. T. Sang, and I. V. Litvinyuk, "Coherent control of the dissociation probability of H2+ in ω-3ω two-color fields," Phys. Rev. A **93**, 063416 (2016). (Cited on p. 86.)

[173] X. Xie, S. Roither, S. Larimian, S. Erattupuzha, L. Zhang, D. Kartashov, F. He, A. Baltuška, and M. Kitzler, "Zero-energy proton dissociation of H2+ through stimulated Raman scattering," Phys. Rev. A **99**, 043409 (2019). (Cited on p. 86.)

[174] S. Kangaparambil, V. Hanus, M. Dorner-Kirchner, P. He, S. Larimian, G. Paulus, A. Baltuška, X. Xie, K. Yamanouchi, F. He, E. Lötstedt, and M. Kitzler-Zeiler, "Generalized Phase Sensitivity of Directional Bond Breaking in the Laser-Molecule Interaction," Phys. Rev. Lett. **125**, 023202 (2020). (Cited on p. 86, 88, and 89.)

[175] Q. Song, P. Lu, X. Gong, Q. Ji, K. Lin, W. Zhang, J. Ma, H. Zeng, and J. Wu, "Dissociative double ionization of CO in orthogonal two-color laser fields," Phys. Rev. A **95**, 013406 (2017). (Cited on p. 86.)

[176] X. Gong, P. He, Q. Song, Q. Ji, H. Pan, J. Ding, F. He, H. Zeng, and J. Wu, "Two-Dimensional Directional Proton Emission in Dissociative Ionization of H2," Phys. Rev. Lett. **113**, 203001 (2014). (Cited on p. 86.)

[177] K. Lin, X. Gong, Q. Song, Q. Ji, W. Zhang, J. Ma, P. Lu, H. Pan, J. Ding, H. Zeng, and J. Wu, "Directional bond breaking by polarization-gated two-color ultrashort laser pulses," J. Phys. B At. Mol. Opt. Phys. **49**, 025603 (2016). (Cited on p. 86.)

[178] H. Ahmad, S. Kamarudin, L. Minggu, and M. Kassim, "Hydrogen from photo-catalytic water splitting process: A review," Renew. Sustain. Energy Rev. **43**, 599–610 (2015). (Cited on p. 86.)

Bibliography

[179] B. Manschwetus, T. Nubbemeyer, K. Gorling, G. Steinmeyer, U. Eich-
mann, H. Rottke, and W. Sandner, "Strong Laser Field Fragmentation
of H2: Coulomb Explosion without Double Ionization," Phys. Rev.
Lett. **102**, 113002 (2009). (Cited on p. 87.)

[180] U. Eichmann, T. Nubbemeyer, H. Rottke, and W. Sandner, "Acceler-
ation of neutral atoms in strong short-pulse laser fields." Nature **461**,
1261–4 (2009). (Cited on p. 87.)

[181] J. McKenna, S. Zeng, J. J. Hua, A. M. Sayler, M. Zohrabi, N. G. John-
son, B. Gaire, K. D. Carnes, B. D. Esry, and I. Ben-Itzhak, "Frustrated
tunneling ionization during laser-induced D2 fragmentation: Detection
of excited metastable D* atoms," Phys. Rev. A **84**, 043425 (2011).
(Cited on p. 87.)

[182] J. McKenna, A. M. Sayler, B. Gaire, N. G. Kling, B. D. Esry, K. D.
Carnes, and I. Ben-Itzhak, "Frustrated tunnelling ionization during
strong-field fragmentation of D 3 +," New J. Phys. **14**, 103029 (2012).
(Cited on p. 87.)

[183] S. M. Erattupuzha Joseph, "Control of molecular processes with intense
laser pulses," Phd thesis, TU Wien (2016). (Cited on p. 87 and 107.)

[184] H. Hu, S. Larimian, S. Erattupuzha, J. Wen, A. Baltuška, M. Kitzler-
Zeiler, and X. Xie, "Laser-induced dissociative recombination of carbon
dioxide," Phys. Rev. Res. **1**, 033152 (2019). (Cited on p. 87 and 88.)

[185] A. M. Sayler, T. Rathje, W. Müller, K. Rühle, R. Kienberger, and
G. G. Paulus, "Precise, real-time, every-single-shot, carrier-envelope
phase measurement of ultrashort laser pulses," Opt. Lett. **36**, 1 (2011).
(Cited on p. 89.)

[186] V. Hanus, S. Kangaparambil, S. Larimian, M. Dorner-Kirchner, X. Xie,
A. Baltuška, and M. Kitzler-Zeiler, "Exploring photoelectron angular
distributions emitted from molecular dimers by two delayed intense
laser pulses," Phys. Rev. A **102**, 053115 (2020). (Cited on p. 89.)

[187] A. M. Perelomov, V. S. Popov, and M. V. Terent'ev, "Ionization of

Atoms in an Alternating Electric Field," Sov. Phys. JETP **23**, 924–934 (1966). (Cited on p. 98.)

[188] M. V. Ammosov, N. Delone, and V. P. Krainov, "Tunnel ionization of complex atoms and of atomic ions in an alternating electromagnetic field," Sov. Phys. JETP **64**, 1191 (1986). (Cited on p. 98.)

[189] U. Eichmann, "Strong-Field Induced Atomic Excitation and Kinematics," in "Ultrafast Dyn. Driven by Intense Light Pulses From Atoms to Solids, from Lasers to Intense X-rays," , M. Kitzler and S. Gräfe, eds. (Springer, Cham, 2016), chap. 1, pp. 3–25. (Cited on p. 103.)

[190] X. Xie, K. Doblhoff-Dier, H. Xu, S. Roither, M. S. Schöffler, D. Kartashov, S. Erattupuzha, T. Rathje, G. G. Paulus, K. Yamanouchi, A. Baltuška, S. Gräfe, and M. Kitzler, "Selective Control over Fragmentation Reactions in Polyatomic Molecules Using Impulsive Laser Alignment," Phys. Rev. Lett. **112**, 163003 (2014). (Cited on p. 105.)

[191] X. Xie, S. Roither, M. Schöffler, E. Lötstedt, D. Kartashov, L. Zhang, G. G. Paulus, A. Iwasaki, A. Baltuška, K. Yamanouchi, and M. Kitzler, "Electronic Predetermination of Ethylene Fragmentation Dynamics," Phys. Rev. X **4**, 021005 (2014). (Cited on p. 105.)

[192] S. Erattupuzha, C. L. Covington, A. Russakoff, E. Lötstedt, S. Larimian, V. Hanus, S. Bubin, M. Koch, S. Gräfe, A. Baltuška, X. Xie, K. Yamanouchi, K. Varga, and M. Kitzler, "Enhanced ionisation of polyatomic molecules in intense laser pulses is due to energy upshift and field coupling of multiple orbitals," J. Phys. B At. Mol. Opt. Phys. **50**, 125601 (2017). (Cited on p. 105.)

[193] S. Larimian, S. Erattupuzha, S. Mai, P. Marquetand, L. González, A. Baltuška, M. Kitzler, and X. Xie, "Molecular oxygen observed by direct photoproduction from carbon dioxide," Phys. Rev. A **95**, 011404 (2017). (Cited on p. 105.)

[194] M. Kitzler and M. Lezius, "Spatial Control of Recollision Wave Packets

with Attosecond Precision," Phys. Rev. Lett. **95**, 253001 (2005). (Cited on p. 105 and 109.)

[195] M. Kitzler, X. Xie, A. Scrinzi, and A. Baltuska, "Optical attosecond mapping by polarization selective detection," Phys. Rev. A **76**, 011801 (2007). (Cited on p. 105 and 109.)

[196] M. Kitzler, X. Xie, S. Roither, A. Scrinzi, and A. Baltuska, "Angular encoding in attosecond recollision," New J. Phys. **10**, 025029 (2008). (Cited on p. 105 and 109.)

[197] H. Eichmann, A. Egbert, S. Nolte, C. Momma, B. Wellegehausen, W. Becker, S. Long, and J. K. McIver, "Polarization-dependent high-order two-color mixing," Phys. Rev. A **51**, R3414–R3417 (1995). (Cited on p. 105.)

[198] L. Medišauskas, J. Wragg, H. van der Hart, and M. Y. Ivanov, "Generating Isolated Elliptically Polarized Attosecond Pulses Using Bichromatic Counterrotating Circularly Polarized Laser Fields," Phys. Rev. Lett. **115**, 153001 (2015). (Cited on p. 105.)

[199] X. Ren, J. Li, Y. Yin, K. Zhao, A. Chew, Y. Wang, S. Hu, Y. Cheng, E. Cunningham, Y. Wu, M. Chini, and Z. Chang, "Attosecond light sources in the water window," Journal of Optics **20**, 023001 (2018). (Cited on p. 112 and 118.)

[200] Y. Fu, K. Nishimura, R. Shao, A. Suda, K. Midorikawa, P. Lan, and E. J. Takahashi, "High efficiency ultrafast water-window harmonic generation for single-shot soft x-ray spectroscopy," Communications Physics **3** (2020). (Cited on p. 112 and 118.)

[201] A. Bhattacherjee and S. R. Leone, "Ultrafast x-ray transient absorption spectroscopy of gas-phase photochemical reactions: A new universal probe of photoinduced molecular dynamics," Accounts of Chemical Research **51**, 3203–3211 (2018). (Cited on p. 112 and 118.)

[202] A. D. Smith, T. Balčiūnas, Y.-P. Chang, C. Schmidt, K. Zinchenko, F. B. Nunes, E. Rossi, V. Svoboda, Z. Yin, J.-P. Wolf, and H. J.

Wörner, "Femtosecond soft-x-ray absorption spectroscopy of liquids with a water-window high-harmonic source," The Journal of Physical Chemistry Letters **11**, 1981–1988 (2020). PMID: 32073862. (Cited on p. 112.)

[203] I. Jordan, M. Huppert, M. A. Brown, J. A. van Bokhoven, and H. J. Wörner, "Photoelectron spectrometer for attosecond spectroscopy of liquids and gases," Review of Scientific Instruments **86**, 123905 (2015). (Cited on p. 112.)

[204] Y. Pertot, C. Schmidt, M. Matthews, A. Chauvet, M. Huppert, V. Svoboda, A. von Conta, A. Tehlar, D. Baykusheva, J.-P. Wolf, and H. J. Wörner, "Time-resolved x-ray absorption spectroscopy with a water window high-harmonic source," Science **355**, 264–267 (2017). (Cited on p. 112, 114, and 118.)

[205] L. Barreau, A. D. Ross, S. Garg, P. M. Kraus, D. M. Neumark, and S. R. Leone, "Efficient table-top dual-wavelength beamline for ultrafast transient absorption spectroscopy in the soft x-ray region," Scientific Reports **10**, 5773 (2020). (Cited on p. 112 and 113.)

[206] A. R. Attar, A. Bhattacherjee, C. D. Pemmaraju, K. Schnorr, K. D. Closser, D. Prendergast, and S. R. Leone, "Femtosecond x-ray spectroscopy of an electrocyclic ring-opening reaction," Science **356**, 54–59 (2017). (Cited on p. 112, 113, 114, and 118.)

[207] A. Bhattacherjee, K. Schnorr, S. Oesterling, Z. Yang, T. Xue, R. de Vivie-Riedle, and S. R. Leone, "Photoinduced heterocyclic ring opening of furfural: Distinct open-chain product identification by ultrafast x-ray transient absorption spectroscopy," Journal of the American Chemical Society **140**, 12538–12544 (2018). PMID: 30204442. (Cited on p. 112.)

[208] A. Bhattacherjee, C. D. Pemmaraju, K. Schnorr, A. R. Attar, and S. R. Leone, "Ultrafast intersystem crossing in acetylacetone via femtosecond x-ray transient absorption at the carbon k-edge," Journal

of the American Chemical Society **139**, 16576–16583 (2017). PMID: 29083165. (Cited on p. 112.)

[209] Z. Yang, K. Schnorr, A. Bhattacherjee, P.-L. Lefebvre, M. Epshtein, T. Xue, J. F. Stanton, and S. R. Leone, "Electron-withdrawing effects in the photodissociation of ch2icl to form ch2cl radical, simultaneously viewed through the carbon k and chlorine l2,3 x-ray edges," Journal of the American Chemical Society **140**, 13360–13366 (2018). (Cited on p. 112.)

[210] K. Schnorr, A. Bhattacherjee, K. J. Oosterbaan, M. G. Delcey, Z. Yang, T. Xue, A. R. Attar, A. S. Chatterley, M. Head-Gordon, S. R. Leone, and O. Gessner, "Tracing the 267 nm-induced radical formation in dimethyl disulfide using time-resolved x-ray absorption spectroscopy," The Journal of Physical Chemistry Letters **10**, 1382–1387 (2019). (Cited on p. 112.)

[211] G. Fan, V. Cardin, K. Legare, E. Kaksis, G. Andriukaitis, A. Pugzlys, T. Kanai, B. Schmidt, P. Vladimir, F. Légaré, A. Baltuska, and T. Balčiūnas, "High flux soft x-ray source driven on yb laser amplifier for resonant magnetic diffraction application," in "High-Brightness Sources and Light-driven Interactions," (OSA, 2018). (Cited on p. 113, 117, and 123.)

[212] T. Popmintchev, M.-C. Chen, A. Bahabad, M. Gerrity, P. Sidorenko, O. Cohen, I. P. Christov, M. M. Murnane, and H. C. Kapteyn, "Phase matching of high harmonic generation in the soft and hard x-ray regions of the spectrum," Proceedings of the National Academy of Sciences **106**, 10516–10521 (2009). (Cited on p. 113, 114, and 118.)

[213] H. Xiong, H. Xu, Y. Fu, J. Yao, B. Zeng, W. Chu, Y. Cheng, Z. Xu, E. J. Takahashi, K. Midorikawa, X. Liu, and J. Chen, "Generation of a coherent x ray in the water window region at 1 khz repetition rate using a mid-infrared pump source," Opt. Lett. **34**, 1747–1749 (2009). (Cited on p. 114 and 118.)

[214] Y. Fu, K. Nishimura, R. Shao, A. Suda, K. Midorikawa, P. Lan, and E. J. Takahashi, "High efficiency ultrafast water-window harmonic generation for single-shot soft x-ray spectroscopy," Communications Physics **3**, 92 (2020). (Cited on p. 114 and 118.)

[215] N. Ishii, K. Kaneshima, K. Kitano, T. Kanai, S. Watanabe, and J. Itatani, "Carrier-envelope phase-dependent high harmonic generation in the water window using few-cycle infrared pulses," Nature Communications **5**, 3331 (2014). (Cited on p. 114 and 118.)

[216] E. J. Takahashi, T. Kanai, K. L. Ishikawa, Y. Nabekawa, and K. Midorikawa, "Coherent water window x ray by phase-matched high-order harmonic generation in neutral media," Phys. Rev. Lett. **101**, 253901 (2008). (Cited on p. 114 and 118.)

[217] A. S. Johnson, L. Miseikis, D. A. Wood, D. R. Austin, C. Brahms, S. Jarosch, C. S. Strüber, P. Ye, and J. P. Marangos, "Measurement of sulfur l2,3 and carbon k edge xanes in a polythiophene film using a high harmonic supercontinuum," Structural Dynamics **3**, 062603 (2016). (Cited on p. 114 and 118.)

[218] S. L. Cousin, N. D. Palo, B. Buades, S. M. Teichmann, M. Reduzzi, M. Devetta, A. Kheifets, G. Sansone, and J. Biegert, "Attosecond streaking in the water window: A new regime of attosecond pulse characterization," Physical Review X **7** (2017). (Cited on p. 114 and 118.)

[219] S. M. Teichmann, F. Silva, S. L. Cousin, M. Hemmer, and J. Biegert, "0.5-kev soft x-ray attosecond continua," Nature Communications **7**, 11493 (2016). (Cited on p. 114 and 118.)

[220] M.-C. Chen, P. Arpin, T. Popmintchev, M. Gerrity, B. Zhang, M. Seaberg, D. Popmintchev, M. M. Murnane, and H. C. Kapteyn, "Bright, coherent, ultrafast soft x-ray harmonics spanning the water window from a tabletop light source," Phys. Rev. Lett. **105**, 173901 (2010). (Cited on p. 114 and 118.)

[221] G. J. Stein, P. D. Keathley, P. Krogen, H. Liang, J. P. Siqueira, C.-

L. Chang, C.-J. Lai, K.-H. Hong, G. M. Laurent, and F. X. Kärtner, "Water-window soft x-ray high-harmonic generation up to the nitrogen k-edge driven by a khz, 2.1um opcpa source," Journal of Physics B: Atomic, Molecular and Optical Physics **49**, 155601 (2016). (Cited on p. 114 and 118.)

[222] T. Popmintchev, M.-C. Chen, D. Popmintchev, P. Arpin, S. Brown, S. Ališauskas, G. Andriukaitis, T. Balčiūnas, O. D. Mücke, A. Pugzlys, A. Baltuška, B. Shim, S. E. Schrauth, A. Gaeta, C. Hernández-García, L. Plaja, A. Becker, A. Jaron-Becker, M. M. Murnane, and H. C. Kapteyn, "Bright coherent ultrahigh harmonics in the kev x-ray regime from mid-infrared femtosecond lasers," Science **336**, 1287–1291 (2012). (Cited on p. 114 and 118.)

[223] J. E. Beetar, M. Nrisimhamurty, T.-C. Truong, G. C. Nagar, Y. Liu, J. Nesper, O. Suarez, F. Rivas, Y. Wu, B. Shim, and M. Chini, "Multi-octave supercontinuum generation and frequency conversion based on rotational nonlinearity," Science Advances **6**, eabb5375 (2020). (Cited on p. 114, 115, 118, and 120.)

[224] R. Safaei, G. Fan, O. Kwon, K. Légaré, P. Lassonde, B. E. Schmidt, H. Ibrahim, and F. Légaré, "High-energy multidimensional solitary states in hollow-core fibres," Nature Photonics **14**, 733–739 (2020). (Cited on p. 114, 115, 118, and 120.)

[225] G. Cerullo and S. De Silvestri, "Ultrafast optical parametric amplifiers," Rev. Sci. Instrum. **74**, 1 (2003). (Cited on p. 115.)

[226] C. Manzoni and G. Cerullo, "Design criteria for ultrafast optical parametric amplifiers," Journal of Optics **18**, 103501 (2016). (Cited on p. 115.)

[227] A. M. Siddiqui, K.-H. Hong, J. Moses, and F. X. Kärtner, "Bandwidth extension and conversion efficiency improvements beyond phase matching limitations using cavity-enhanced opcpa," Opt. Express **29**, 9907–9926 (2021). (Cited on p. 115.)

[228] A. Y. Naumov, D. M. Villeneuve, and H. Niikura, "High conversion efficiency of an optical parametric amplifier pumped by 1 khz ti:sapphire laser pulses for tunable high-harmonic generation," Opt. Express **28**, 4088–4098 (2020). (Cited on p. 115.)

[229] A. Owens, A. Yachmenev, and J. Küpper, "Coherent control of the rotation axis of molecular superrotors," The Journal of Physical Chemistry Letters **9**, 4206–4209 (2018). PMID: 29991265. (Cited on p. 115.)

[230] G. Andriukaitis, T. Balčiūnas, S. Ališauskas, A. Pugžlys, A. Baltuška, T. Popmintchev, M.-C. Chen, M. M. Murnane, and H. C. Kapteyn, "90 GW peak power few-cycle mid-infrared pulses from an optical parametric amplifier," Opt. Lett. **36**, 2755 (2011). (Cited on p. 115.)

[231] G. Fan, K. Légaré, V. Cardin, X. Xie, R. Safaei, E. Kaksis, G. Andriukaitis, A. Pugžlys, B. E. Schmidt, J. P. Wolf, M. Hehn, G. Malinowski, B. Vodungbo, E. Jal, J. Lüning, N. Jaouen, G. Giovannetti, F. Calegari, Z. Tao, A. Baltuška, F. Légaré, and T. Balčiūnas, "Ultrafast magnetic scattering on ferrimagnets enabled by a bright yb-based soft x-ray source," Optica **9**, 399–407 (2022). (Cited on p. 117.)

[232] B. Henke, E. Gullikson, and J. Davis, "X-ray interactions: Photoabsorption, scattering, transmission, and reflection at e = 50-30,000 ev, z = 1-92," Atomic Data and Nuclear Data Tables **54**, 181–342 (1993). (Cited on p. 122 and 123.)

[233] G. Fan, P. A. Carpeggiani, Z. Tao, G. Coccia, R. Safaei, E. Kaksis, A. Pugzlys, F. Légaré, B. E. Schmidt, and A. Baltuška, "70 mj nonlinear compression and scaling route for an yb amplifier using large-core hollow fibers," Opt. Lett. **46**, 896–899 (2021). (Cited on p. 125.)

A song comes to an end ...

...

... and a new one starts.

Martin Dorner-Kirchner

Personal Data

Name:	Martin Dorner-Kirchner
Gender:	male
Place and Date of Birth:	Vienna, Austria | ████
Address:	████████████
Phone:	████████
email:	martin.kirchner@tuwien.ac.at
Family status:	████████

Education

07/2017 present	PhD studies at Photonics Institute, Technische Universität Wien
05/2017	Master of Science degree, MSc. Technische Universität Wien
04/2013–05/2017	Studies of Technical Physics at TU Wien
04/2013	Bachelor of Science degree, BSc. Technische Universität Wien
10/2009–04/2013	Studies of Technical Physics at TU Wien
05/2009	Matura Höhere technische Lehranstalt Hollabrunn
09/2004–05/2009	Studies of electronics and computer technology at HTL Hollabrunn

Journal Articles

M. Dorner-Kirchner, V. Shumakova, G. Coccia, E. Kaksis, B. Schmidt, V. Pervak, A. Pugzlys, A. Baltuška, M. Kitzler-Zeiler, and P.-A. Carpeggiani, "HHG at the carbon K-edge directly driven by SRS red-shifted pulses from an ytterbium amplifier," **In Preparation** (2022).

M. Dorner-Kirchner, S. Erattupuzha, S. Larimian, M. Koch, V. Hanus, S. Kangaparambil, G. Paulus, A. Baltuška, X. Xie, M. Kitzler-Zeiler, Y. Wang, X. Lai, S. Yu, R. Sun, and X. Liu, "Laser-subcycle control of electronic excitation across system boundaries," *Journal of Physics B: Atomic, Molecular and Optical Physics* **54**, 164004 (2021).

H. Hu, S. Kangaparambi, **M. Dorner-Kirchner**, V. Hanus, A. Baltuška, M. Kitzler-Zeiler, and X. Xie, Quantitative retrieval of the angular dependence of laser-induced electron rescattering in molecules, *Phys. Rev. A* **103**, 013114 (2021).

V. Hanus, S. Kangaparambil, S. Larimian, **M. Dorner-Kirchner**, X. Xie, A. Baltuška, and M. Kitzler-Zeiler, "Exploring photoelectron angular distributions emitted from molecular dimers by two delayed intense laser pulses," *Phys. Rev. A* **102**, 053115 (2020).

Y. Wang, X. Lai, S. Yu, R. Sun, X. Liu, **M. Dorner-Kirchner**, S. Erattupuzha, S. Larimian, M. Koch, V. Hanus, S. Kangaparambil, G. Paulus, A. Baltuška, X. Xie, and M. Kitzler-Zeiler,

"Laser-induced electron transfer in the dissociative multiple ionization of argon dimers," *Phys. Rev. Lett.* **125**, 063202 (2020).

S. Kangaparambil, V. Hanus, **M. Dorner-Kirchner**, P. He, S. Larimian, G. Paulus, A. Baltuška, X. Xie, K. Yamanouchi, F. He, E. Lötstedt, and M. Kitzler-Zeiler, "Generalized phase sensitivity of directional bond breaking in the laser-molecule interaction," Phys. Rev. Lett. **125**, 023202 (2020).

V. Hanus, S. Kangaparambil, S. Larimian, **M. Dorner-Kirchner**, X. Xie, M. S. Schöffler, G. G. Paulus, A. Baltuška, A. Staudte, and M. Kitzler-Zeiler, "Experimental separation of subcycle ionization bursts in strong-field double ionization of H₂," *Phys. Rev. Lett.* **124**, 103201 (2020).

V. Hanus, S. Kangaparambil, S. Larimian, **M. Dorner-Kirchner**, X. Xie, M. S. Schöffler, G. G. Paulus, A. Baltuška, A. Staudte, and M. Kitzler-Zeiler, "Subfemtosecond tracing of molecular dynamics during strong-field interaction," *Phys. Rev. Lett.* **123**, 263201 (2019).

Conference Contributions

V. Hanus, S. Kangaparambil, **M. Dorner-Kirchner**, S. Larimian, X. Xie, A. Baltuška, and M. Kitzler-Zeiler, "Photoelectron Circular Dichroism at the Few-Cycle Limit in the Tunnel Ionization Regime," *2019 CLEO/Europe-EQEC*, **Poster**, 19148223 (2019).

V. Hanus, S. Kangaparambil, **M. Dorner-Kirchner**, S. Larimian, X. Xie, M. S. Schöffler, A. Staudte, G. G. Paulus, A. Baltuška, and M. Kitzler-Zeiler, "Sub-Cycle Separation of Ionization Bursts in the Double Ionization of H2," *2019 CLEO/Europe-EQEC*, **Talk**, 19148736 (2019).

M. Dorner-Kirchner, P.A. Carpeggiani, and M. Kitzler-Zeiler, "Versatile apparatus for ultrafast XUV-spectroscopy," *2018 ICTP Winter College on Extreme Non-linear Optics, Attosecond Science and High-field Physics*, **Poster**, (2018)